

**USE OF SURFACE SPECIFIC FLOW FACTORS IN A MULTI-  
PHYSICAL MODEL OF POWER CYLINDER COMPONENTS**

by

Alexander Joseph Locker IV

A thesis submitted to the Graduate Faculty of  
Auburn University  
in partial fulfillment of the  
requirements for the Degree of  
Master of Science in Mechanical Engineering

Auburn, Alabama  
May 5, 2018

Keywords: Flow Factors, Hydrodynamic Lubrication,  
Predictive Modeling, Engine Components

Copyright 2018 by Alexander Joseph Locker IV

Approved by

Robert L. Jackson, Chair, Professor of Mechanical Engineering  
Jay Khodadadi, Professor of Mechanical Engineering  
David Beale, Professor of Mechanical Engineering

## ABSTRACT

New technologies are being introduced for power cylinder components at a faster rate due to the drive for better fuel economy and CO<sub>2</sub> foot print reduction. This includes new and advanced coatings, materials, and surface textures. In turn, robust methods are needed to evaluate and optimize technologies to ensure optimal performance. Therefore, the study of tribological lubrication flow has become more pressing among power cylinder components. This thesis analyzes the modification of the Reynolds equation for computational efficiency by analyzing rough surfaces in the hydrodynamic flow regime through the use of flow factors. This analysis is aimed towards modeling the surface interactions and pressure variations across power cylinder components of an internal combustion engine, namely the piston ring and cylinder wall. These interacting surfaces were measured directly through the use of a profilometer. Through the use of these measured surface properties, surface specific flow factors are derived by numerical flow simulation. The statistical flow factors are obtained and implemented in the Reynolds equation to model the pressure and shear variations across the asperities of interacting surfaces. These flow factors can then be used to consider the effect of roughness in lubrication problems without deterministically modeling roughness. The derived flow factors make predictions that are significantly different than those in existing literature. This derivation methodology can be used in the determination of flow factors for any pair of interacting surfaces. The governing flow factors for a pair of surfaces are expressed as empirical relations in terms of the film ratio ( $h/\sigma$ ). The flow

factors are then applied to an initial analysis of a multi-physical model of power cylinder components in a two-dimensional axisymmetric case to consider roughness throughout the combustion cycle in order to evaluate tribological interactions.

## ACKNOWLEDGMENTS

I would like to thank my advisor, Professor Robert L. Jackson for helping me and believing in me through my research. This opportunity is once in a lifetime and he supplied me with that. Thanks to my committee members Professor Jay Khodadadi and Professor David Beale for agreeing to help me in earning my Master's Degree.

A special thanks to Ford Motor Company for funding the research as a part of Ford University Research Program (URP) and allowing us to work closely with them.

I would also love to thank my family for their continued support in all the good times and in all the bad, and for all their insight that life has to offer. Thanks to my Dad, Al J. Locker, III "Pops", for his insight and continued motivation throughout my time as an Auburn Tiger. Your motivational pep talks touched me while on the soccer field as a 5 year old, just as they did while playing football for Auburn, and continued throughout my Bachelor's and Master's degrees at Auburn. Thanks also to my Mother, Elise A. Locker "Momma", for her unwavering support through my degrees. Your ability to always find a silver lining has and always will put a smile on my face no matter how easy or hard the day was. Thanks also to my sister, Kirsten A. Locker "Hen Hen", for her uncanny ability to lighten a situation and as a sister I can always talk to. I love you and our playful banter will never get old.

Last but certainly not least, I would love to thank my incredible fiancé, Danielle, for supporting me through a tough graduate program. I cherish every moment we have together and

will certainly always cherish the memories of our long nights in the library working together. This marks a new chapter in our lives and I'm excited for what the Lord has in store for us.

## TABLE OF CONTENTS

Abstract .....	ii
Acknowledgments.....	iv
List of Tables .....	xi
List of Figures .....	xii
Nomenclature .....	xvii
Chapter 1: Introduction.....	1
1.1 Problem Statement.....	1
1.2 Objective .....	2
1.3 Current Approach and Contributions.....	4
Chapter 2 Background and Literature Review.....	6
2.1 Power – Cylinder Components .....	6
2.1.1 Piston and Crank Mechanisms.....	6
2.1.2 Block, Head, and Pan Construction .....	8
2.1.3 Cylinder Geometry.....	9
2.1.3.1 Squish and Swirl .....	10
2.1.4 Ignition.....	12

2.1.5	Balancing .....	13
2.1.6	The Flame Front.....	14
2.1.7	Gas Dynamics .....	15
2.1.7.1	Air and Fuel Flow .....	15
2.1.7.2	Exhaust Flow .....	16
2.1.8	Piston Ring – Pack .....	17
2.2	The Reynolds Equation.....	18
2.2.1	Applications to Power – Cylinder Components.....	19
2.2.2	Alternate Applications .....	19
2.3	Flow Factors.....	20
2.4	Cavitation.....	24
2.4.1	Cavitation Models.....	24
2.4.2	Cavitated Region Boundary Conditions .....	26
Chapter 3	Methodology .....	29
3.1	Measurement of Interacting Surfaces .....	29
3.1.1	Profilometer .....	29
3.1.2	Cylinder Wall – Level Data .....	32
3.1.3	Piston Ring – Curvature.....	33
3.1.4	Surface Topography.....	36

3.1.4.1	Cylinder Wall Features .....	37
3.1.4.2	Piston Ring Features .....	40
3.2	Surface Roughness Directionality Characterization .....	41
3.2.1	Auto-Correlation Function.....	41
3.2.2	Cross-Correlation Function.....	46
3.2.3	Surface Anisotropy Index .....	49
3.3	The Reynolds Equation.....	52
3.3.1	Derivation from Navier-Stokes.....	53
3.3.2	Discretization .....	58
3.3.2.1	Coefficients for Reynolds Equation Discretization .....	58
3.3.2.2	Complete Discretized Equation .....	60
3.3.3	Verification .....	61
3.3.4	Convergence and Relaxation .....	70
3.3.5	Alternate Numerical Schemes.....	74
Chapter 4	Flow Factor Derivation .....	76
4.1	Flow Rate Ratios.....	77
4.2	Boundary Conditions .....	81
4.2.1	Pressure Flow Factors Boundary Conditions.....	82
4.2.2	Shear Flow Factor Boundary Conditions.....	82

4.3	Pressure Flow Factors .....	83
4.4	Shear Flow Factor .....	85
4.4.1	Ambient Pressure of 0 kPa.....	86
4.4.2	Reference Pressure of 101 kPa .....	92
4.5	Numerical Results .....	96
4.5.1	X-Direction Pressure Flow Factor.....	99
4.5.2	Z-Direction Pressure Flow Factor .....	102
4.5.3	Shear Flow Factor .....	105
Chapter 5 Piston Ring Model.....		108
5.1	Lubrication Model .....	108
5.2	Solid Contact Model .....	111
5.3	Coupled Lubrication and Solid Contact Models.....	113
5.3.1	Coupled Model Test Cases .....	114
5.4	Finite Element Ring Model.....	118
5.5	Boundary Conditions .....	119
5.6	Force and Moment Balance .....	120
5.7	Convergence .....	122
5.8	Piston Ring Model Results.....	125
5.9	Future Model Implementations.....	133

5.9.1 Dynamic Model .....	134
Chapter 6 Closure .....	136
6.1 Conclusions.....	136
6.2 Future Work.....	137
Appendix A Program Code.....	139
Appendix B Future Models.....	208
References.....	216

## LIST OF TABLES

Table 3.1 Surface data parameters .....	51
Table 3.2 Surface anisotropy index values .....	51
Table 3.3 System parameters .....	64
Table 3.4 Relaxation factors for slider bearing models .....	74
Table 4.1 System parameters .....	86
Table 4.2 Load carrying capacity results .....	96
Table 4.3 Coefficients for $x$ and $z$ pressure flow factors.....	97
Table 4.4 Coefficients for shear flow factor .....	98
Table 4.5 Relaxation factors for simulation cases .....	99
Table 5.1 Coupled model test case parameters .....	115

## LIST OF FIGURES

Figure 2.1 Piston components.....	7
Figure 2.2 Cylinder geometry to induce angular velocity .....	10
Figure 2.3 Hemi-spherical nature of combustion chamber to induce swirl.....	11
Figure 2.4 Spark plug electrode bridge.....	12
Figure 2.5 Piston ring and cylinder wall tribological interaction .....	18
Figure 2.6 Stribeck curve with marked lubrication regimes.....	21
Figure 2.7 Depiction of various lubrication regimes .....	22
Figure 2.8 (a) The full-Sommerfeld boundary conditions and (b) Half-Sommerfeld boundary condition .....	27
Figure 3.1 Influence of stylus tip on surface measurement .....	30
Figure 3.2 Current Production Engine Cylinder Wall (Isometric View).....	31
Figure 3.3 Current Production Engine Cylinder Wall (Top View) .....	31
Figure 3.4 Piston ring with curvature (Isometric View).....	33
Figure 3.5 One row of measured data points on the curved piston ring .....	34
Figure 3.6 Side view of piston ring structure.....	35
Figure 3.7 Piston ring without curvature (Isometric View).....	35
Figure 3.8 Piston ring without curvature (Top View).....	36
Figure 3.9 Chemical make-up of cylinder wall to improve lubrication and hardness effects. In (a) is Carbon, (b) is Chromium, (c) is Copper, (d) is Iron, (e) is Manganese, (f) is	

Oxygen, (g) is Phosphorus, (h) is Silicon, (i) is SEM of cylinder wall, and (j) is the Zinc map .....	39
Figure 3.10 Surface profile of auto-correlation parameters.....	42
Figure 3.11 Auto-Correlation Function for the cylinder wall.....	43
Figure 3.12 Auto-Correlation Function for the piston ring.....	45
Figure 3.13 Auto-Correlation Function for convoluted surfaces.....	45
Figure 3.14 Cross-Correlation Function direction.....	47
Figure 3.15 Cross-Correlation Function for convoluted surfaces.....	48
Figure 3.16 Typical surface characterization for transversely ( $\gamma < 1$ ) oriented, isotropic ( $\gamma = 1$ ), and longitudinally oriented ( $\gamma > 1$ ) surfaces.....	50
Figure 3.17 Control volume.....	55
Figure 3.18 Poiseuille flow .....	57
Figure 3.19 Couette flow .....	57
Figure 3.20 Discretization of Pressure ( $p$ ) and Film Thickness ( $h$ ).....	58
Figure 3.21 Fixed incline slider bearing geometry.....	62
Figure 3.22 Nodal discretization for slider bearing .....	63
Figure 3.23 Film thickness of 1-D slider bearing .....	65
Figure 3.24 Pressure distribution along 1-D slider bearing .....	66
Figure 3.25 Force per unit width of the slider bearing .....	67
Figure 3.26 Film thickness of 2-D slider bearing.....	69
Figure 3.27 Pressure distribution along 2-D slider bearing.....	69

Figure 3.28 Pressure convergence of modeled slider bearing .....	71
Figure 3.29 Convergence error of modeled slider bearing .....	73
Figure 3.30 Typical progression of numerical nodal scheme calculations .....	74
Figure 3.31 Alternate progression of numerical nodal scheme calculations .....	75
Figure 4.1 Film thickness function .....	77
Figure 4.2 Pressure flow region for model .....	79
Figure 4.3 Interacting power cylinder components (Isometric View).....	83
Figure 4.4 Interacting power cylinder components (Y-Z View).....	84
Figure 4.5 Cylinder wall pressure distribution due to shearing (Top View) .....	87
Figure 4.6 Cylinder wall pressure distribution due to shearing (Isometric View).....	88
Figure 4.7 Cylinder wall pressure distribution due to shearing (Isometric View).....	88
Figure 4.8 Cylinder wall pressure distribution due to shearing (X-Y View).....	89
Figure 4.9 Piston ring pressure distribution due to shearing (Top View).....	91
Figure 4.10 Piston ring pressure distribution due to shearing (Isometric View).....	91
Figure 4.11 Piston ring pressure distribution due to shearing (X-Y View).....	92
Figure 4.12 Cylinder wall pressure distribution due to shearing without cavitation (Top View) .....	93
Figure 4.13 Cylinder wall pressure distribution due to shearing without cavitation (Isometric View).....	93
Figure 4.14 Piston ring pressure distribution due to shearing (Top View).....	94
Figure 4.15 Piston ring pressure distribution due to shearing (Isometric View).....	95

Figure 4.16 Poiseuille flow in the $x$ direction for smooth surfaces .....	100
Figure 4.17 Poiseuille flow in the $x$ direction for rough surfaces .....	100
Figure 4.18 $X$ direction pressure flow factor .....	101
Figure 4.19 Poiseuille flow in the $z$ direction for smooth surfaces.....	103
Figure 4.20 Poiseuille flow in the $z$ direction for rough surfaces .....	103
Figure 4.21 $Z$ direction pressure flow factor.....	104
Figure 4.22 Shear flow factors.....	105
Figure 4.23 Shear flow factor comparison.....	106
Figure 5.1 Elastic-Plastic contact pressure for the combined surfaces.....	112
Figure 5.2 Total pressure acting on outer piston ring surface.....	116
Figure 5.3 Pressure acting on outer piston ring surface.....	117
Figure 5.4 Sample Abaqus mesh .....	118
Figure 5.5 Free body diagram of piston ring and cylinder interface with sample pressures applied on the ring surfaces.....	120
Figure 5.6 Flowchart of the iterative scheme used to solve the coupled contact and lubrication problem.....	124
Figure 5.7 Piston ring rotation about the Center of Mass .....	126
Figure 5.8 Pressure on outer ring surface .....	126
Figure 5.9 Pressure on upper ring surface .....	128
Figure 5.10 Pressure on inner ring surface .....	129
Figure 5.11 Pressure on lower ring surface .....	129

Figure 5.12 Total pressure on piston ring surfaces (smaller film thickness) .....	130
Figure 5.13 Total pressure on piston ring surfaces (larger film thickness) .....	131
Figure 5.14 Output deformation results in MATLAB .....	132
Figure 5.15 Ford piston ring with rounded edges .....	133
Figure 5.16 Modeled piston speed for slider bearing .....	134
Figure B.1 Discretization of Temperature ( $T$ ) .....	211
Figure B.2 Converged temperatures across four surfaces .....	213
Figure B.3 Temperatures at each point converging .....	214
Figure B.4 Converged temperature value and time .....	214

## NOMENCLATURE

$A$	=	Area
$A_r$	=	Real contact area
$A_n$	=	Nominal contact area
$ACF$	=	Auto-Correlation Function
$a_0 - a_5$	=	Reynolds coefficients
$a$	=	Axial width of piston ring
$BDC$	=	Bottom Dead Center
$C_d$	=	Discharge coefficient
$CM$	=	Center of Mass
$CCF$	=	Cross-Correlation Function
$E$	=	Elastic modulus
$e$	=	Internal energy per unit mass
$F$	=	Force
$f_j$	=	Body forces experienced
$G_0$	=	Roeland's equation constant
$H$	=	Film ratio ( $h/\sigma$ )
$h$	=	Nominal film thickness

$h_1$	=	Slider bearing inlet
$h_2$	=	Slider bearing outlet
$h_T$	=	Local film thickness
$K$	=	Iteration number
$L$	=	Length of bearing
$M$	=	Moment
$m$	=	Mass
$\dot{m}$	=	Mass flow rate
$mg$	=	Milligrams
$N$	=	Length of sample data
$P$	=	Linear momentum
$p$	=	Pressure
$p_0$	=	Stagnation pressure
$q$	=	Flow rate
$R$	=	Bubble radius
$R_{ah}$	=	Asperity height
$RMS$	=	Root Mean Square surface roughness
$r$	=	Radial width of piston ring
$S$	=	Surface tension between boundary of the cavity and the fluid

$S_0$	=	Roeland's equation constant
$S_y$	=	Yield strength
$SOR$	=	Successive Over Relaxation
$SUR$	=	Successive Under Relaxation
$T$	=	Temperature
$T_0$	=	Stagnation temperature
$TDC$	=	Top Dead Center
$t$	=	Time
$\bar{U}$	=	Relative sliding velocity
$u, v, w$	=	Velocities in Cartesian coordinates
$\mathbf{V}$	=	Velocity
$V_{r1}$	=	Variance ratio of surface 1 (Cylinder wall)
$V_{r2}$	=	Variance ratio of surface 2 (Piston ring)
$W$	=	Relaxation factor
$w$	=	Load-carrying capacity
$x, y, z$	=	Cartesian coordinate system
$X_{ii}$	=	2-D measured surface profile
$X_{ij}$	=	3-D measured surface profile
$x_b$	=	Burned gas fraction

$x_r$	=	Unburnt residuals
$\gamma$	=	Surface anisotropy index (Peklenik number)
$\delta_1, \delta_2$	=	Roughness amplitude of surfaces from mean height
$\eta$	=	Asperity density
$\theta$	=	Angle of crankshaft
$\theta_d$	=	Crankshaft angle duration
$\theta_s$	=	Crankshaft angle at start of combustion
$\lambda$	=	Horizontal distance between asperities
$\lambda_{0.5}$	=	Half the correlation length
$\lambda_{0.5x}$	=	Half the correlation length in the $x$ direction
$\lambda_{0.5z}$	=	Half the correlation length in the $z$ direction
$\mu$	=	Dynamic viscosity
$\mu m$	=	Micrometers
$\nu$	=	Kinematic viscosity
$\nu_p$	=	Poisson's ratio
$\rho$	=	Density
$\rho_{ii}$	=	Auto-Correlation Function
$\rho_{ij}$	=	Cross-Correlation Function
$\sigma$	=	Composite RMS value

$\sigma_1, \sigma_2$	=	RMS value of Cylinder wall and Piston ring
$\sigma_s$	=	Asperity peaks RMS value
$\Phi$	=	Dissipation function
$\Phi_{s1}, \Phi_{s2}$	=	Shear flow factor for rough surface against smooth surface
$\varphi_x$	=	Pressure flow factor in the $x$ direction
$\varphi_z$	=	Pressure flow factor in the $z$ direction
$\varphi_s$	=	Composite shear flow factor

## CHAPTER 1

### INTRODUCTION

#### *1.1 Problem Statement*

While a macroscopic study of the engine dynamics is necessary for the success of any fluid bearing component, so are the microscopic interactions. Surface topography plays a large role in not only component longevity, but also more importantly in efficiency and performance. It is therefore useful to study these surface interactions, namely when a lubricant is involved. It is computationally and numerically difficult to model the flow past individual asperities along all components. For this very reason the governing lubricant flow equation, the Reynolds equation, is modified by the use of pressure and shear flow factors.

Flow factors are a method used to statistically model a rough surface as a smooth surface, previously introduced by Patir and Cheng [1] in their “Average Flow Model”, by deriving properties from the rough surfaces. The layout of asperities in Patir and Cheng’s [1] model was numerically generated, and these asperity layouts were assumed to be either purely transverse, isotropic, or purely longitudinal. The flow past and around these points could then be statistically modeled. These models are then able to be used in conjunction with the Reynolds equation for a more accurate solution which takes into account surface features.

While far more accurate than modeling the hydrodynamic properties of flow across smooth surfaces, these generic flow model equations are less accurate than deriving surface specific flow factor models for predicting the fluid interactions in the hydrodynamic regime. Thus more precise flow modeling equations are necessary for more accurate flow predictions and computational efficiency. One specific case of great interest that has not received much attention is power cylinder components.

Three primary flow factors are paired with the Reynolds equation, namely to account for surface impedance on the flow of a lubricant. The first of which,  $\varphi_x$  measures the flow resistance across asperities due to a pressure induced gradient along the flow direction. Similarly,  $\varphi_z$  measures the flow resistance along the transverse direction. And lastly,  $\varphi_s$  measures the lubricant transport due to shearing effects. These flow parameters are a function of the film thickness, standard deviation of the surfaces, and the Peklenik number ( $\gamma$ ) as defined by the auto-correlation function derived from the specific surface topography [2]. The Peklenik number relates the various directions of flow together through functional form.

## *1.2 Objective*

The goal of this work is to develop and create a numerical methodology and toolkit that models the cylinder wall, piston, and piston ring interface by considering lubrication and contact mechanics. This model could be used to make parametric predictions of the interfaces performance (e.g. friction) and also possible failure. The coated rough surface contact mechanics and lubrication occurs on a scale much smaller than the size of the piston ring and therefore the key aspect of the

model is an algorithm that solves simultaneously the multiple mechanisms at different scales. This will be accomplished using a modular numerical model with interchangeable components that represent different accepted methodologies.

The Reynolds equation will be solved to consider the effects of hydrodynamic lubrication on the problem. In regions in or near contact where asperities between surfaces come in close proximity, the asperities can influence the lubrication flow. Surface specific flow factors will be derived to include the effect of roughness on lubricant flow in the Reynolds equation.

The elastic superposition and/or the finite element method will be used to model the mechanical deformations of the piston ring surfaces. Other numerical schemes will also be incorporated to model solid sliding friction, boundary lubrication, asperity contact, and full film lubrication. The model will initially be constructed as a quasi-steady state model, and will not consider transient and time dependent effects, but could be added later. The lubrication model considers the pressures and tractions generated by the oil lubricant separating the surfaces. The solid contact model must consider the solid contact and friction between the components, which are defined by the roughness of the surface specific topography. Both of these models make use of the measured geometry of a cylinder surface, piston ring, and their interactions.

The contact mechanics, lubrication, and thermo-mechanical models are coupled through their boundary conditions and material properties which must be solved and satisfied simultaneously. This will be done by use of an iterative process. The coupled problem is non-linear and therefore relaxation techniques will be used to enhance convergence. Once the governing program is operating, it will make many predictions that will be useful for the optimization and

design of the components. For instance, it will predict the portion of the load carried by the lubricant pressure and by the solid contact between the surfaces.

### *1.3 Current Approach and Contributions*

Previously the study of surface roughness effects on lubrication flow has been limited to stochastic concepts as first introduced by Tzeng and Saibel [3]. A new method of flow simulation was derived by Patir and Cheng [1] which was based on numerically solving the Reynolds equation over a modeled bearing with randomly generated surface roughness characteristics, then deriving an average Reynolds equation from several flow quantities. This method is restricted to the assumption that the rough surface heights are a perfect Gaussian distribution [4]. Peklenik [2] sought to introduce random process analysis and signal processing theory in order to characterize rough surfaces. A more accurate flow model comes from combining these two methods such that signal processing theory is used in conjunction with existing flow models which lead to new surface-specific flow model techniques, derived in terms of real measured surfaces.

It is well known that surfaces possess some roughness consisting of deviations from their nominal flatness, especially among power cylinder components [5]. Many researchers have taken a wide array of approaches to solve the problem of lubrication and contact between rough surfaces. It can be difficult and unreasonable to solve the rough surface contact problem from the actual geometry (often referred to as a deterministic methodology) because the profiles of surfaces are very detailed [6]. Therefore, simple closed-form methods accessible to researchers and the practicing engineers are often employed. The current work will provide several different options

to consider elastic-plastic rough surface contact: multiscale methods developed at Auburn [7], statistical methods [8-10], and a deterministic model [11]. This is similar to prior work by Jackson on modeling thrust washer bearings for automotive planetary sets [12, 13] and other tribological interfaces [14, 15]. The previous works are some of the first numerical models to generate the Stribeck curve (i.e. predict friction when either the surfaces are separated by a full film of lubrication in contact).

Surface roughness also plays a large role in thermo-elastohydrodynamic stability. Jang and Khonsari [16-19] found that surface roughness and lubricant film thickness effect the thermal surface deformations and can lead to hot pots. This thermoelastic instability can be improved by reducing sliding speed, decreasing modulus of elasticity of the surfaces, increasing the thermal conductivity, or increasing the film thickness [20]. Surface roughness is seen to have a large effect on the stability of surface interactions through a multitude of cases. It is therefore desired to study the nature of fluid behavior effected by surface roughness, which can lead to predictive flow models.

The following thesis seeks to analyze the derivation of surface specific flow factors for an accurate hydrodynamic lubrication model, specifically for the case of automotive power cylinder components.

## **CHAPTER 2**

### **BACKGROUND AND LITERATURE REVIEW**

#### *2.1 Power – Cylinder Components*

An internal combustion engine is a machine designed to extract work from the combustion of air and fuel inside a combustion chamber. Many design considerations are taken into account in the procedures for building one of these highly sophisticated mechanisms. With many different forms and applications, these engines can be used from propelling large scale marina equipment to smaller scale house work items to everyday automobiles. This section goes into detail about the mechanics and design considerations involved with the setup, build quality, and general run quality of the components used in the power generation cycle of the four-stroke internal combustion engine.

##### *2.1.1 Piston and Crank Mechanisms*

The piston is arguably the most important part of an internal combustion engine itself and can be seen in Figure 2.1. The piston is designed to be strong, lightweight, and able to withstand great amounts of stress. The purpose of the piston is to transfer force from the combusting gas in the cylinder chamber to the crankshaft which generates usable torque. As the piston moves in an

upward motion, a counterweight on the crankshaft is able to force the piston upward upon initiation of the engine cycle. An adverse pressure gradient from the crankcase housing to the combustion chamber also slightly helps drag the piston to Top Dead Center (TDC) upon completion of the exhaust stroke. As the pressure in the chamber reaches its peak when the combustion process takes place, this generates a force spread across the piston head area forcing the motion in a linear downward direction. This action's efficiency of linear downward motion is heavily reliant on the lubrication and the tribological interaction of the piston and the cylinder wall, which is the focus of this work.

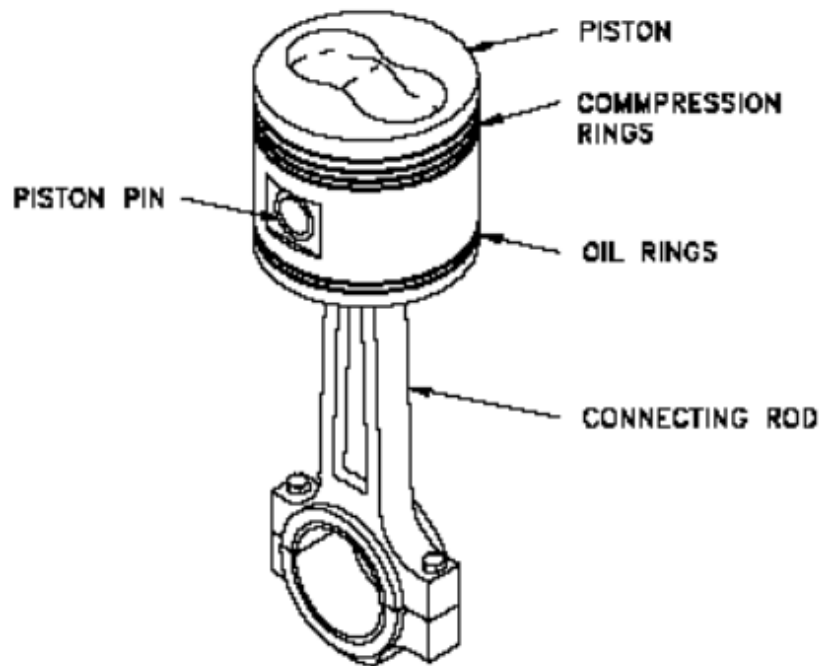


Figure 2.1: Piston components [21]

The connecting rod is mounted to the crankshaft by means of a radial bearing. This rotary element is designed to support large axial loads that are transmitted between the two elements. This hydrodynamic bearing is able to eliminate large amounts of friction that would normally be a problem. The lubricant acts as a full film which is able to divert this heat created from friction away from the crankshaft. This rotating combination of the piston and the connecting rod has to be strong and uniform in order to generate the torque required for work output. If the connection is otherwise beyond perfection, severe mechanical efficiency losses can occur.

### *2.1.2 Block, Head, and Pan Construction*

The engine block is the backbone in generating usable torque. Without a strong housing the combustion reaction is unable to take place. The stress yield points for steel must be able to withstand the cyclic stress generated by the piston. The engine pan is bolted to the engine block by several steel bolts. This pan keeps the crankshaft, crank arm, and other parts within a working medium protected from any external anomalies such as debris in the lubricants or undesired particles in the combustible air.

With such high temperatures being reached inside the cylinder, countermeasures are taken in order to cool the engine block. Two methods may be used, one is passive cooling and the other is active cooling [22]. Extended surface fins are one example of passive cooling. Extruded fins seek to increase the heat transfer rate between the cylinder and the ambient air by increasing the amount of free convection able to act on the surface area of the engine block. The heat generated from the combustion process is carried by way of conduction to the surface of the fins where the

free convection air is then able to lower the convective heat transfer coefficient. This system is typically found on smaller internal combustion engines. Automobile engines use active cooling. Active cooling involves the use of a mechanical system to force a coolant through the engine block. A water pump, powered by a belt from the crankshaft, supplies the pressure to drive the coolant around the system and through a liquid to air heat exchanger, also known as a radiator.

The proper operating temperature range also greatly affects the ignition timing. If the ambient air temperature is beyond normal operating conditions the cylinder will heat up unnecessarily and pre-ignition can occur. Likewise if the ambient air temperature is far too cold the sparkplug can produce undesired carbon deposits around the central electrode. Even worse, the spark could still fire and the carbon deposits can create a delay which results in the spark and piston mistimed; this is engine knock.

### *2.1.3 Cylinder Geometry*

Cylinder geometry is designed to take into account many factors. Of which the most important are squish, tumble, and swirl. These three factors all deal with increasing the burn rate of combustion in an effort to increase volumetric efficiency [22]. The top of the combustion chamber is rounded, as seen in Figure 2.2 in order to give the incoming air angular velocity, this helps in generating swirl, which gives a faster burn rate and therefore a higher volumetric efficiency.



Figure 2.2: Cylinder geometry to induce angular velocity

### *2.1.3.1 Squish and Swirl*

As the piston moves towards TDC at the end of the compression stroke, the gas mixture at the outer edge of the cylinder walls is forced radially inward. This radially inward motion of the gas mixture is called squish. This fluid process adds to the mass motion within the cylinder, in order to help spread the flame front faster, as will be seen in greater detail in this section swirl is generated by the onset of air from the port inlet into the combustion chamber. Air is forced throughout the chamber by the downward motion of the piston. As the inlet valve is offset from the center axis of the chamber, and due to the helical nature of the walls, this forces the air into the combustion chamber with an angular momentum. This downward angular “controlled” turbulence motion is what swirl refers to. Other engines may have more design configurations than just a

piston chamber assembly, such as a hemi-spherical valve arrangement, as seen in Figure 2.3 or even air passages that induce swirl before the air enters the chamber. All of which seek to increase the volumetric efficiency of the engine. However too much swirl is bad and reduces volumetric efficiency as well.

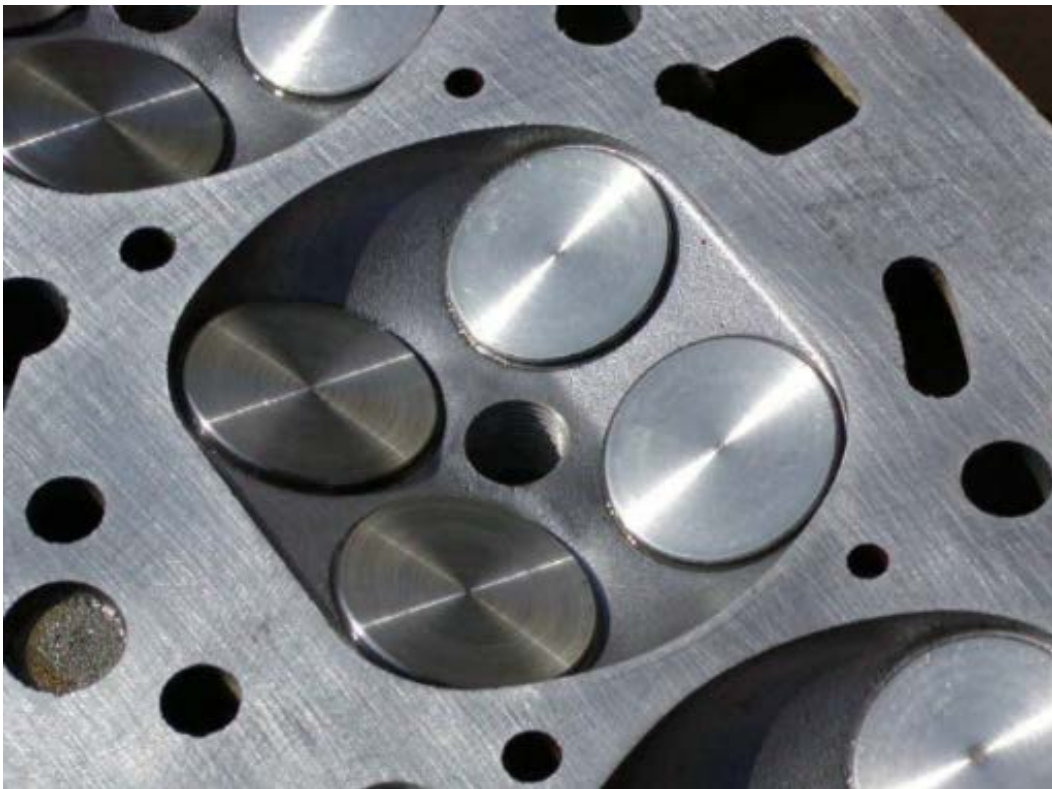


Figure 2.3: Hemi-spherical nature of combustion chamber to induce swirl [23]

### 2.1.4 Ignition

The spark plug is the mechanism that initiates the reaction inside the combustion chamber. As the electrons on both sides of the spark plug bridge, seen in Figure 2.4, build up due to a periodic magnetic field, the potential difference grows. Once this voltage potential exceeds the dielectric strength of the air and gas between the bridge, this gas becomes ionized. The ionization of this gas becomes the initiation of the chemical combustion reaction due to a dramatic difference in heat. This intense heat fueled reaction then generates the flame front in the cylinder (Section 2.1.6).



Figure 2.4: Spark plug electrode bridge [24]

### *2.1.5 Balancing*

Having a completely balanced internal combustion engine is virtually impossible even with an even numbered of cylinders. This only makes the design for the rotating machinery that much more vital for the longevity of its use. In accordance with Newton's Second law of motion, an object that has mass and velocity also carries momentum. Expressed mathematically in terms of its linear momentum, in an inertial reference frame, and the control volume being the combustion chamber, Reynolds Transport Theorem may be used to describe the piston's force.

As the piston speed is directly proportional to the crankshaft speed, so are the transmitted forces. When the piston head is reaching TDC its velocity must reach zero in order for it to change directions. Its momentum is slowed and eventually stopped by the crankshaft. This process is the same when the piston reaches Bottom Dead Center (BDC). Its momentum must completely change direction before alternating directions linearly.

This sudden transfer of momentum from the piston to the crankshaft causes ever so slight deformations acting on the crankshaft similar to a cantilevered beam. As the crankshaft deflects it creates a frequency from which many deflections (one while the piston is at TDC and one while the piston is at BDC) occur in a specified length of time. In this vibrating system, the point where the forces cause the oscillations in the crankshaft to grow phenomenally is called the resonant frequency. Resonant Frequency is a crucial part when it comes to engine design, and if not designed for properly can lead to catastrophic failures in the materials used.

### 2.1.6 The Flame Front

The flame front in an internal combustion engine bridges the burnt gas from unburnt gas by a high velocity pressure differential reaction [25]. The kernel initiates from the bridge in the spark plug. Generating higher swirl ratios and squish will create a hotter and faster flame front dependent on the engine speed. The angle of the crankshaft at ignition is directly related to the angle at the start of combustion through

$$\theta_{Start\ of\ Combustion} - \theta_{Ignition\ Point} = \theta_{Ignition\ Delay} \quad (1)$$

This equation states that the crank angle at the moment the flame is visible minus the crank angle when the sparks fires gives the crank angle of the ignition delay.

A crucial part in flame front design is the location of the spark plug. If the spark plug is at the outer edge of the cylinder, the flame front travels only in one direction thus generating a larger than normal burn rate velocity and impacts the cylinder wall with ferocious momentum [25]. After many cycles this constant bashing against the wall can cause the spark and piston to be out of synchronization, thus leading to engine knock.

Some engine designs have the spark plug directly above the center of the piston in order to ensure an isotropic flame front throughout the combustion chamber. As the flame comes to a termination along the cylinder walls not all the fuel-air mixture is combusted. The end gas is still slightly compressed however and can sneak into crevices, as will be seen in Section 2.1.7.2. The burned gas as a function of crank angle can be modeled using the Wiebe function [25] given as

$$x_{b(\theta)} = x_r + (1 - x_r) \left\{ 1 - \exp \left[ -a \left( \frac{\theta - \theta_s}{\theta_d} \right)^n \right] \right\} \quad (2)$$

where  $x_r$  represents the unburnt residuals,  $\theta_s$  represents the crank angle at the start of combustion, and  $\theta_d$  represents the crank angle duration. The combination of these parameters gives the amount of charge left in the chamber undisturbed by the flame front.

### 2.1.7 Gas Dynamics

As seen in analyzing squish and swirl as well as the flame front, gas dynamics plays an extensive role in contributing to an engines efficiency and run quality.

#### 2.1.7.1 Air and Fuel Flow

Clean air is a necessity for a quality combustion reaction. Air enters by way of the filter and travels through the carburetor where it mixes with the gas to travel past the choke. The choke limits the allowable mass flow rate that gets through to the combustion chamber. The fuel is mixed with the air at the choke valve and is governed by the venturi effect [25], resembling a converging diverging nozzle. In order for the gas to flow through the venturi there has to be a pressure differential as stated in the mass flow equation:

$$\dot{m}_{fuel} = C_{d_{jet}} A_{jet} [2 \rho_{fuel} (p_0 - p_{throat})]^{\frac{1}{2}} \quad (3)$$

where  $C_{d_{jet}}$  is the discharge coefficient of the jet and accounts for the viscosity of fluids,  $p_0$  is the stagnation pressure, and  $p_{throat}$  is the pressure at the throat.

With the choke valve wide open the mass flow rate of air through the intake dramatically increases while with a completely closed choke virtually no air is able to get through. Upon start-up, the choke valve is in the full open position in order to allow the initiation of combustion with

more air and fuel as this requires significantly more work being done on the piston. That being said, upon ignition and start-up the throttle is lowered in order to close the choke valve slightly as the engine does not need to be run at wide open throttle in most automobile cases. This comes from the help of the counter weight on the crankshaft that help keeps the piston in constant motion along with the combustion inside the cylinder chamber forcing the piston down.

Keeping the throttle in a moderate position between fully open and closed also increases the volumetric efficiency of the engine. If not enough air is able to flow into the cylinder there is wasted space and energy inside the combustion chamber. Likewise, if there is too much air the unburned residuals will be higher at the completion of combustion thus leaving more wasted fuel and air inside the cylinder at the start of the next stroke.

#### 2.1.7.2 Exhaust Flow

For a new cycle to begin in the combustion chamber, the unburnt gas must be forced out of the cylinder. As the cylinder travels from BDC to TDC the exhaust port is opened thus expelling the used gas into a series of tubes. These tubes channel the exhaust to the muffler which thus expels the used chemicals to the environment. If the flow is non-choked the mass flow rate past the outlet valve becomes

$$\dot{m} = \frac{(C_d A) p_o}{\sqrt{R_{bg} T_o}} \left( \frac{p_t}{p_o} \right)^{\frac{1}{k}} \left\{ \frac{2k}{k-1} \left[ 1 - \left( \frac{p_t}{p_o} \right)^{\frac{k-1}{k}} \right] \right\}^{\frac{1}{2}} \quad (4)$$

where  $T_o$  is the reference stagnation temperature,  $p_o$  is the reference cylinder stagnation pressure as a function of crank angle,  $k$  is  $\frac{c_p}{c_v}$  inside the cylinder,  $p_t$  is the pressure at the throat,  $C_d$  is the

discharge coefficient and is roughly 0.7 for exhaust valves, and  $A$  represents the minimum curtain area [25]. The foundation of this equation is based on a pressure differential sufficient enough between the exhaust pressure and the pressure at the throat to drive the mass flow rate. Without this pressure difference, there would be no exhaust flow.

Approximately 9% of the fuel that enters the combustion chamber is not burned in the primary combustion process. About 7% of that will eventually burn and the remaining 2% is emitted. This 7% consists of 5% due to the fuel trapped in crevices such as spark plug pockets, head gaskets, and the piston ring, while the 2% is absorbed into the liquids and solid deposits [22].

#### *2.1.8 Piston Ring – Pack*

As previously mentioned the piston is one of the most important parts of generating usable work. This cyclic nature of the piston would normally melt the piston rings and crankshaft bearings without the aid of a lubricant or lubrication. This interaction of the piston, piston ring, and cylinder wall is crucial in not only generating usable work but also efficient work [26], a schematic of the interactions can be seen in Figure 2.5. As the piston traverses linearly downward in the bore from TDC to BDC, the piston ring is forced at an angle due to its inertial resistance. A similar situation happens in moving from BDC to TDC. A detailed study of the interactions of the piston ring, cylinder wall, and lubricant supporting the two is presented in this work for the development of a numerical flow model to predict the failure of these components, which can lead to the design of superior component materials and even geometry.

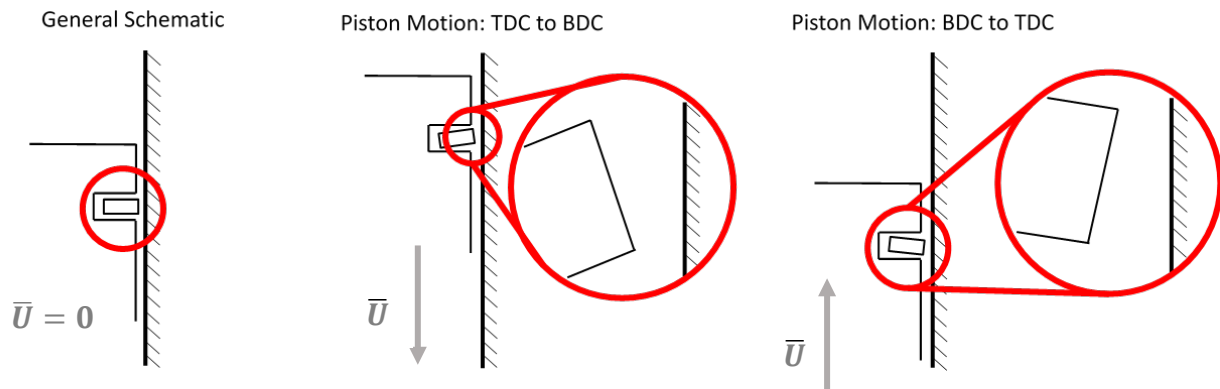


Figure 2.5: Piston ring and cylinder wall tribological interaction

## 2.2 The Reynolds Equation

The Reynolds equation is a second order linear partial differential equation governing the generation of hydrodynamic pressure in thin viscous film bearings [27]. It is commonly the equation of use in modeling the viscous flow of lubricant between the cylinder wall and piston ring. The Reynolds equation can be used to predict how surface roughness effects bearings in elasto-hydrodynamic contact. It can account for how the flow transport and impedance is altered due to local flow regions near peaks and in valleys of the surface roughness features. This additional flow transport is only seen in the sliding contacts of two rough surface bearings [26]. The Reynolds equation is derived from the Navier-Stokes equations, which are derived from Newton's second law paired with the conservation of momentum. There are many forms of the Reynolds equation, and each form is based on the variations of physical mechanisms involved in the system. The general form of the Reynolds equation, which will be derived in greater detail later on, for a thin, viscous, incompressible, Newtonian, laminar fluid is

$$\frac{\partial}{\partial x} \left( \frac{h^3}{12\mu} \frac{\partial p}{\partial x} \right) + \frac{\partial}{\partial z} \left( \frac{h^3}{12\mu} \frac{\partial p}{\partial z} \right) = \frac{\bar{U}}{2} \frac{\partial h}{\partial x} + \frac{\partial h}{\partial t} \quad (5)$$

### 2.2.1 Application to Power – Cylinder Components

Among power cylinder components, the Reynolds equation has been seen more commonly used in a one dimensional form and a two dimensional axisymmetric form. For example Ting and Mayer [26] use the one dimensional axisymmetric form to analyze the effect of piston ring lubrication on cylinder bore wear analysis. Similarly Chong, et. al. [28] use the one dimensional form of the Reynolds equation in analyzing cavitation induced starvation for the tribological conjunctions in piston ring-packs. Furuhamu [29] expands this to a two dimensional piston ring analysis in analyzing the continual dynamics of piston ring lubrication. He derives a model for average film thickness between the cylinder wall and piston ring as a function of crank angle. Akalin and Newaz [30] use the Reynolds equation to perform a two dimensional unsteady analysis on piston ring-cylinder bore friction modeling in the mixed lubrication regime. The three dimensional form of the Reynolds equation has not been used among power cylinder components as it pertains to specific applications [31, 32].

### 2.2.2 Alternate Applications

The Reynolds equation can also be used to calculate the hydrodynamic pressure among other machine bearings, such as journal bearings, slider bearings, and or gas lubricated bearings. With this, Reynolds equation can also be written in its compressible form as

$$\frac{\partial}{\partial x} \left( \frac{\rho h^3}{12\mu} \frac{\partial p}{\partial x} \right) + \frac{\partial}{\partial z} \left( \frac{\rho h^3}{12\mu} \frac{\partial p}{\partial z} \right) = \frac{\bar{U}}{2} \frac{\partial \rho h}{\partial x} + \frac{\partial \rho h}{\partial t} \quad (6)$$

The Reynolds equation can also be used for not just Newtonian fluid, but also non-Newtonian fluids. Peiran and Shizhu [33] derive a form of the Reynolds Equation for non-Newtonian thermal elasto-hydrodynamic lubrication. Dien and Elrod [34] then combine these two applications and apply the generalized Reynolds equation for non-Newtonian fluids to a journal bearing. The non-Newtonian Reynolds equation model was then applied to not only laminar flow, but also transitional flow and turbulent flow regimes by Metzner and Reed [35]. Mitsuya et. al. [36] sought to incorporate not only roughness, but also slip past the asperities into an average Reynolds equation. Wu [37] then took this slip model and applied it to the compressible Reynolds equation (Eq. (6)).

Having seen how the Reynolds equation is able to be applied and modified to solve for hydrodynamic pressures between various cases, the case in question is among power cylinder components. The form of the Reynolds equation derived is namely involving statistical flow factors which modify the Reynolds equation to account for various surface roughness in the full-film lubrication regime.

### *2.3 Flow Factors*

Flow factors are a method for determining roughness effects on lubrication flow in the full film lubrication regime, the mixed lubrication regime, or boundary regime. The three major flow regimes are composed of thin viscous films that can be categorized by the Stribeck curve shown in Figure 2.6. The Stribeck curve is a plot of coefficient of friction versus the dimensionless bearing

number. The Stribeck curve is used to determine the transitions between the flow regimes. On the left side of the Stribeck curve is the boundary lubrication regime where there exists aggressive surface abrasion and wear is high, as seen in Figure 2.7. On the right side is the hydrodynamic regime where the surfaces are completely separated by a full film. Surface roughness plays a large part on load carrying capacity among all of these regimes.

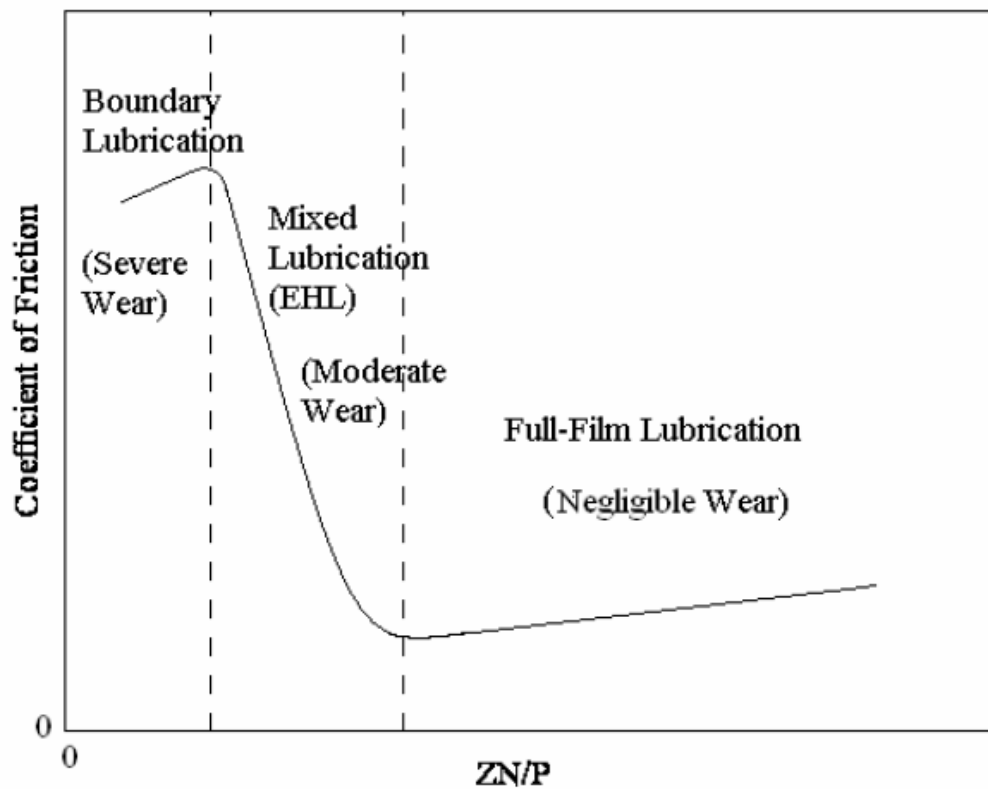


Figure 2.6: Stribeck curve with marked lubrication regimes [38]

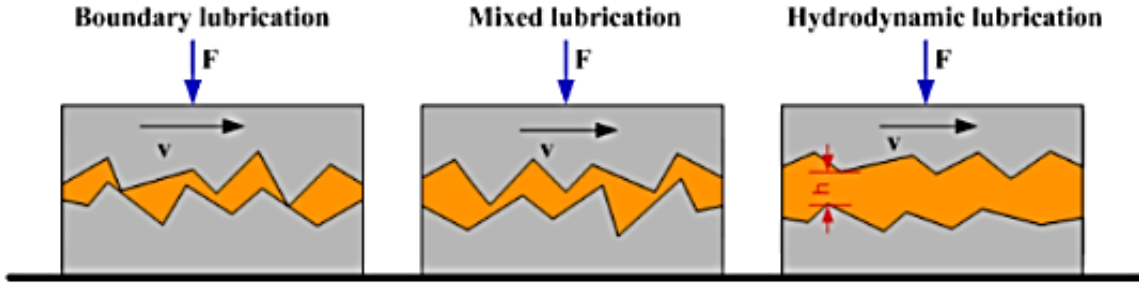


Figure 2.7: Depiction of various lubrication regimes [39]

Lubricants interact not only at the macroscopic level, but also at the microscopic level; which is especially important for the surfaces themselves. While the Reynolds equation (Eq. (5)) can be used to solve for pressure at each asperity on a rough surface, this method is tiresome and computationally arduous. Surface roughness plays a large part in the hydrodynamic flow regime. It is computationally and numerically difficult to model the flow past individual asperities. Asperities of each surface in or near contact play a large role in the influence on lubrication flow. For this very reason the Reynolds equation is modified by the use of pressure and shear flow factors.

Patir and Cheng [1, 40] were the first to determine the effects of surface roughness on the flow between three-dimensional surfaces. The flow effects were determined through the use of statistical flow factors. The flow factors were incorporated into the Reynolds equation (Eq. (5)) through

$$\frac{\partial}{\partial x} \left( \varphi_x \frac{h^3}{12\mu} \frac{\partial p}{\partial x} \right) + \frac{\partial}{\partial z} \left( \varphi_z \frac{h^3}{12\mu} \frac{\partial p}{\partial x} \right) = \frac{\bar{U}}{2} \frac{\partial h}{\partial x} + \frac{\bar{U}}{2} \frac{\partial \varphi_s}{\partial x} \quad (7)$$

where  $\varphi_x$  and  $\varphi_z$  represent the effects the asperities have on the pressure driven flow in the absence of any surface movement or shearing. While  $\varphi_s$  represents the effects the asperities have on the shear driven flow, in the absence of any pressure induced gradient.

Flow factors are a method used to statistically model a rough surface as a smooth surface. As the surface specific topography can be found through measuring tools, the flow past and around these points can then be statistically modeled. These models can then be used in conjunction with the Reynolds equation for a more accurate pressure solution which takes into account surface texturing.

Patir and Cheng derived their flow factors from numerically generated surfaces with known statistical properties, and then used empirical flow factor equations to modify the Reynolds equation. In contrast to Patir and Cheng, this work presents flow factors that are derived from actual measured surfaces, followed by the modification of the Reynolds equation with the surface specific empirical flow factor equations. This allows for a more accurate analysis of the pressure and shearing effects surface specific topography has on power cylinder components.

The Reynolds equation is seen to govern the behavior of the mean pressure in rough bearings and thin film interacting surfaces. However, a more accurate model taking into account surface topography layout can be used. The flow factors set forth by Patir and Cheng are a very reliable statistical model, however newer techniques are utilized to derive empirical models that may have improved accuracy among power cylinder components.

## *2.4 Cavitation*

Cavitation is the spontaneous formation of pressure free voids or zones and is the result of placing excessive shearing and tensile forces on a lubricant. The lubricant is spontaneously able to overcome the molecular bonds holding the fluid together, thusly creating space between them and creating a negative pressure zone that is a two-phase composition. Cavitation can also happen when the pressure in a fluid spontaneously drops. This sudden drop in pressure is caused by the fluid shearing quicker than it can react which leaves trails of negative pressure. This is damaging to the lifespan of mechanical components as the cavitation zones collapse and implode on the surfaces causing undesired cyclic stress.

### *2.4.1 Cavitation Models*

Cavitation is an area that has not gained too much interest among power cylinder components until recent years. Several cavitation models have been formulated and or implemented in conjunction with calculating more accurately the total hydrodynamic pressure a fluid film undergoes among tribological components. A few cavitation models that have been integrated with power cylinder components are:

1. Universal Cavitation Model [41]
2. Jakobsson, Floberg, and Olsson (JFO) model [42]
3. Flow Separation Model [43]
4. Floberg Model [44]
5. Swift Stieber Model [45, 46]

Yang and Keith [47] uses the universal cavitation model in examining the elasto-hydrodynamic regime for piston ring lubrication. This combines the Rayleigh-Plesset equation for physical bubble dynamics, into a model containing cavitation which accounts for flow continuity of mass. The resulting equation is:

$$R \frac{d^2 R}{dt^2} + \frac{3}{2} \left( \frac{dR}{dt} \right)^2 = \left( \frac{p_{cavity} - p}{\rho_l} \right) - \frac{4\nu_l}{R} \frac{dR}{dt} - \frac{2S}{\rho_l R} \quad (8)$$

where  $\nu_l$  represents the kinematic viscosity of the fluid,  $S$  is surface tension between the boundary of the cavity and the fluid,  $\rho_l$  is the density of the liquid, and  $p$  is the fluid pressure far from the bubble. This relates the time rate of change of the bubble radius,  $R$ , and the bubble pressure,  $p_{cavity}$ , to the fluid properties while holding true to conservation of mass [48].

The JFO model has received much of the attention. The JFO model was initiated by Jakobsson and Floberg [49] and further extended by Olsson [42]. Their model can properly treat the spontaneous nature of the cavitation film rupture and the film reformation. Elrod [50] sought to simplify the model into a universal governing equation that is valid for both the fully hydrodynamic regime and the cavitation voids. He introduced a numerical analysis that enabled the prediction of the cavitation region. Paydas and Smith [51] were the first to apply Elrod's universal algorithm to a practical application, namely involving journal bearings [52].

Ma [53] was the first to apply the simplified JFO model to the study of piston ring lubrication [52]. He found that the operating performance of the piston ring is largely influenced by lubricant starvation. Specifically as starvation increases, the conditions that could lead to gaseous blow-by are greatly enhanced [53]. The JFO model can be directly incorporated into the Reynolds equation and therefore has had a large interest in the development of piston ring

lubrication modeling considering cavitation. The accuracy of the hydrodynamic pressure is still just as accurate. This led Harp and Salant [54] to derive a density flow factor that was derived experimentally and fit with an empirical equation similar to the pressure and shear flow factors as mentioned in Section 2.3. This density flow factor is new and specific to the cavitation model. It accounts for the reduced density in the control volume due to the pockets of air [54]. The average Reynolds equation is kept in the same form as in Sections 2.2 and 2.3 except it improves the accuracy of the hydrodynamic pressure calculations by including the effect of inter-asperity cavitation.

#### *2.4.2 Cavitated Region Boundary Conditions*

There are several methods for setting the boundary conditions of the cavitated regions of the lubricant. Sommerfeld [55] derived the hydrodynamic pressure solution for the journal bearing in 1904 and the solution can be seen in Figure 2.8(a).

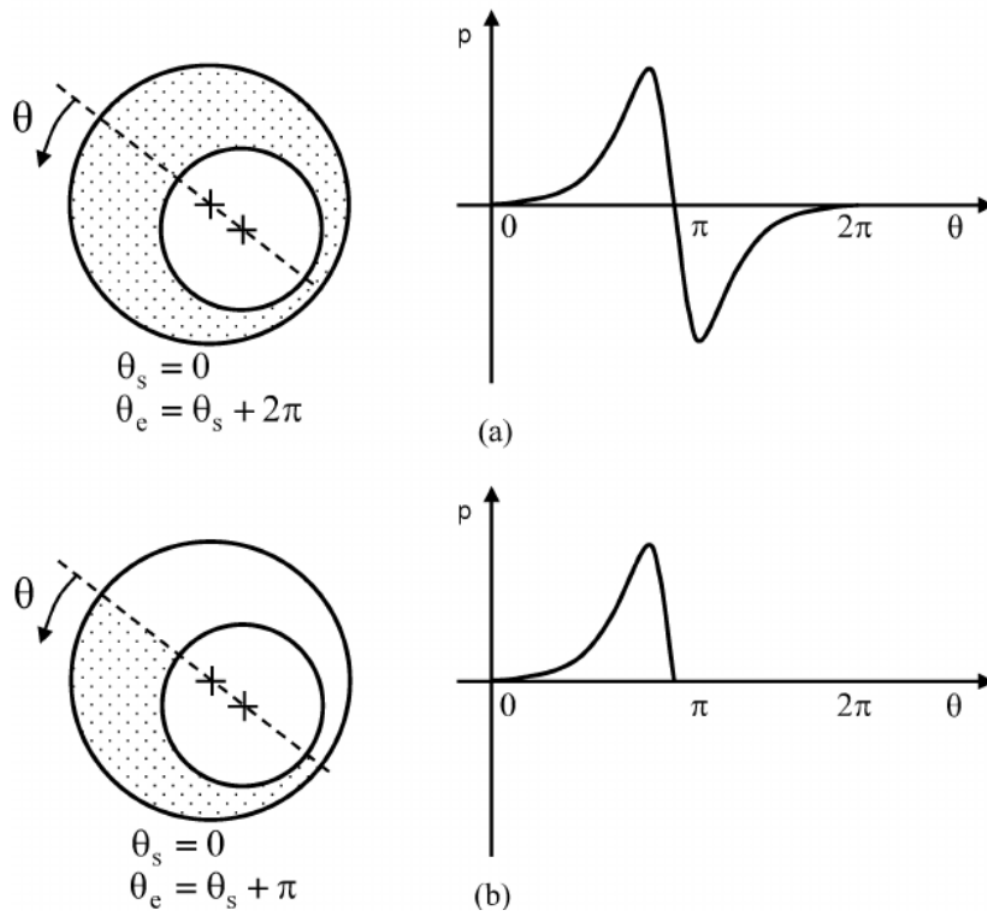


Figure 2.8: (a) The full-Sommerfeld boundary conditions and (b) Half-Sommerfeld boundary condition [28]

This approach is unrealistic in the application among power cylinder components as it requires the lubricant to sustain very large negative hydrodynamic pressures for an extended period of time and will lead to an under prediction of the hydrodynamic load carrying capacity [56]. When gaseous cavities form in a lubricant, the flow rate at the cavitation boundary must increase to maintain the mass flow continuity of the lubricant due to the void regions. The JFO model requires that there is zero pressure gradient and mass is conserved at the rupture and reformation boundaries

of the cavitation zones. The Gmbel solution, also known as the half-Sommerfeld solution, realizes that a lubricant cannot sustain large negative pressures over extended periods of time and as a result simply neglects the negative pressures [57], this can be seen in Figure 2.8(b). This solution condition, however, does not satisfy the mass flow continuity and is rarely used among power cylinder components. A popular boundary condition is the Reynolds condition formulated by Swift [46] and Steiber [45], where boundary conditions are applied to the cavitation boundary and are

$$p = p_{cavity} \quad , \quad \frac{dp}{dx} = 0 \quad (9)$$

where  $p_{cavity}$  is the saturation pressure of the gaseous cavities. This condition is preferred over the Sommerfeld or half-Sommerfeld solution as the mass continuity is held across the cavitation boundary layer. This boundary condition can also be directly implemented with the Reynolds equation, and will be tested numerically in a later section.

There are other highly accurate cavitation models that deal in calculating bubble dynamics, however they deal primarily with the full universal cavitation model and are beyond the scope of this thesis. For completeness they are listed as follows

1. Singhal et al. Model [41]
2. Zwart-Gerber-Belamri Model [58]
3. Schnerr and Sauer Model [59]

More commonly, these cavitation models are utilized in Computational Fluid Dynamics (CFD) analysis using software packages such as ANSYS, ABAQUS, Star CCM, etc. due to their complexity.

## CHAPTER 3

### METHODOLOGY

#### *3.1 Measurement of Interacting Surfaces*

There are several methods for measuring precision surface finishes. Two general categories are contacting and noncontacting. For this thesis contacting methods were used and are the focus of the analysis. A stylus profilometer is under the category of utilizing contacting methods. A profilometer is a tool that's designed based on the principle of using the vertical motion of a stylus tip and transforming it into lateral surface heights. This rough surface measurement is utilized in the derivation of the surface specific flow factors. While this method was performed on power cylinder components, the method of deriving surface specific characterizations can be done with almost any engineered surface.

##### *3.1.1 Profilometer*

The use of a profilometer is one of the most common tools in measuring surface finish due to its accuracy, range of tribological uses, and cost. The stylus tip utilized in this work is made of diamond, has a tip radius of  $2\mu m$ , uses a static load of 10mg, and has a resolution of 1 nm. If the load of the stylus tip is too low and the velocity is too high, this may result in bouncing on the

surface and results in the loss and misreading of surface resolutions. In a similar fashion if the load is too high and the velocity too high, this results in abrasion of the tip on the surface, which leads to not only damage of the stylus but also the surface. Several issues can arise from the stylus tip. One is that the tip is relatively large in comparison with the smallest roughness features. Features may inadvertently be filtered as shown with the stylus tips in Figure 3.1.

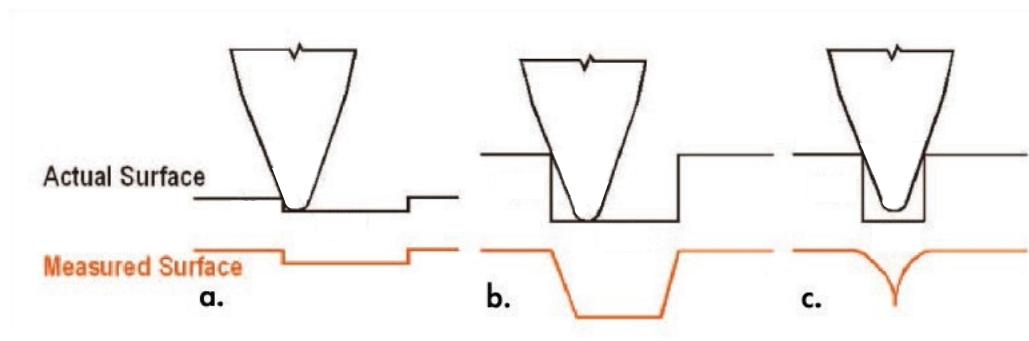


Figure 3.1: Influence of stylus tip on surface measurement [60]

Due to the sensitivity of the instrument, the profilometer is operated on a self-leveling pneumatic vibration isolation table. This ensures the steadiness of the machine when measuring the surfaces.

The current thesis used a rough surface sample cut out of a cylinder wall from an internal combustion engine supplied by Ford Motor Company. For the sample surface, 1,000 rows,  $1,000\mu m$  long were measured each spaced  $1\mu m$  apart, thus the length-to-width dimensions of the surface sample is  $1000\mu m \times 1000\mu m$ . The measured raw surface data for the cylinder wall measurements are shown in Figures 3.2 and 3.3.

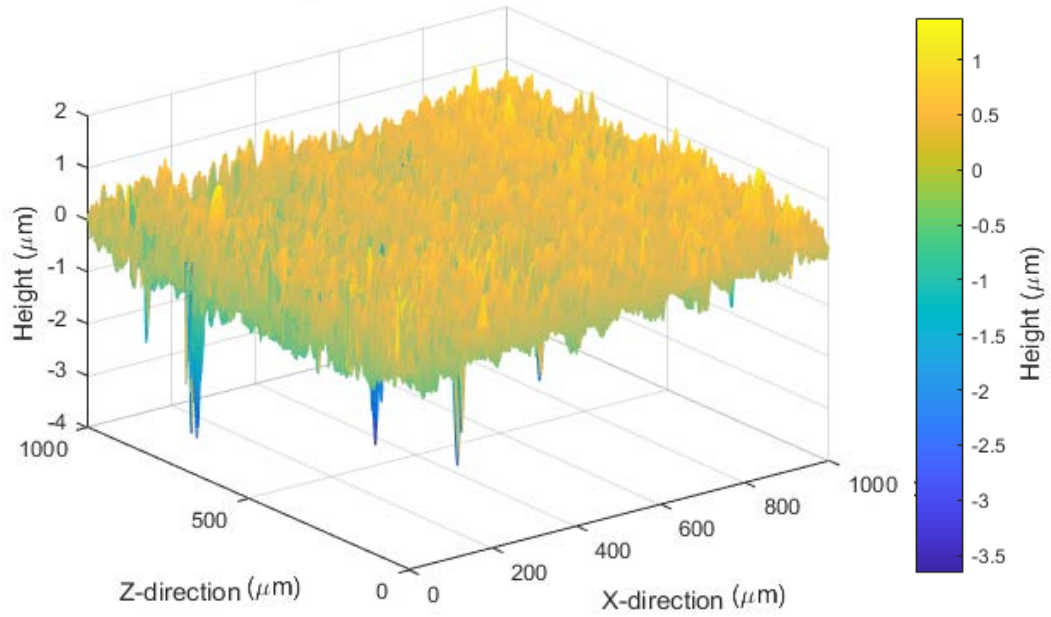


Figure 3.2: Current Production Engine Cylinder Wall (Isometric View)

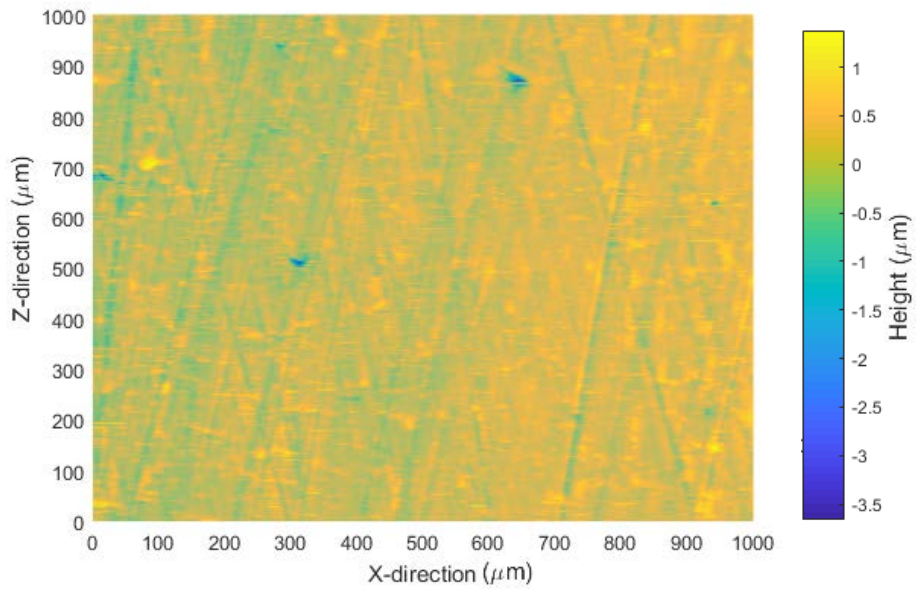


Figure 3.3: Current Production Engine Cylinder Wall (Top View)

### 3.1.2 Cylinder Wall – Level Data

With the raw data surveyed, the cylinder wall surface heights must now be leveled. In leveling the surface this ensures that the average surface height is set to zero, and can be expressed mathematically as

$$y_{leveled} = y_{unleveled} - y_{curve\ fit} \quad (10)$$

Due to the nature of the profilometer measuring each of the 1,000 rows individually, each row must be leveled separately. This ensures that each row's average is leveled at zero. If the whole surface was leveled at once this could filter out surface data from other rows. As the stylus traverses the surface in a single row there is an amount of error that arises as mentioned in Section 3.1.1. If all the surface heights were summed across the whole surface so would the error, thus each row is leveled separately to reduce the amount of error. With the cylinder wall surface data leveled with an average surface height centered at zero, attention is now shifted to the piston ring surface.

### 3.1.3 Piston Ring – Curvature

The opposing surface in question is the piston ring. The piston ring raw data and surface heights were sent directly from Ford Motor Company. The piston ring is from the same production engine, with the same length-to-width measurements. The surface and its heights can be seen in Figure 3.4.

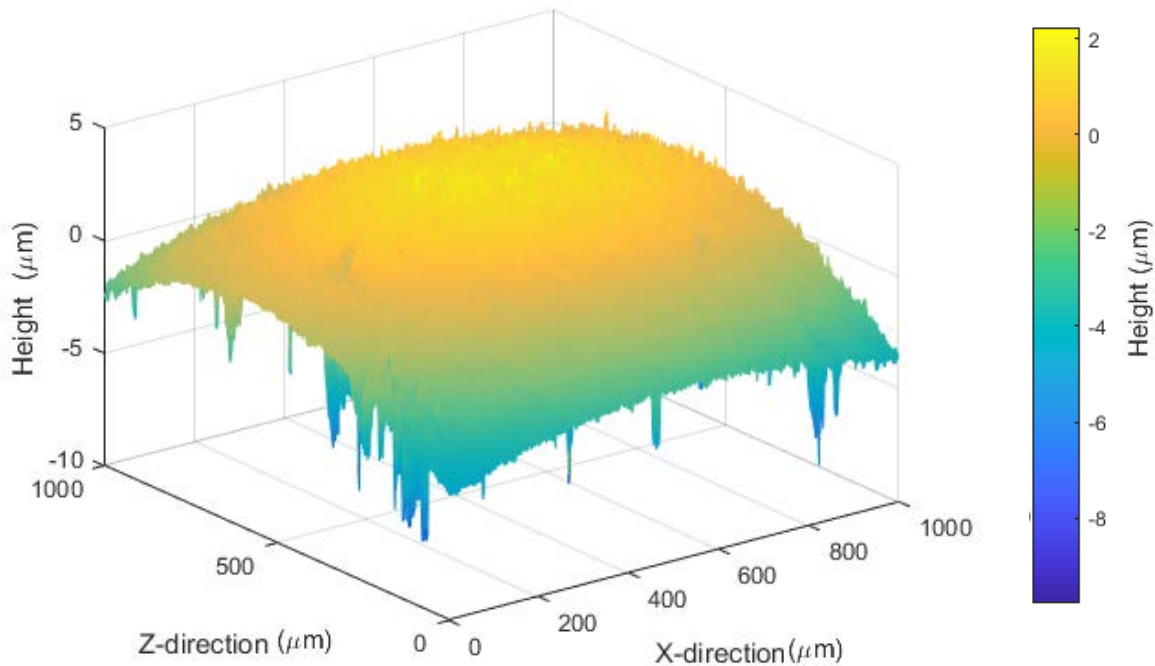


Figure 3.4: Piston ring with curvature (Isometric View)

In deriving surface specific flow factors from surface topography, only the surface features are needed. The geometry of the ring is not needed in the derivation. Later on the Reynolds equation will be seen to take care of the flow field geometry. In a similar fashion to the cylinder wall, in looking at the piston ring roughness, a leveled surface is desired. This includes fitting each row with a curve, finding the average surface height from the curve fit, then subtracting out the average. Figure 3.5 shows one of the rows of data curve fitted to a fifth order polynomial with coefficients that have 95% confidence bounds at every node. This procedure was iterated for each of the 1,000 rows of data to be leveled at zero. A side view of the entire piston topographic structure is seen as a comparison in Figure 3.6. In Figures 3.7 and 3.8 the piston ring can be seen without

any curvature after it has been removed. The piston ring now has no curvature and is leveled with an average surface height centered at zero.

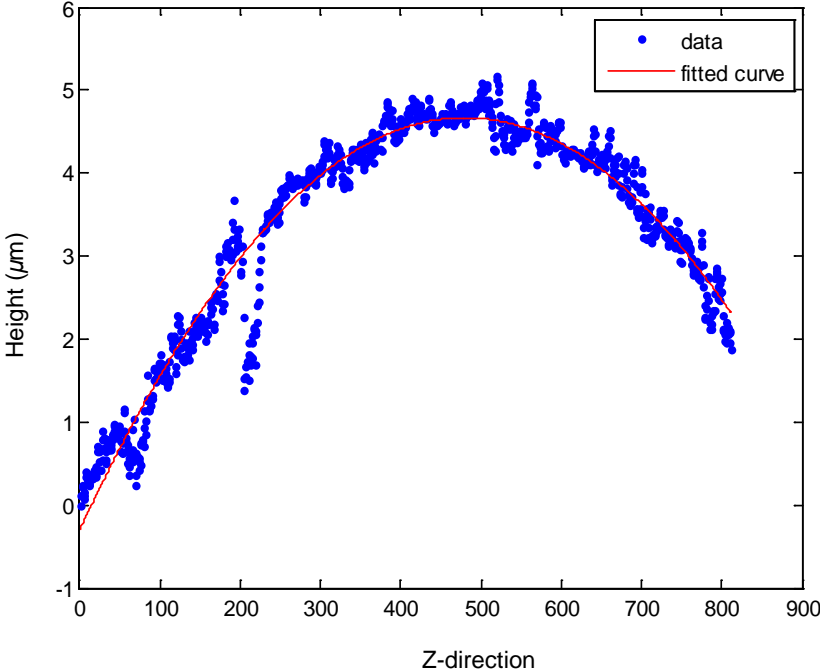


Figure 3.5: One row of measured data points on the curved piston ring

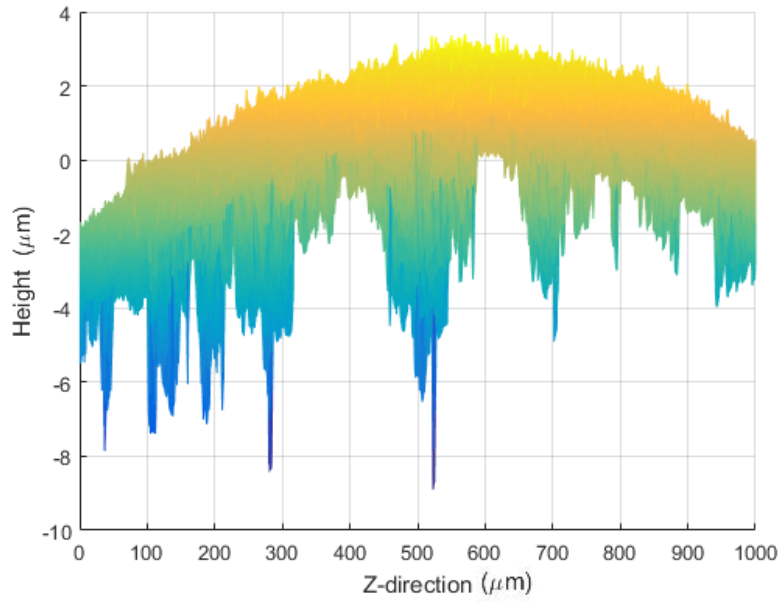


Figure 3.6: Side view of piston ring structure

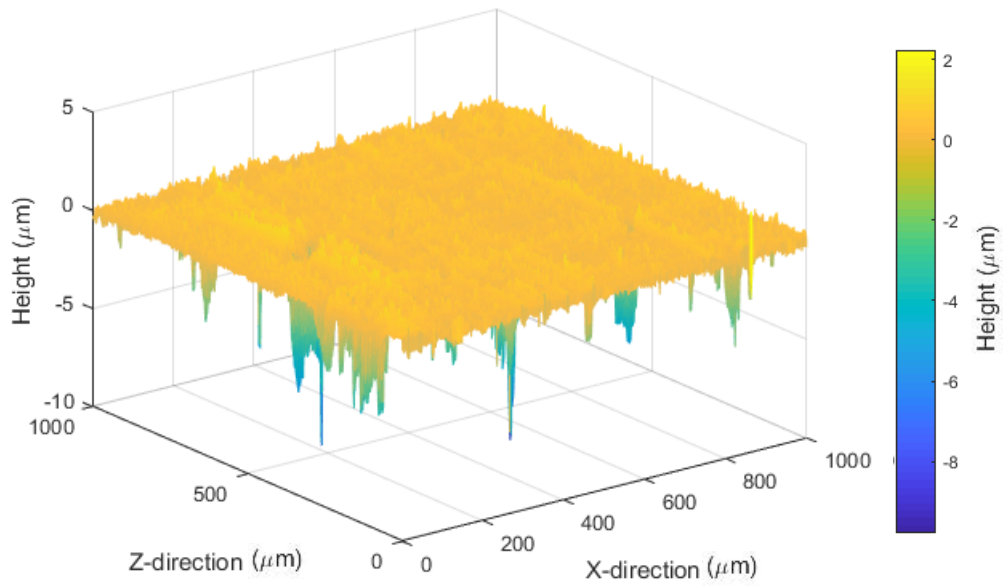


Figure 3.7: Piston ring without curvature (Isometric View)

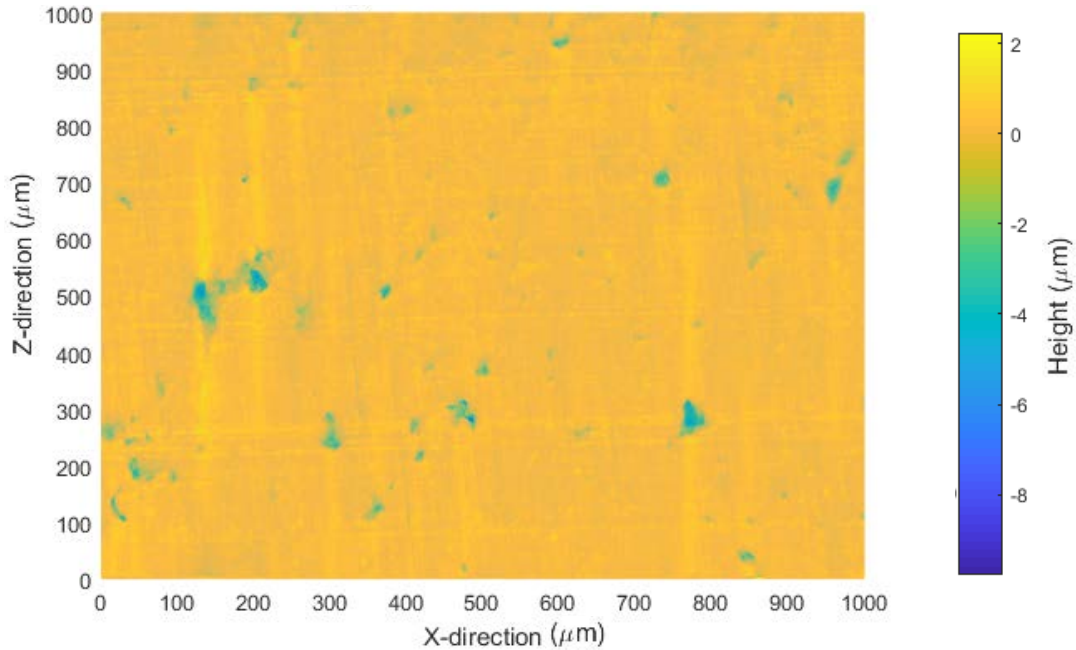


Figure 3.8: Piston ring without curvature (Top View)

### 3.1.4 Surface Topography

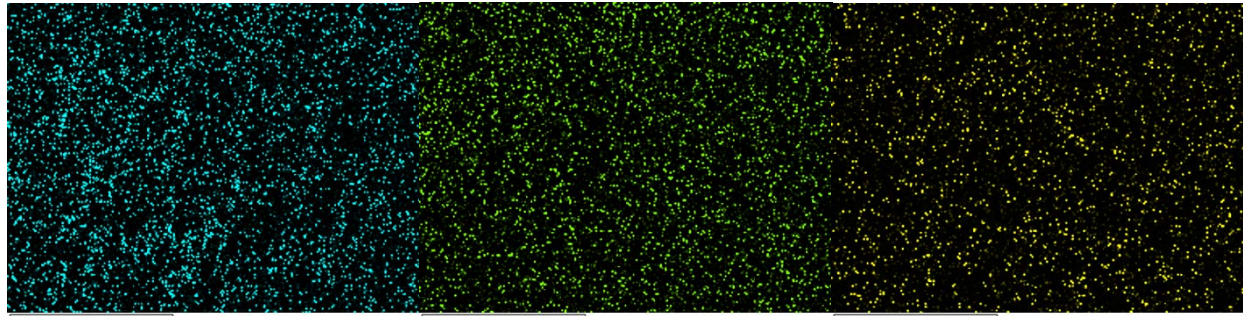
Surface topography is the key influence on the derivation of surface-specific flow factors. How the lubricant is conveyed past asperities is the basis of the empirical flow factor equations. The transversely oriented asperities hinder the flow of lubricant while longitudinally oriented asperities aid in the movement of lubricant. This is synonymous with the design of the engineered cylinder wall surface where lubricant is channeled through the grooves to aid in the lubrication of the piston ring-pack. The local hydrodynamic pressure on these rough surfaces is desired to have an average flow model predicting the average hydrodynamic pressure across a set of surfaces.

#### *3.1.4.1 Cylinder Wall Features*

The cylinder wall features play a major role among power cylinder components. Namely to contain the combustion reaction inside the engine bore. As the piston's connecting rod traverses around the crankshaft the rotational dynamic movement is transferred into rectilinear movement by way of the piston and engine bore. The cylinder wall guides the piston from TDC to BDC, and vice versa, continually. As the piston moves in a rectilinear fashion several thousand times per minute, constant lubrication is required to prevent components from generating heat, by way of friction, causing significant wear and leading to mechanical failures.

The cylinder wall's capabilities of providing lubrication to the engine bore have greatly increased over the recent years. The cross-hatched pattern, seen in Figure 3.3, is engineered to better channel the lubricant along the direction of piston motion ( $x$  direction). As lubricant traverses through the grooves, additional hydrodynamic load support is generated due to the added conveyance of lubricant, as compared to a smooth cylinder wall surface. In analyzing the entirety of the cylinder wall around the engine bore, this hydrodynamic lift causes a pseudo steady-state model. Prior to the development of the cylinder wall lubricant grooves, the increase in hydrodynamic lift force on one side of the bore resulted in a decrease in hydrodynamic lift force on the opposing side of the bore. This lift force would reverberate several times back and forth in one combustion cycle causing the piston to shake within the chamber. The cylinder wall grooves aid in the result of a steady flow of lubricant and thus a more constant hydrodynamic load, instead of reverberating from one side to the other side, throughout the piston cycle.

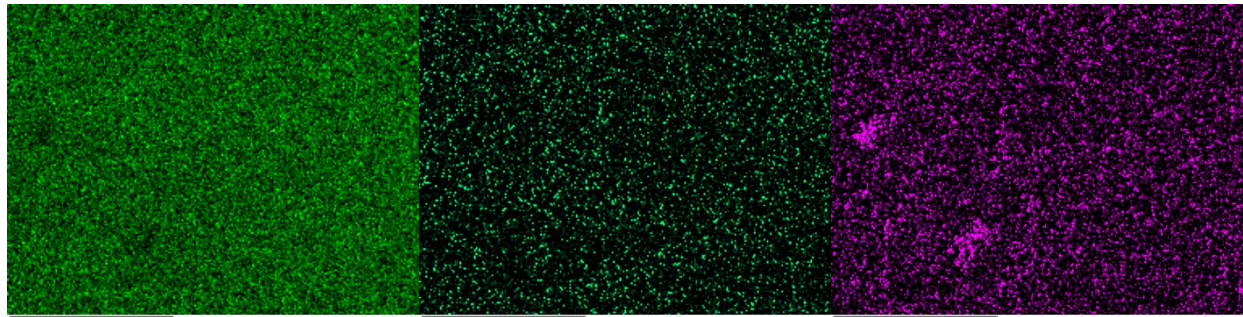
For the cylinder wall the materials used are gray cast iron with controlled hardness and microstructure to achieve optimum cylinder liner characteristics. This hardness resists deformations due to mechanical contacts on the cylinder wall by the piston ring. The chemical breakdown of the cylinder wall can be seen in Figure 3.9.



(a)

(b)

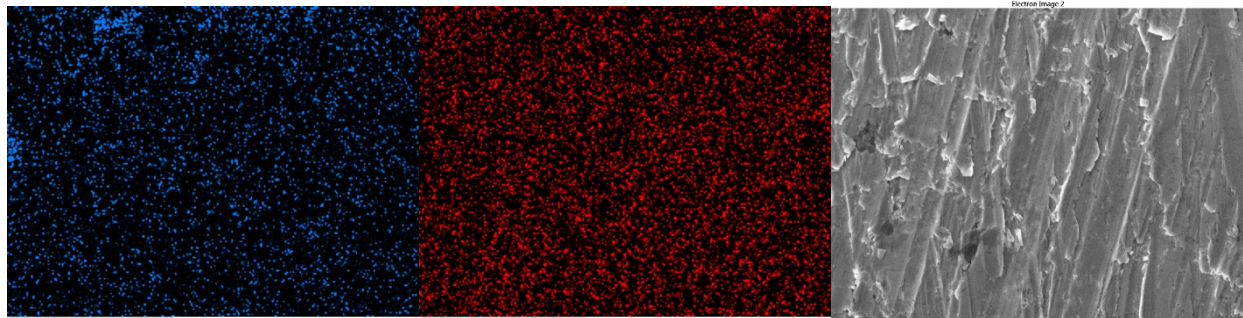
(c)



(d)

(e)

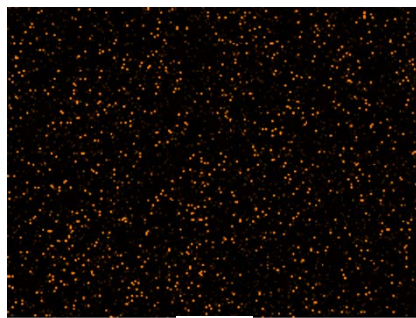
(f)



(g)

(h)

(i)



(j)

Figure 3.9: Chemical make-up of cylinder wall to improve lubrication and hardness effects. In (a) is Carbon, (b) is Chromium, (c) is Copper, (d) is Iron, (e) is Manganese, (f) is Oxygen, (g) is Phosphorus, (h) is Silicon, (i) is SEM of cylinder wall, and (j) is the Zinc map

\*Special thanks to Ford for supplying the photos

In Figure 3.9, black represents space between the chemical concentration areas, while each color represents that particular element's concentrated area. Each sample has length-to-width dimensions of  $150\mu\text{m} \times 150\mu\text{m}$ . It can be seen from Figure 3.9(d) that the cylinder wall is primarily iron; seen from the prominent amount of color compared to black. Also, there are certain spots on the cylinder wall where the elements are concentrated in porous regions, as seen by the concentration of color in Figures 3.9(f) and 3.9(g). These concentration spots can be seen in Figure 3.3 as craters where the surface height is below zero. Thus there are porous regions in the cylinder wall. There are also porous regions that are more prominent on the piston ring.

#### *3.1.4.2 Piston Ring Features*

Similar to the cylinder wall, the piston ring is also engineered for improved functional surface properties. The piston ring is given more porous features. These pores allow lubricant to nucleate providing additional hydrodynamic lift and load support. These pores are seen in Figure 3.8 as surface heights below the leveled surface. They serve as a similar function to the cylinder wall grooves where they are engineered to carry lubricant, thus increasing hydrodynamic load support. These porous regions prevent severe mechanical damage from the piston ring on the cylinder wall by ensuring there is a constant supply of lubricant on the piston ring surface. The reverberations from one side of the engine bore to the other side are also reduced for the same reasons mentioned in Section 3.1.4.1.

Tribological surface characteristics are very prominent in the mechanical success of power cylinder components and are often underestimated. These surface features are, and will be, seen to

have a large effect on lubrication of the cylinder wall and piston ring, not only by aiding in additional transport of fluid, but also the longevity of engine component life. These surface specific topographic features will be seen to have a major influence on the empirical flow factors.

### *3.2 Surface Roughness Directionality Characterization*

Many engineered surfaces are given certain roughness parameters whether on purpose or due to a manufacturing technique, such as turning or milling. In most applications a statistical description of the surface will be satisfactory by means of its first and second moments of the probability density distribution function along with its Root-Mean-Square (RMS) roughness [61]. However, in analyzing the relatively low tolerances that are involved with power cylinder components, such as the piston, ring, and cylinder wall, more adequate surface characterization techniques are required. The elementary correlation function may describe analytically the surface topography based on the correlation lengths [2].

#### *3.2.1 Auto-Correlation Function*

The auto-correlation function (ACF) reflects the profile of surface topography by relating the spaces between individual surface asperity heights. This is completed by relating a random signal to a delayed copy of itself as a function of delay [2]. The 2-D auto-correlation function provides a sufficient statistical description of a surface whose topography may be considered a general random process [62]. It is obtained by multiplying each asperity height by the height of another at a fixed horizontal distance farther along the profile. The horizontal distance starts with

an adjacent asperity and is iterated up to the length of the surface profile. Therefore the local asperities have more of an effect on each other than an asperity further away. This is very prominent under pressure driven flow and shearing of a fluid over asperities.

The average of the product over the 2-D surface length represents the auto-correlation function and can be expressed in its primary tensor notation as

$$\rho_{ii}(\lambda) = \frac{1}{N - \lambda} \sum_{i=1}^{N-\lambda} X_{ii}(l) X_{ii}(l + \lambda) \quad (11)$$

where  $X_{ii}(l)$  represents the measured surface profile and  $\lambda$  represents the variable horizontal distance between asperities. This can be visualized from the surface profile in Fig. 3.10.

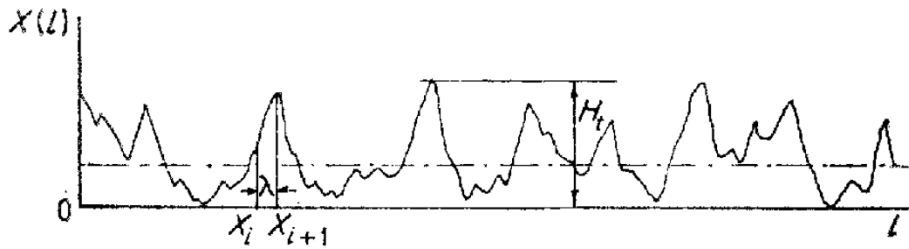


Figure 3.10: Surface profile of auto-correlation parameters [2]

In analyzing the 2-D auto-correlation function, on a 3-D surface, each row of asperities is correlated separately. Followed by averaging the correlations over the entire surface. This procedure is followed for both the  $x$  and  $z$  directions. Let  $\lambda_{0.5}$  represent the length at which the auto-correlation reduces to 50% of its initial value. Three cases are run to determine the correlation lengths for the cylinder wall surface, the piston ring surface, and the convoluted surfaces superimposed together through the principle of superposition. The cylinder wall asperity heights,

along with the piston ring asperity heights were superimposed to form one rough surface that incorporates all surface topography. With this the overall correlation lengths are able to be calculated for the piston ring-pack interface. Figure 3.11 shows the auto-correlation function for the cylinder wall, while Figure 3.12 shows the piston ring, and Figure 3.13 shows the convoluted surfaces.

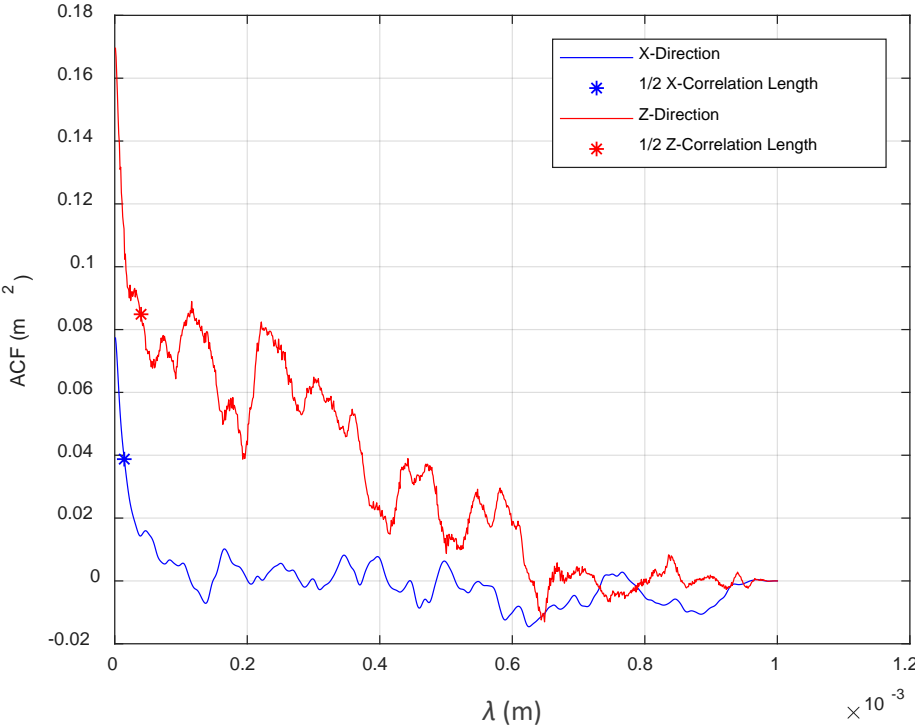


Figure 3.11: Auto-Correlation Function for the cylinder wall

As seen in Figure 3.11, the ACF gradually decays showing that as the correlation length increases, the asperities have less correlation and effect on each other.

The asperities in the  $x$  direction have little correlation with each other, as seen in Figure 3.11. This is graphically seen as the function reaches a minimum at a faster rate as compared to the  $z$  direction. The  $z$  direction is seen to take a longer time to decay. This is in agreement with the surface engineered topography. The cross-hatching pattern (Figure 3.3) is seen to have more of an effect on the local asperities in the  $z$  direction. This aids in the transport of fluid as asperities work in unison in this direction. This improves lubrication flow along the wall through the combustion cycle as the piston moves from Bottom Dead Center to Top Dead Center, and vice versa.

In Figure 3.12 are the  $x$  and  $z$  direction correlation functions for the piston ring. It is noticed that unlike the cylinder wall, there is not a strong correlation in one direction or the other. This is seen graphically as both the  $x$  and  $z$  correlation curves decay rather abruptly; this results in very little aid in the transportation of lubricant from local asperities.

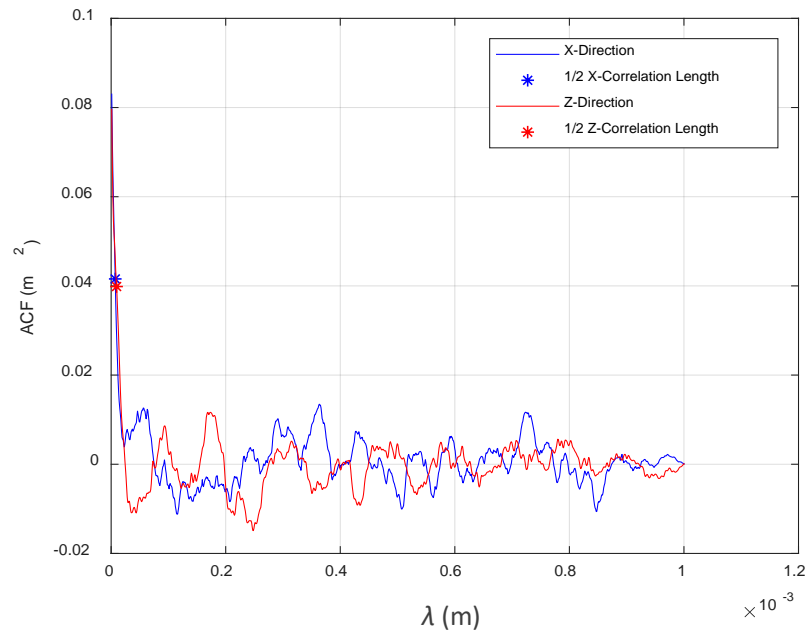


Figure 3.12: Auto-Correlation Function for the piston ring

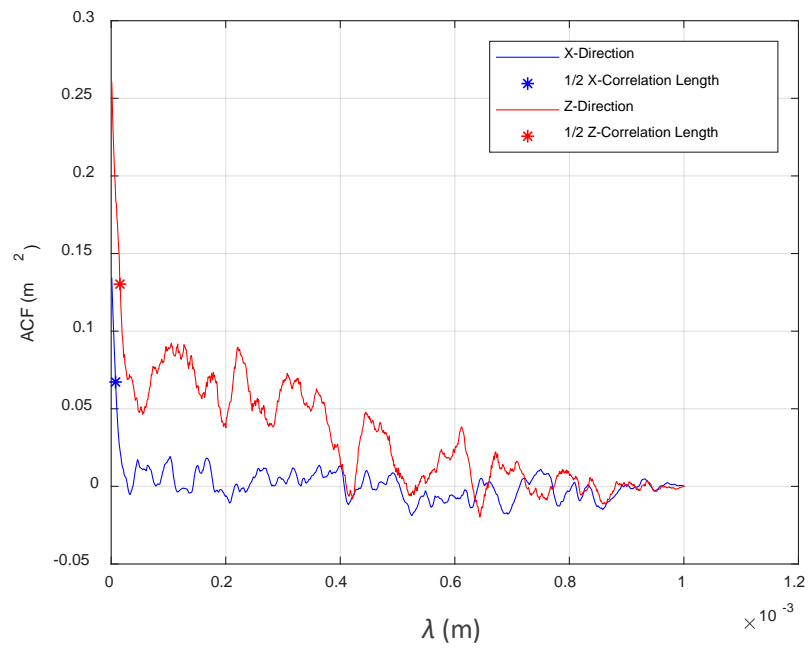


Figure 3.13: Auto-Correlation Function for convoluted surfaces

The correlation lengths for the convoluted surfaces are seen in Figure 3.13. The  $x$  direction correlation length decays rather quickly in a similar fashion to both the cylinder wall and piston ring. The  $z$  direction correlation curve, however, is observed to be higher than the piston ring, but lower than the cylinder wall. This is where the curve should be observed due to the fact one surface is engineered for lubricant flow and one surface is not. It is still noticed by the  $z$  direction correlation curve for the convoluted surface that asperities farther away are more correlated.

### *3.2.2 Cross-Correlation Function*

New developments have led to a more accurate model of the auto-correlation function by expanding its surface characterization capabilities [2]. Instead of correlating multiple 2-D ACF's together over a 3-D surface, Peklenik suggested a 3-D cross-correlation function (CCF) instead of the auto-correlation function. Instead of correlating each row of asperities in a rectilinear fashion then averaging the correlations over the entire surface, it was suggested to move in a diagonal pattern across the surface. Figure 3.14 shows the movement of the cross correlation function.

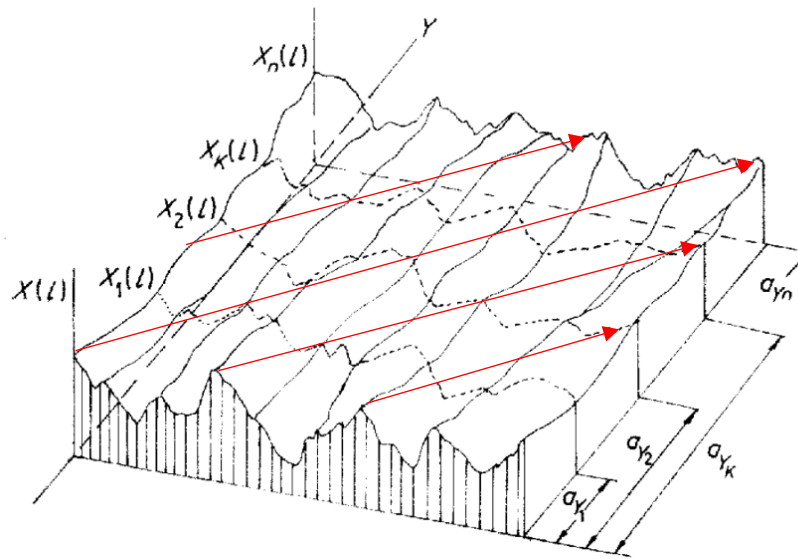


Figure 3.14: Cross-Correlation Function direction [2]

For three dimensional surface characterizations the auto-correlation function is able to be written in its primary tensor notation as the cross-correlation function

$$\rho_{ij}(\lambda) = \frac{1}{N - \lambda} \sum_{i=1}^{N-\lambda} X_{ii}(l) X_{ij}(l + \lambda) \quad (12)$$

The primary difference from the ACF and CCF is that multiple signals are now related to each other. This application is largely more accurate when analyzing the full intricacies of three dimensional surface characterizations of a real measured tribological surface. The assumption of a linear auto-correlation function for small decay lengths,  $\lambda$ , may be held true for most engineering surfaces under two dimensions [1], however this assumption is not held when expanded to three dimensions, especially for the accurate analysis of the piston ring interface. Figure 3.15 shows the cross-correlation function for the convoluted surfaces.

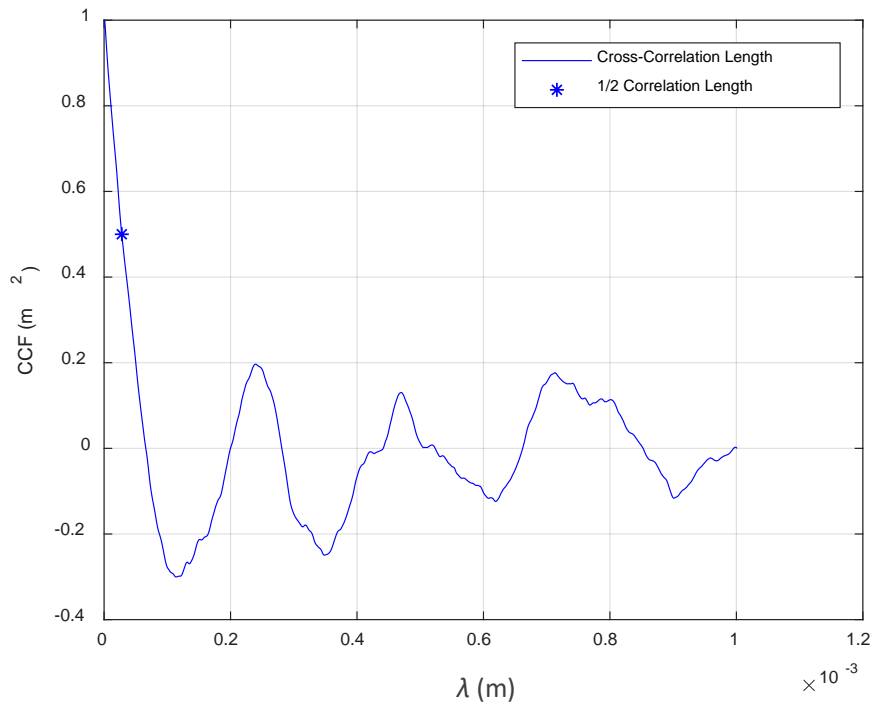


Figure 3.15: Cross-Correlation Function for convoluted surfaces

The cross-correlation function is seen to have several differences from the auto-correlation function. Firstly is the amount of noise that is seen. The function is seen to have a very consistent and stable decay rate with little interferences. This is due to the amount of averages across each diagonal of the surfaces. Where the ACF averages each correlation length together to get one length, the CCF continually updates the average as more correlation signals are measured. Secondly, strong correlations exist at relatively evenly spaced distances, denoted by the curve peaks. This is due to the repetitive cross-hatching structure on the cylinder wall surface.

For the evaluation of the directional surface patterns in the current study the cross-correlation function must be normalized [2]. For deterministic characteristics and surfaces measured in identical parallel directional patterns (i.e. on a profilometer), the following condition must be satisfied

$$\rho_{ij}(\lambda)_{max} = \rho_{ii}(0) = \rho_{jj}(0) = 1 \quad (13)$$

where the correlation function is normalized by its maximum value such that the value is unity. Likewise the correlation length is normalized by the root-mean-square roughness. With the correlation lengths calculated, deterministic methods can now be employed to classify the flow of lubricant past asperities among the surface interactions.

### 3.2.3 Surface Anisotropy Index

In order to study the specific effects of flow factors on directional surface topography we use the Peklenik [2, 63] number,  $\gamma$ , also known as the surface anisotropy index. The Peklenik number is defined as the ratio of correlation lengths in the  $x$  and  $z$  direction:

$$\gamma = \frac{\lambda_{0.5z}}{\lambda_{0.5x}} \quad (14)$$

The Peklenik number can be visualized from Patir and Cheng [1] as the individual asperity length-to-width ratio shown in Figure 3.16.

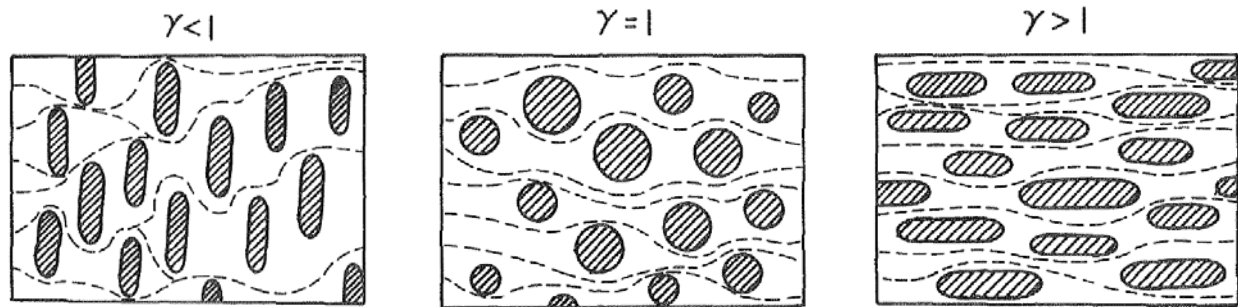


Figure 3.16: Typical surface characterization for transversely ( $\gamma < 1$ ) oriented, isotropic ( $\gamma = 1$ ), and longitudinally oriented ( $\gamma > 1$ ) surfaces [1]

As previously mentioned, the transversely oriented asperities hinder the flow of lubricant while longitudinally oriented asperities aid in the movement of lubricant. This is synonymous with the design of the engineered cylinder wall surface where lubricant is channeled through the grooves to aid in the lubrication of the piston ring-pack.

While the surface anisotropy index number has previously been calculated for the interactions of one rough surface and one smooth surface, its use is currently expanded to two rough surfaces through the principal of superposition as accomplished with the convoluted surfaces used for the ACF and CCF calculations. For completeness, the studied surface interactions are able to be compared to Patir and Cheng [1, 40] through the Peklenik number. Table 3.1 lists the calculated parameters from the combined surface data.

Table 3.1: Surface data parameters

Parameter	Value	Units
Correlation length in $x$ direction ( $\lambda_{0.5x}$ )	5.492	$\mu\text{m}$
Correlation length in $z$ direction ( $\lambda_{0.5z}$ )	14.493	$\mu\text{m}$
RMS roughness of cylinder wall ( $\sigma_1$ )	0.892	$\mu\text{m}$
RMS roughness of piston ring ( $\sigma_2$ )	0.294	$\mu\text{m}$
Composite RMS roughness ( $\sigma$ )	0.939	$\mu\text{m}$

Table 3.2 lists the Peklenik numbers for the various surfaces, with each respective method used to calculate it.

Table 3.2: Surface anisotropy index values

Parameter	Method	Peklenik Number
Cylinder wall	ACF	3.45
Piston ring	ACF	1.32
Convolutated surfaces	ACF	2.64
Convolutated surfaces	CCF	2.79

Considering the cylinder wall and piston ring interface, their combined Peklenik number,  $\gamma$ , is calculated to be 2.79. This agrees with previous works as the surface topography on the cylinder wall aides in the conveyance of fluid and therefore results in a surface anisotropy number

greater than unity ( $\gamma > 1$ ). The piston ring also results in a value greater than unity indicating it also aids in the flow of lubrication. This agrees with Figure 3.8 as the pores in the surface are meant to house lubricant. This results in lubricant flowing over the lubricant filled pores and results in a lower coefficient of friction; as opposed to the lubricant sliding across the asperities themselves which would raise the coefficient of friction.

With a study of the surface roughness directionality characterizations and surface topography completed, a study is now shifted over to analyze the flow of lubricant under these various conditions.

### *3.3 The Reynolds Equation*

The Reynolds equation is solved to calculate the fluid film pressure distribution of thin viscous fluid films. The equation is used to estimate the hydrodynamic, squeeze, and hydrostatic pressure variations across any type of fluid film bearing. The Reynolds equation is derived from the Navier-Stokes equations under the following conditions

1. Incompressible flow
2. Thin film
  - i. Laminar flow
  - ii. Neglected convective accelerations
  - iii. Neglected body forces and inertia
3. Steady-State
4. Newtonian fluid

## 5. No slip at solid boundaries

### 3.3.1 Derivation from Navier-Stokes

The Navier-Stoke equations are a set of three nonlinear scalar differential equations that come from the conservation of momentum equation and the constitutive relations for a Newtonian fluid. In their primary tensor notation, with three possible values of the free subscript  $j$ , can be expressed by Eq. (15)

$$\rho \frac{\partial u_j}{\partial t} + \rho u_k \frac{\partial u_j}{\partial x_k} = -\frac{\partial p}{\partial x_j} + \frac{\partial}{\partial x_j} \left( \lambda \frac{\partial u_k}{\partial x_k} \right) + \frac{\partial}{\partial x} \left[ \mu \left( \frac{\partial u_i}{\partial x_j} + \frac{\partial u_j}{\partial x_i} \right) \right] + \rho f_j \quad (15)$$

Under the assumption of an incompressible fluid the continuity equation is equivalent to zero. This is expressed in tensor notation in Eq. (16)

$$\frac{\partial u_k}{\partial x_k} = \frac{\partial u}{\partial x} + \frac{\partial v}{\partial y} + \frac{\partial w}{\partial z} \quad (16)$$

Also under the assumption of steady state the temporal acceleration, expressed as the first term of Eq. (15), becomes zero. Expressed as Eq. (17)

$$\rho \frac{\partial u_j}{\partial t} = \frac{\partial u}{\partial t} + \frac{\partial v}{\partial t} + \frac{\partial w}{\partial t} = 0 \quad (17)$$

Likewise neglecting convective accelerations, such as when flow moves around an obstruction, the second term on the left hand side of Eq. (15) becomes zero. Expressed as Eq. (18)

$$\rho u_k \frac{\partial u_j}{\partial x_k} = 0 \quad (18)$$

Under the assumption of a thin film, body forces, such as gravity, which act on the mass of the fluid, are neglected. Therefore the last term on the right hand side of Eq. (15) reduces to zero and is expressed by Eq. (19)

$$\rho f_j = 0 \quad (19)$$

Thusly the Navier-Stokes Equations (15) reduce to Eq. (20), as expressed in primary tensor notation.

$$0 = -\frac{\partial p}{\partial x_j} + \frac{\partial}{\partial x_i} \left[ \mu \left( \frac{\partial u_i}{\partial x_j} + \frac{\partial u_j}{\partial x_i} \right) \right] \quad (20)$$

where the first term on the right hand side represents the pressure gradient across the fluid film and the second term on the right hand side represents the viscous-shear term. Under the assumption of a very thin film, the pressure gradient across the width of the film does not change. Also under this same assumption of a thin film, the velocity of the film changes quickly. This can be expressed by Eq. (21)

$$\frac{\partial^2 u}{\partial y^2} \gg \frac{\partial^2 u}{\partial x^2} \text{ and } \frac{\partial^2 u}{\partial z^2} \quad (21)$$

Under these assumptions Eq. (20) reduces to two directions. The  $x$  direction and  $z$  direction flow equations respectively become

$$0 = -\frac{\partial p}{\partial x} + \mu \frac{\partial^2 u}{\partial y^2} \quad (22)$$

$$0 = -\frac{\partial p}{\partial z} + \mu \frac{\partial^2 v}{\partial y^2} \quad (23)$$

Both of which are dependent on the  $y$  direction velocity gradient as stated in Eq. (21). By integrating Eqs. (22) and (23) to get  $u$  and  $v$ , respectively, the  $x$  and  $z$  direction velocity profiles are

$$u = \frac{1}{2\mu} \frac{\partial p}{\partial x} (y^2 - hy) + \frac{2\bar{U}y}{h} \quad (24)$$

$$v = \frac{1}{2\mu} \frac{\partial p}{\partial z} (y^2 - hy) \quad (25)$$

Assume an arbitrary control volume as shown in Figure 3.17.

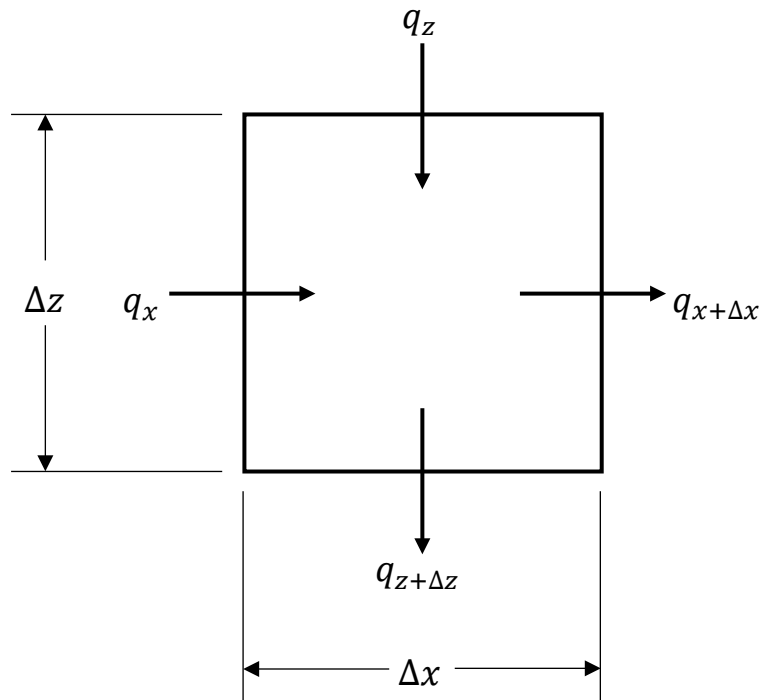


Figure 3.17: Control volume

As the flow rate increases, the control volume decreases in volume. Vice versa holds true; as the flow rate decreases the control volume increases in volume.

The local flow per unit width can be expressed in terms of the changing film thickness

$$\frac{\partial h}{\partial t} = \frac{q_x - q_{x+\Delta x}}{\Delta x} + \frac{q_z - q_{z+\Delta z}}{\Delta z} \quad (26)$$

As  $\Delta x$  and  $\Delta z$  become infinitesimally small and approach zero, under the assumption the base area still contains a sufficient number of asperities to perform the integration, Eq. (26) becomes:

$$\frac{\partial h}{\partial t} = -\frac{\partial q_x}{\partial x} - \frac{\partial q_z}{\partial z} \quad (27)$$

Thusly, the local flow rates per unit width are calculated from the integration of Eqs. (24) and (25).

The integrals may be expressed as

$$q_x = \int_0^h u dy \quad (28)$$

$$q_z = \int_0^h v dy \quad (29)$$

And are calculated to be

$$q_x = -\frac{h^3}{12\mu} \frac{\partial p}{\partial x} + \bar{U} h \quad (30)$$

$$q_z = -\frac{h^3}{12\mu} \frac{\partial p}{\partial z} \quad (31)$$

Now the reduced Navier-Stokes equation (Eq. (20)) is able to be expressed in terms of the pressure gradient and changing film thickness. Using Eqs. (30) and (31) to modify Eq. (20), the Reynolds equation is obtained,

$$\frac{\partial}{\partial x} \left( \frac{h^3}{12\mu} \frac{\partial p}{\partial x} \right) + \frac{\partial}{\partial z} \left( \frac{h^3}{12\mu} \frac{\partial p}{\partial z} \right) = \frac{\bar{U}}{2} \frac{\partial h}{\partial x} + \frac{\partial h}{\partial t} \quad (32)$$

This equation is also commonly rearranged as

$$\frac{\partial}{\partial x} \left( h^3 \frac{\partial p}{\partial x} \right) + \frac{\partial}{\partial z} \left( h^3 \frac{\partial p}{\partial z} \right) = 6\mu\bar{U} \frac{\partial h}{\partial x} + \frac{\partial h}{\partial t} \quad (33)$$

The two terms on the left hand side of the Reynolds equation (Eq. (32)), represent the pressure driven flow, or Poiseuille flow. Poiseuille flow is the viscous flow due to a pressure gradient in the direction of the fluid motion, as seen in Figure 3.18. The first term on the right hand side represents the shear-driven flow, or Couette flow. Couette flow is the viscous flow due to a velocity gradient perpendicular to the direction of motion of the fluid, as seen in Figure 3.19. Lastly, the second term on the right hand side represents how the film thickness changes with time, also called the squeeze film term. This term is neglected under steady state and therefore is beyond the scope of this thesis.

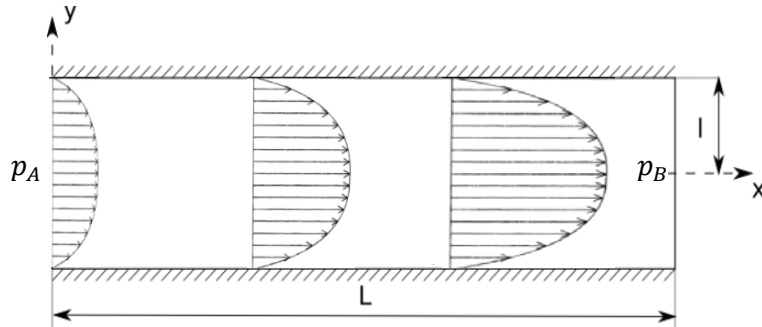


Figure 3.18: Poiseuille flow

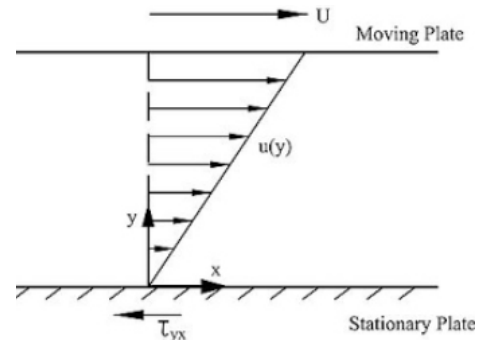


Figure 3.19: Couette flow

Therefore under the above assumptions, the Navier-Stokes equations are simplified to the Reynolds equation (Eq. (32)).

### 3.3.2 Discretization

The Reynolds equation is numerically solved for using the centered finite difference method. There are several forms in which the equation solution can be expressed. Firstly, the method of breaking the equation down into multiple parts through the use of coefficients to enhance computational efficiency [64], and secondly is keeping the solution as one equation. These two forms of the solution are outlined below.

#### 3.3.2.1 Coefficients for Reynolds Equation Discretization

The Reynolds equation is solved for the pressure flows using the centered finite difference method by setting up a nodal network shown in Figure 3.20.

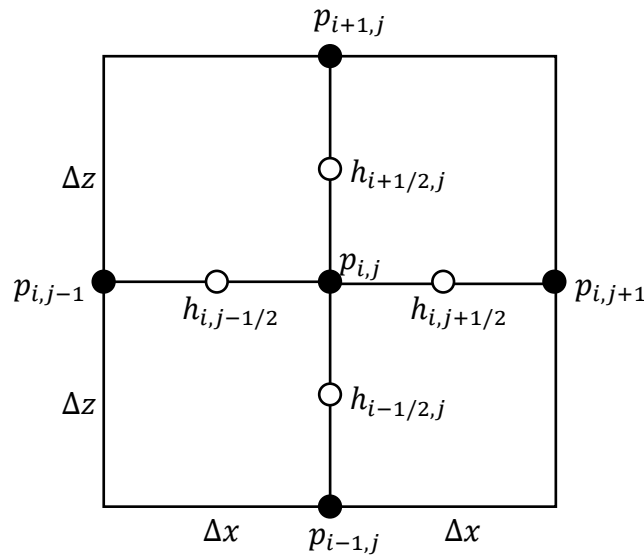


Figure 3.20: Discretization of Pressure ( $p$ ) and Film Thickness ( $h$ )

The intermediate pressures at the midpoints are calculated through Eqs (34-37)

$$\left(\frac{\partial p}{\partial x}\right)_{i,j+1/2} = \frac{p_{i,j+1} - p_{i,j}}{\Delta x_{j+1}} \quad (34)$$

$$\left(\frac{\partial p}{\partial x}\right)_{i,j-1/2} = \frac{p_{i,j} - p_{i,j-1}}{\Delta x_j} \quad (35)$$

$$\left(\frac{\partial p}{\partial z}\right)_{i+1/2,j} = \frac{p_{i+1,j} - p_{i,j}}{\Delta z_{i+1}} \quad (36)$$

$$\left(\frac{\partial p}{\partial z}\right)_{i-1/2,j} = \frac{p_{i,j} - p_{i-1,j}}{\Delta z_i} \quad (37)$$

In using the normalized Reynolds equation (Eq. (33)), in conjunction with using the central difference for calculating the expressions at the primary node  $(i, j)$ , the Poiseuille terms in the  $x$  and  $z$  directions become Eqs. (38) and (39), respectively

$$\left(\frac{\partial}{\partial x}\left(h^3 \frac{\partial p}{\partial x}\right)\right)_{i,j} = \frac{h_{i,j+1/2}^3 \left(\frac{\partial p}{\partial x}\right)_{i,j+1/2} - h_{i,j-1/2}^3 \left(\frac{\partial p}{\partial x}\right)_{i,j-1/2}}{\frac{\Delta x_j + \Delta x_{j+1}}{2}} \quad (38)$$

$$\left(\frac{\partial}{\partial x}\left(h^3 \frac{\partial p}{\partial z}\right)\right)_{i,j} = \frac{h_{i+1/2,j}^3 \left(\frac{\partial p}{\partial z}\right)_{i+1/2,j} - h_{i-1/2,j}^3 \left(\frac{\partial p}{\partial z}\right)_{i-1/2,j}}{\frac{\Delta z_i + \Delta z_{i+1}}{2}} \quad (39)$$

The partial derivatives on the right hand side of Eqs. (38) and (39) are exactly equivalent to the intermediate pressures discretized in Eqs. (34-37). In a similar manner the Couette flow term becomes

$$\left(\frac{\partial h}{\partial x}\right)_{i,j} = \frac{h_{i,j+1/2} - h_{i,j-1/2}}{\frac{\Delta x_j + \Delta x_{j+1}}{2}} \quad (40)$$

Substituting the above discretized expressions into the normalized Reynolds equation (Eq. (33)) and solving for  $p_{i,j}$  leads to the overall pressure equation

$$p_{i,j} = \frac{1}{a_5} (a_1 p_{i,j-1} + a_2 p_{i,j+1} + a_3 p_{i-1,j} + a_4 p_{i+1,j} + a_0) \quad (41)$$

where the coefficients are expressed in Eq. (42)

$$\begin{aligned} a_0 &= \frac{h_{i,j+1/2} - h_{i,j-1/2}}{\Delta x_j + \Delta x_{j+1}} & a_1 &= \frac{h_{i,j-1/2}^3}{\Delta x_j (\Delta x_j + \Delta x_{j+1})} \\ a_2 &= \frac{h_{i,j+1/2}^3}{\Delta x_{j+1} (\Delta x_j + \Delta x_{j+1})} & a_3 &= \frac{h_{i-1/2,j}^3}{\Delta z_i (\Delta z_i + \Delta z_{i+1})} \\ a_4 &= \frac{h_{i+1/2,j}^3}{\Delta z_{i+1} (\Delta z_i + \Delta z_{i+1})} & a_5 &= a_1 + a_2 + a_3 + a_4 \end{aligned} \quad (42)$$

Thusly the pressure at the node of interest is able to be calculated through the summation of its counterparts.

### 3.3.2.2 Complete Discretized Equation

The second numerical solution form for the Reynolds equation is using the complete discretized equation. This method comes from substituting in Eq. (42) into Eq. (41) and calculating the nodal pressure ( $p_{i,j}$ ) by one equation. It is computationally more efficient for the Couette flow case as the majority of the coefficients in Eq. (42) are dependent on the Poiseuille flow case.

Substituting Eqs. (38-40) into the Reynolds equation (Eq. (33)) gives the following

$$\begin{aligned}
& \frac{h_{i,j+1/2}^3 \left( \frac{\partial p}{\partial x} \right)_{i,j+1/2} - h_{i,j-1/2}^3 \left( \frac{\partial p}{\partial x} \right)_{i,j-1/2}}{\frac{\Delta x_j + \Delta x_{j+1}}{2}} \\
& + \frac{h_{i+1/2,j}^3 \left( \frac{\partial p}{\partial z} \right)_{i+1/2,j} - h_{i-1/2,j}^3 \left( \frac{\partial p}{\partial z} \right)_{i-1/2,j}}{\frac{\Delta z_i + \Delta z_{i+1}}{2}} \quad (43) \\
& = 6\mu\bar{U} \frac{h_{i,j+1/2} - h_{i,j-1/2}}{\frac{\Delta x_j + \Delta x_{j+1}}{2}}
\end{aligned}$$

Substituting in Eqs. (34-37) and solving for  $p_{i,j}$  gives the complete discretized equation

$$\begin{aligned}
& \frac{6\mu\bar{U}\Delta x(\Delta z)^2 \left( \frac{h_{i,j+1} - h_{i,j-1}}{2} \right) - (h_{i,j-1/2}^3)(p_{i,j-1})(\Delta z)^2 - (h_{i,j+1/2}^3)(p_{i,j+1})(\Delta z)^2}{(\Delta z)^2(h_{i,j-1/2}^3 - h_{i,j+1/2}^3) + (\Delta x)^2(h_{i-1/2,j}^3 - h_{i+1/2,j}^3)} \dots \\
& - \frac{(h_{i-1/2,j}^3)(p_{i-1,j})(\Delta x)^2 + (h_{i+1/2,j}^3)(p_{i+1,j})(\Delta x)^2}{(\Delta z)^2(h_{i,j-1/2}^3 - h_{i,j+1/2}^3) + (\Delta x)^2(h_{i-1/2,j}^3 - h_{i+1/2,j}^3)} = p_{i,j} \quad (44)
\end{aligned}$$

Thusly the pressure at the node of interest is able to be calculated at a greater computational efficiency for the Couette flow case.

### 3.3.3 Verification

The Reynolds equation is initially solved for the case of a slider bearing, operating only in the hydrodynamic regime. A slider bearing utilizes a converging diverging wedge shape geometry to generate load support. The entrance is at a larger film thickness than the exit as shown in Figure 3.21.

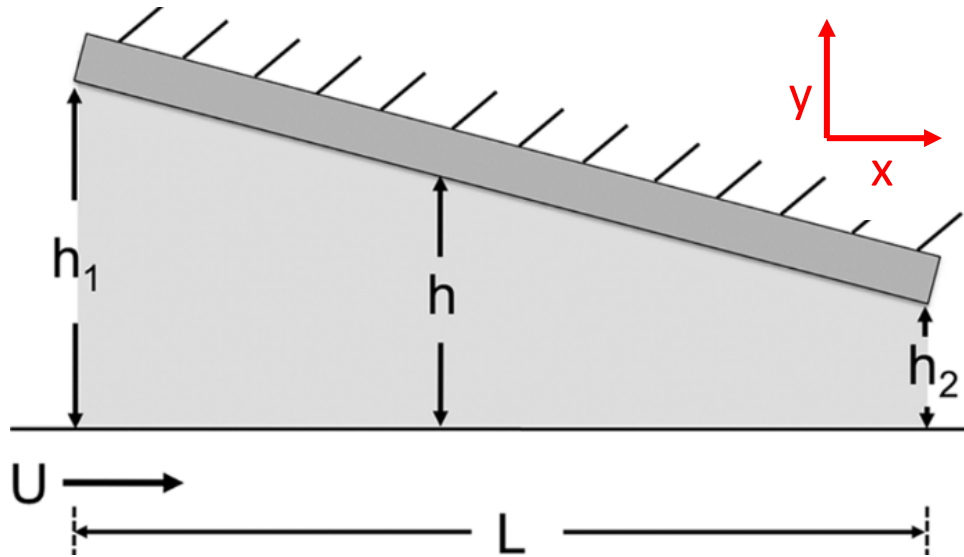


Figure 3.21: Fixed incline slider bearing geometry

For the verification of the discretized and programmed Reynolds equation, 1-D geometry is used. Flow is only considered in the  $x$  direction. Thusly The Reynolds equation (Eq. (32)) reduces to its simplified 1-D form;

$$\frac{\partial}{\partial x} \left( \frac{h^3}{12\mu} \frac{\partial p}{\partial x} \right) = 2\bar{U} \frac{\partial h}{\partial x} \quad (45)$$

To numerically solve this equation, the nodal network set up on the slider bearing is shown in Fig 3.22.

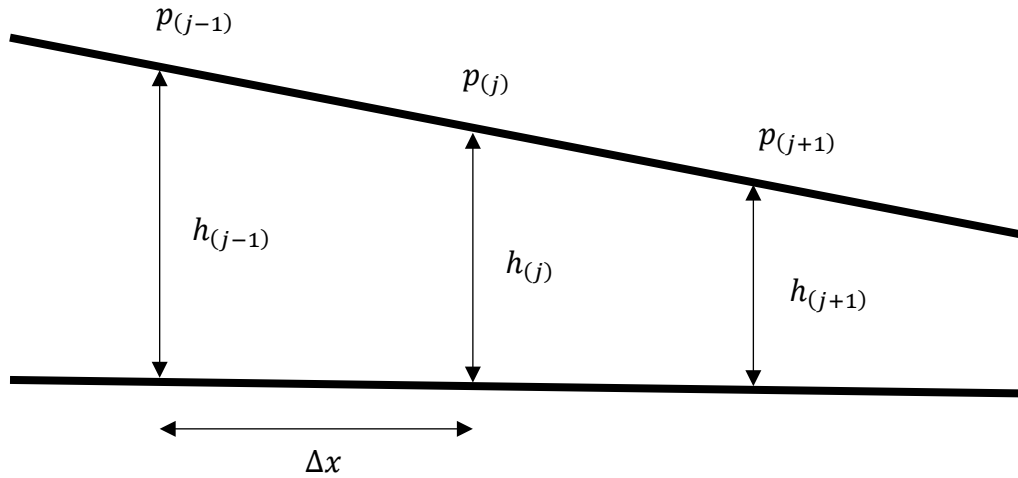


Figure 3.22: Nodal discretization for slider bearing

As lubricant travels from the entrance of the bearing ( $h_1$ ) to the exit ( $h_2$ ), the pressure increases while the velocity of the lubricant decreases in accordance with Bernoulli's principle. This relative fluid film motion generates hydrodynamic pressure in the lubricant which is able to carry a load on the upper surface of the bearing. By solving the Reynolds equation, with the slider bearing geometry in 1-D, the hydrodynamic pressure in the bearing can be calculated as mentioned in Section 3.3.2. The load carrying capacity of the bearing can then be numerically calculated by integrating the pressure per unit area. This can be done with Simpsons rule, expressed as follows

$$\frac{Force}{Width} = \int_{x_{j-1}}^{x_{j+1}} p dx = \frac{2\Delta x}{6} [p_{(x_{j-1})} + 4p_{(j)} + p_{(x_{j+1})}] \quad (46)$$

It should be mentioned that in calculating the load carrying capacity, every other node is used because Simpsons rule integrates over a block defined by three adjacent nodes.

With the geometry initialized the boundary conditions are now initialized. The pressure at the first and last node are assumed to be atmospheric and no hydrodynamic pressure is calculated at those nodes. They still serve as part of the nodal grid to calculate the pressure at all interior nodes. The pressure at each node may now be calculated numerically based on the discretized film thickness. The parameters for this system are outlined in Table 3.3.

Table 3.3: System parameters

Parameter	Variable	Value	Units
Dynamic viscosity	$\mu$	0.1	$Pa \cdot s$
Relative velocity	$u$	1	$m/s$
Length of bearing	$L$	0.01	$m$
Height at inlet of incline	$h_1$	3	$\mu m$
Height at outlet of incline	$h_2$	1	$\mu m$

The analytical pressure solution to the 1-D Reynolds equation (Eq. (45)) has been solved analytically under the infinitely long approximation [65] and is

$$P = 6\mu U \frac{L}{h_1^2 - h_2^2} \frac{(h_1 - h)(h - h_2)}{h^2} \quad (47)$$

where the film thickness ( $h$ ) along the bearing is

$$h_{(x)} = -\frac{(h_1 - h_2)}{L}x + h_1 \quad (48)$$

The load-carrying capacity has also been analytically solved for the infinitely long approximation [65] and is

$$w = \frac{6\mu UL^2}{(\lambda - 1)^2 h_2^2} \left[ \ln\lambda - \frac{2(\lambda - 1)}{\lambda + 1} \right] \quad (49)$$

where the film thickness ratio ( $\lambda$ ) is defined as

$$\lambda = \frac{h_1}{h_2} \quad (50)$$

The numerical 1-D Reynolds equation solution can now be validated from the analytical solution for both hydrodynamic pressure and load-carrying capacity.

The film thickness is shown in Figure 3.23. It can be seen that the inlet and outlet heights are the same as in Table 3.3 along the length of the bearing. The hydrodynamic pressure is shown in Figure 3.24. As previously stated the boundary nodes are set to zero, as can be seen.

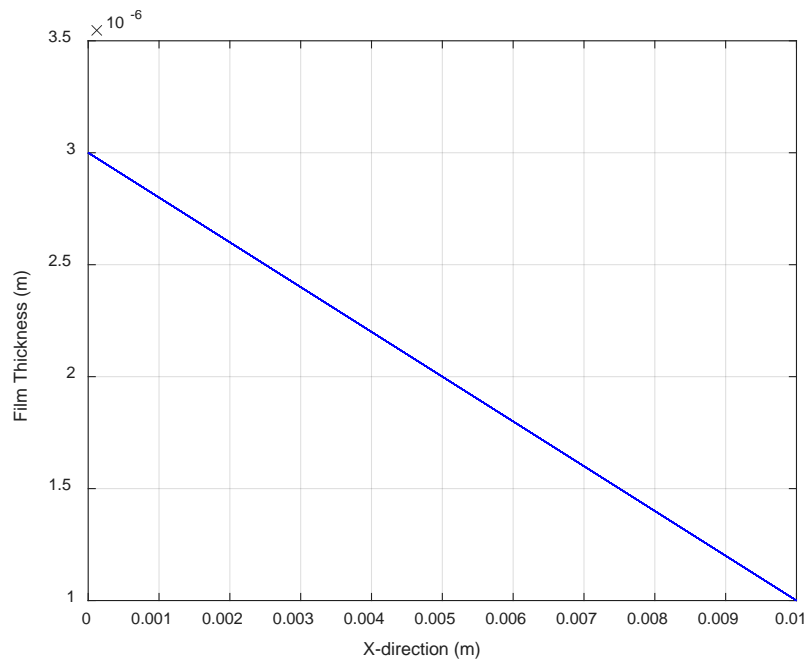


Figure 3.23: Film thickness of 1-D slider bearing

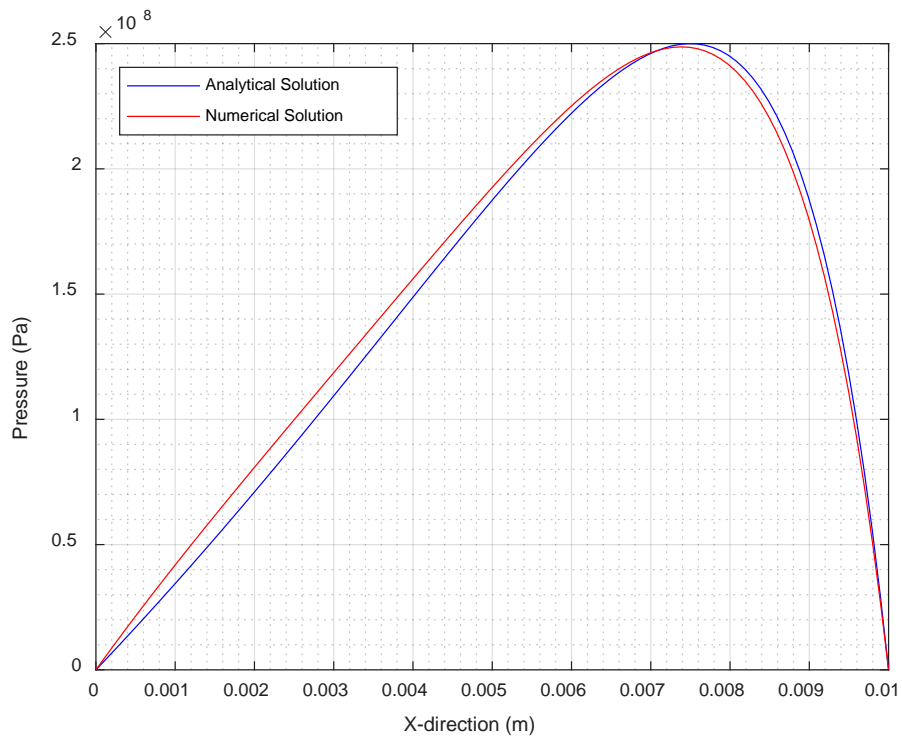


Figure 3.24: Pressure distribution along 1-D slider bearing

With a maximum error between the numerical and analytical pressure solutions of 2.3%, the numerical solution is verified by the minimal deviations from the analytical solution.

Upon integration of pressure the load carrying capacity per unit width is numerically calculated and plotted in Figure 3.25 as a function of the inlet to outlet ratio, along with the analytical solution for verification.

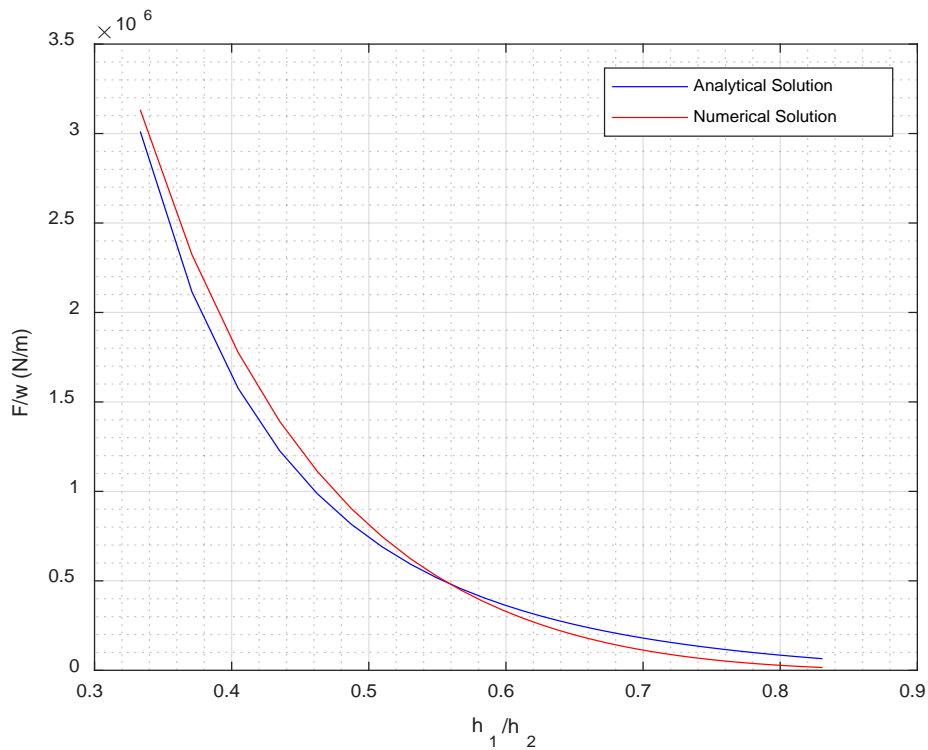


Figure 3.25: Force per unit width of the slider bearing

It is observed that as the inlet and outlet approach the same film thickness, the load carrying capacity decreases. This is due to much less hydrodynamic pressure generation in the fluid as the geometry converges in the gap. Similar to the hydrodynamic pressure verification, with a maximum error between the numerical and analytical solutions of 3.0%, the numerical solution is verified by the minimal deviations from the analytical solution.

Upon successful verification of the 1-D fixed incline slider bearing model, the model can now be expanded to 2-D by using the derived Reynolds equation (Eq. (32)). In this manner the general procedure stays identically the same:

1. Initialize geometry
2. Initialize boundary conditions
3. Discretize film thickness
4. Calculate nodal pressure from Reynolds equation (Eq. (32))

The 2-D Reynolds equation does not have a closed form analytical solution and can only be solved numerically. However with the verification of the 1-D case system model, and employing the same numerical discretization techniques for the  $z$  direction, the 2-D model is assumed to be accurate.

The boundary conditions are still assigned to zero for the verification stage of the 2-D Reynolds solution. The primary difference in this case is the slider bearing now has depth. The slider bearing is modeled as having the same width and length (0.01m) set up by a 50x50 nodal grid, as can be seen from the film thickness in Figure 3.26. With all the same system parameters as mentioned in Table 3.3, the pressure of the bearing is shown in Figure 3.27.

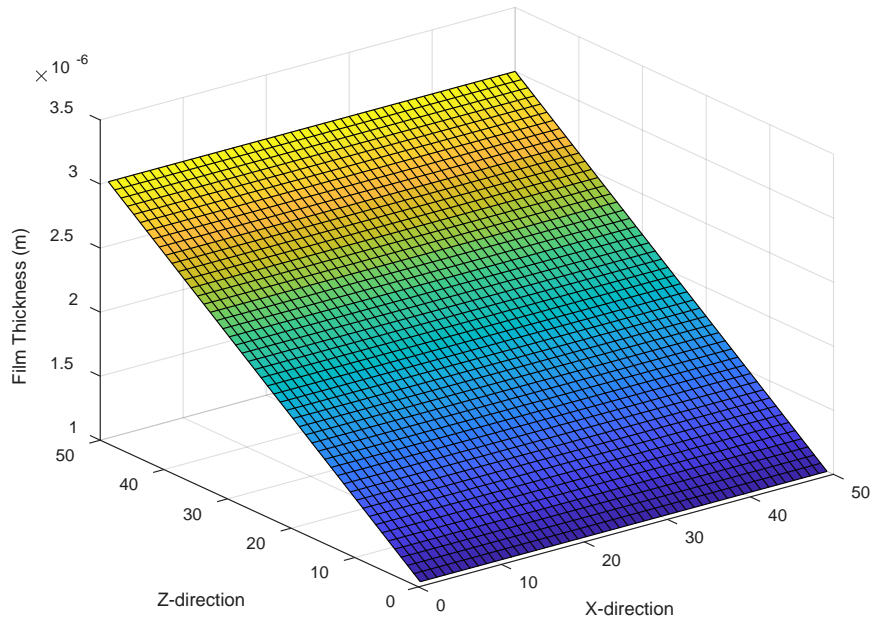


Figure 3.26: Film thickness of 2-D slider bearing

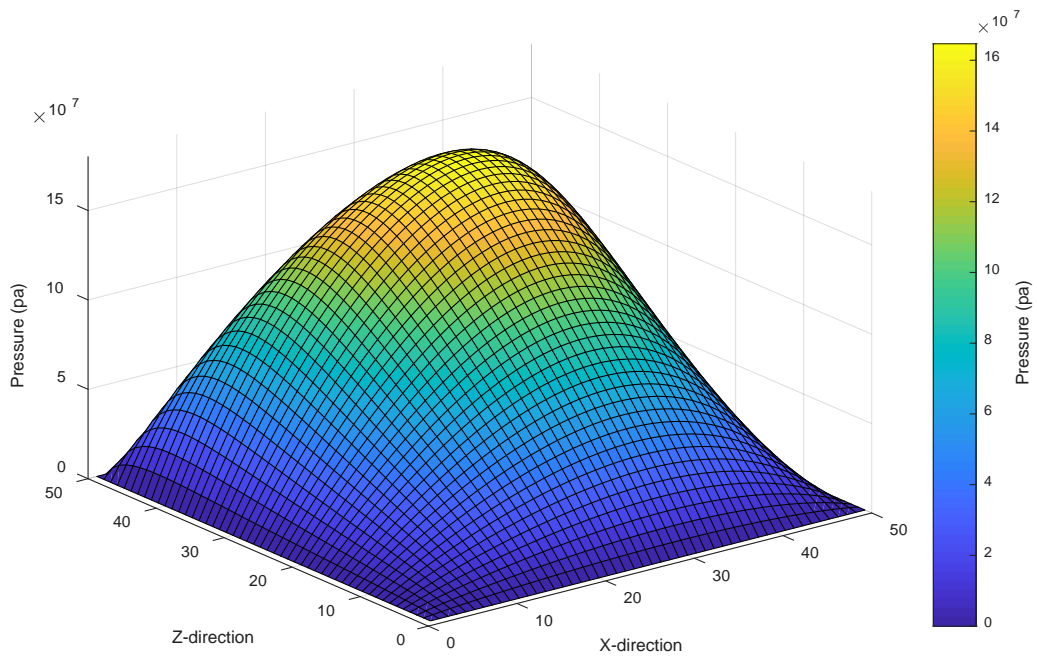


Figure 3.27: Pressure distribution along 2-D slider bearing

The Reynolds equation is seen to predict the hydrodynamic pressure in a fluid film bearing under several cases. With the system and programmatic set-up concluded for these slider bearing verification cases, the accuracy of the solutions must now be analyzed.

### 3.3.4 Convergence and Relaxation

In solving the Reynolds equation for pressure an iterative method is used. Starting with an initial guess the pressure is calculated and iterated approaching a converged solution. The solution has converged based on a convergence criteria, or percent error, between the current solution and the previous solution. The pressure at every node is calculated, along with the average error for the entire surface. The average error for the entire surface expressed mathematically is

$$Error = \left( \sum_{j=1}^N \sum_{i=1}^M \frac{(p_{i,j})_K - (p_{i,j})_{K-1}}{(p_{i,j})_{K-1}} \right) \left( \frac{1}{NM} \right) \quad (51)$$

where  $K$  represents the iteration number. Figure 3.28 shows a plot of the calculated pressure, for the 1-D case, every tenth iteration until convergence is reached. The initial pressure guess is zero at every node.

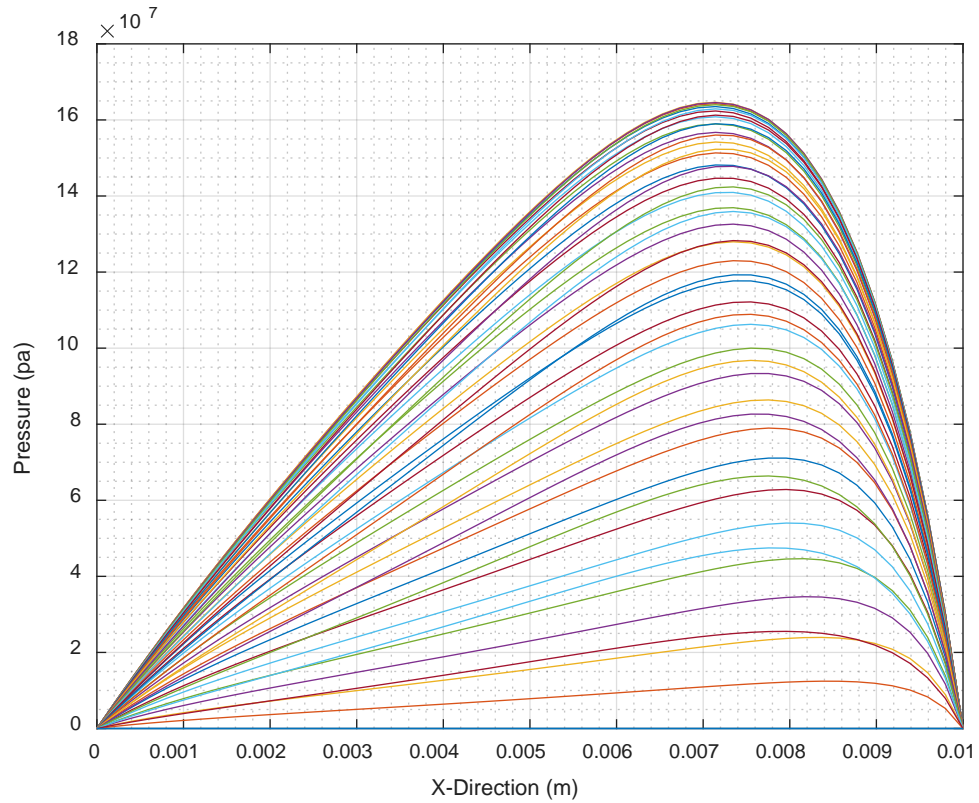


Figure 3.28: Pressure convergence of modeled slider bearing

It can be seen that the initial guess was zero and the curves are trending towards a solution. The closer the two curves are to one another the smaller the error between them. Once the convergence criteria is reached the solution has been reached. As shown from Figure 3.28, the curves move closer together as the pressure increases, indicating the calculated pressure is getting closer to the solution.

While the Reynolds equation is a stable, second order, linear differential equation, relaxation methods can be used to either accelerate or decelerate the convergence process. At each iteration the pressure is calculated and the results can be relaxed through

$$(p_{i,j})_K = (p_{i,j})_K W + (p_{i,j})_{K-1} (1 - W) \quad (52)$$

where  $W$  is called the relaxation factor. For most cases where relaxation is implemented the relaxation factor is close to 1. It represents an assigned weight value to the new solution and the previous solution. For a relaxation factor of 0.9, that is  $W = 0.9$ , then the first term on the right hand side of Eq. (52) tells the calculated nodal pressure to be weighted as 90% of the new solution. While, the second term on the right hand side tells the calculated pressure to be weighted by  $(1 - W)$ , that is 0.1, or 10% of the pressure calculated from the previous iteration.

When  $W = 1$  no relaxation takes place and the nodal pressure is calculated and the solution converges at its standard rate. By assigning a value of  $W > 1$  more weight is given on the new solution while reducing the weight of the previous solution. This scheme is called successive over-relaxation (SOR) and results in an accelerated convergence; typically used for very stable differential equations. As opposed to when  $W < 1$  the weight scheme is reversed and less weight is given to the new solution and more weight is given to the previous solution. This scheme is called successive under-relaxation (SUR) and results in a decelerated convergence; typically used for differential equations that have stability issues.

In terms of the Reynolds equation, a relaxation factor between 1.1 and 1.2 is observed to be very stable. With too large of a relaxation factor employed, the solution runs the risk of diverging and not approaching a converged solution. Figure 3.29 shows the convergence error for

various values of relaxation factor from the same modeled bearing problem outline in Section 3.3.3.

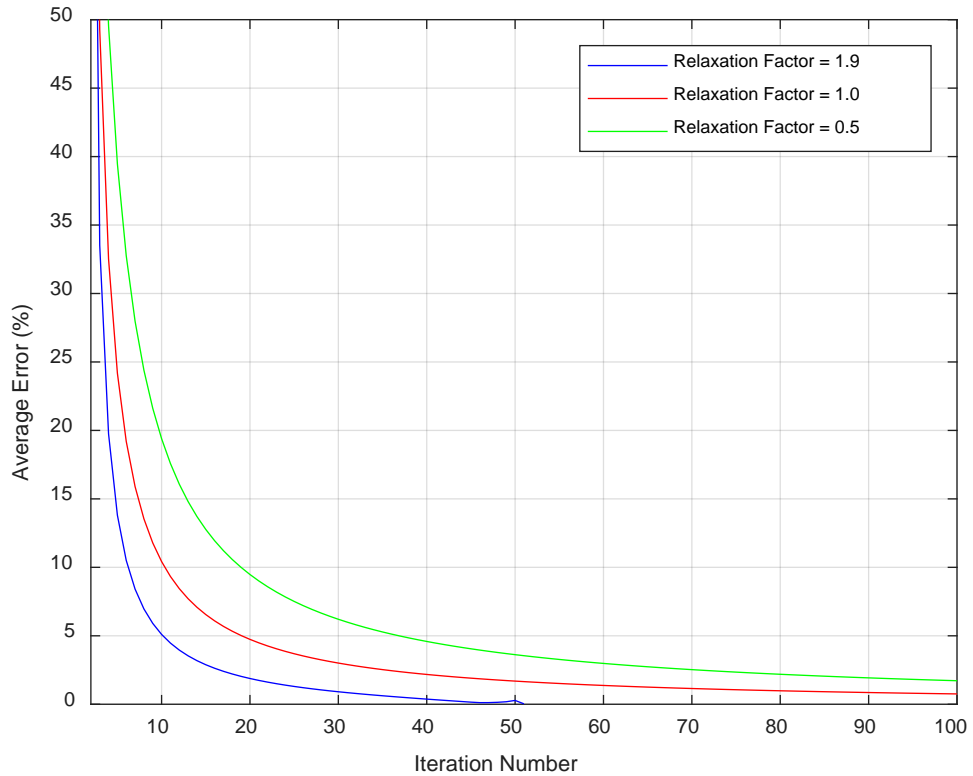


Figure 3.29: Convergence error of modeled slider bearing

It can be seen that with a larger relaxation factor, the solution converges faster, and vice versa is true; when the relaxation factor is smaller the solution takes more iterations to converge. This modeled slider bearing problem paired with the Reynolds equation is very stable and thus an uncharacteristically high value of relaxation factor (1.9) is used to emphasize convergence speed.

As previously mentioned, the Reynolds relaxation factors are typically between 1.1 and 1.2, as will be seen in the following chapter. These factors (1.1-1.2) are used due to the complex surface topography. Table 3.4 shows the relaxation factors used for the slider bearing system models.

Table 3.4: Relaxation factors for slider bearing models

Geometry	Relaxation Factor
1-D Slider bearing	1.9
2-D Slider bearing	1.9

3.3.5 Alternate Numerical Schemes

The numerical scheme outline in Section 3.3.2 utilizes the standard finite difference method of moving from left to right then up as shown in Figure 3.30. This allows for easy programming and is beneficial in stable situations.

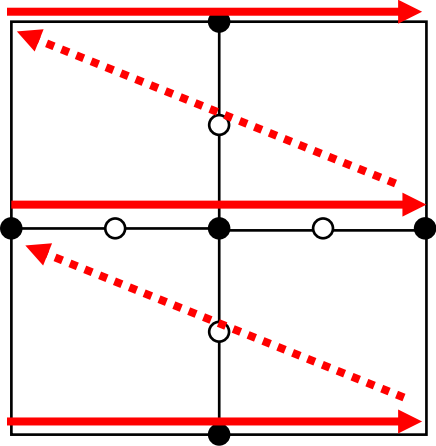


Figure 3.30: Typical progression of numerical nodal scheme calculations

A variation of this method was tested in order to verify the results of the Reynolds equation pressure solutions under various numerical schemes. Instead of moving in a repetitive synchronized path, the calculations move in a “snake” like fashion from one node to another. This allows for less of an abrupt change in pressure, or film thickness, from one node to another as the nodes flow together. Typically this scheme is very useful when dealing with unstable systems.

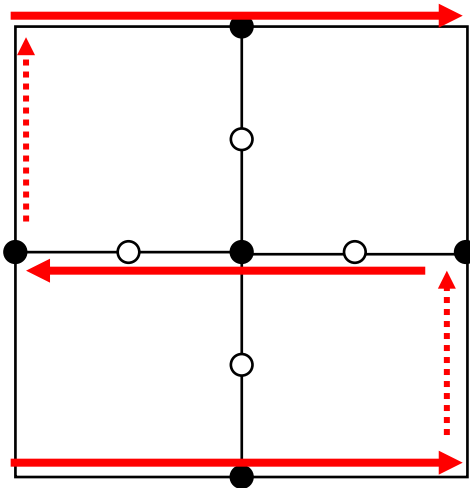


Figure 3.31: Alternate progression of numerical nodal scheme calculations

With the numerical solution to the Reynolds equation verified for 1-D and 2-D geometry of a modeled slider bearing, the same numerical modeling techniques can now be employed for the interaction of the measured cylinder wall and piston ring surfaces. Similar steps will be taken in calculating the hydrodynamic pressure between these surfaces in order to determine the effect the asperities and surface topography have on the flow of lubricant.

## CHAPTER 4

### FLOW FACTOR DERIVATION

This chapter outlines the method for deriving flow factors from specific surfaces of power cylinder components. Prior to this work, surface specific flow factors have not been used in a multi-physical model of power cylinder components. The average Reynolds equation is defined for rough surfaces in terms of shear and pressure flow factors obtained through numerical flow simulation. While the derivation remains the same, the empirical flow factor equations themselves are not universal and specific to one set of interacting surfaces.

The local film thickness is defined in terms of the nominal film thickness, and the rough surface distance from their mean levels, expressed mathematically as

$$h_T = h + \delta_1 + \delta_2 \quad (53)$$

where  $\delta_1$  and  $\delta_2$  are the local asperity distances from the mean level for each surface respectively,  $h_T$  is the local film thickness and  $h$  is the nominal film thickness. This can be seen graphically in Figure 4.1.

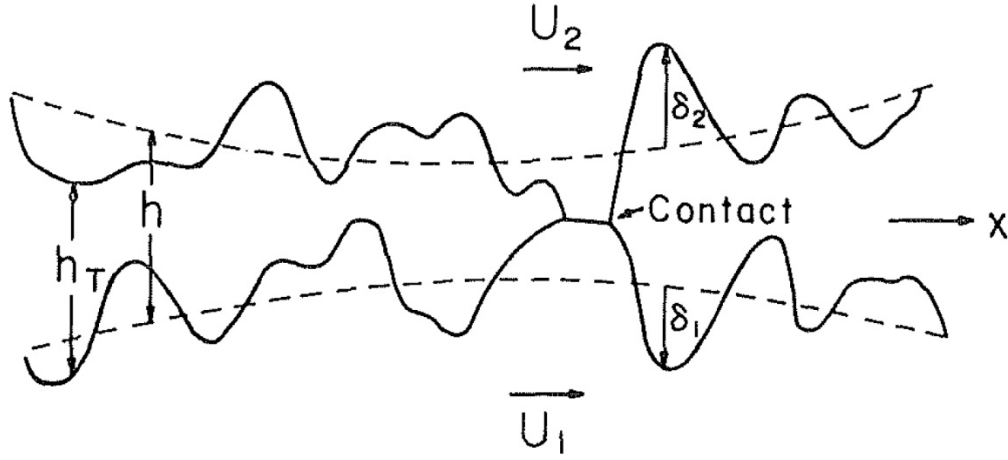


Figure 4.1: Film thickness function [1]

#### 4.1 Flow Rate Ratios

As previously mentioned, a pressure flow factor is mathematically the ratio of rough surface flow rate to smooth surface flow rate between two surfaces at one film thickness. The film thickness can then be iterated, producing various flow factors. It is therefore desired to determine the effect roughness has on the rough surface flow rate.

The local flow rates in Eq. (27) are able to be rewritten in terms of local film thickness and expressed as

$$\frac{\partial h_T}{\partial t} = -\frac{\partial q_x}{\partial x} - \frac{\partial q_z}{\partial z} \quad (54)$$

The Reynolds equation (Eq. (32)) can be written in terms of local film thickness as

$$\frac{\partial}{\partial x} \left( \frac{h_T^3}{12\mu} \frac{\partial p}{\partial x} \right) + \frac{\partial}{\partial z} \left( \frac{h_T^3}{12\mu} \frac{\partial p}{\partial z} \right) = \frac{U_1 + U_2}{2} \frac{\partial h_T}{\partial x} + \frac{\partial h_T}{\partial t} \quad (55)$$

Thusly, the local flow rates per unit width are defined from the Reynolds equation (Eq. (32)) as

$$q_x = -\frac{h_T^3}{12\mu} \frac{\partial p}{\partial x} + \frac{U_1 + U_2}{2} h_T \quad (56)$$

$$q_z = -\frac{h_T^3}{12\mu} \frac{\partial p}{\partial z} \quad (57)$$

Now considering the local flows per unit width, Eqs. (56) and (57), entering the control volume, the expected mean flow rates are able to be expressed as

$$\bar{q}_x = \frac{1}{\Delta z} \int_z^{z+\Delta z} q_x dz = \frac{1}{\Delta z} \int_z^{z+\Delta z} \left( -\frac{h_T^3}{12\mu} \frac{\partial p}{\partial x} + \frac{U_1 + U_2}{2} h_T \right) dz \quad (58)$$

$$\bar{q}_z = \frac{1}{\Delta x} \int_x^{x+\Delta x} q_z dx = \frac{1}{\Delta x} \int_x^{x+\Delta x} \left( -\frac{h_T^3}{12\mu} \frac{\partial p}{\partial z} \right) dx \quad (59)$$

We are then able to define the pressure flow factors,  $\varphi_x$  and  $\varphi_z$ , along with the shear flow factor,  $\varphi_s$ , such that the above expected mean flow rates become

$$\bar{q}_x = -\varphi_x \frac{h^3}{12\mu} \frac{\partial \bar{p}}{\partial x} + \frac{U_1 + U_2}{2} h_T + \frac{U_1 - U_2}{2} \sigma \varphi_s \quad (60)$$

$$\bar{q}_z = -\varphi_z \frac{h^3}{12\mu} \frac{\partial \bar{p}}{\partial z} \quad (61)$$

Using Eqs. (60) and (61) to modify Eq. (55), the modified Reynolds equation is obtained

$$\frac{\partial}{\partial x} \left( \varphi_x \frac{h^3}{12\mu} \frac{\partial \bar{p}}{\partial x} \right) + \frac{\partial}{\partial z} \left( \varphi_z \frac{h^3}{12\mu} \frac{\partial \bar{p}}{\partial z} \right) = \frac{U_1 + U_2}{2} \frac{\partial h_T}{\partial x} + \frac{U_1 - U_2}{2} \sigma \varphi_s + \frac{\partial h_T}{\partial t} \quad (62)$$

As  $h/\sigma \rightarrow \infty$  we know from Patir and Cheng [40], that Eq. (62) becomes the Reynolds equation for smooth surfaces and the pressure flow factors  $\varphi_x$ , and  $\varphi_z$  satisfy

$$\varphi_x, \varphi_z \rightarrow 1 \text{ as } h/\sigma \rightarrow \infty \quad (63)$$

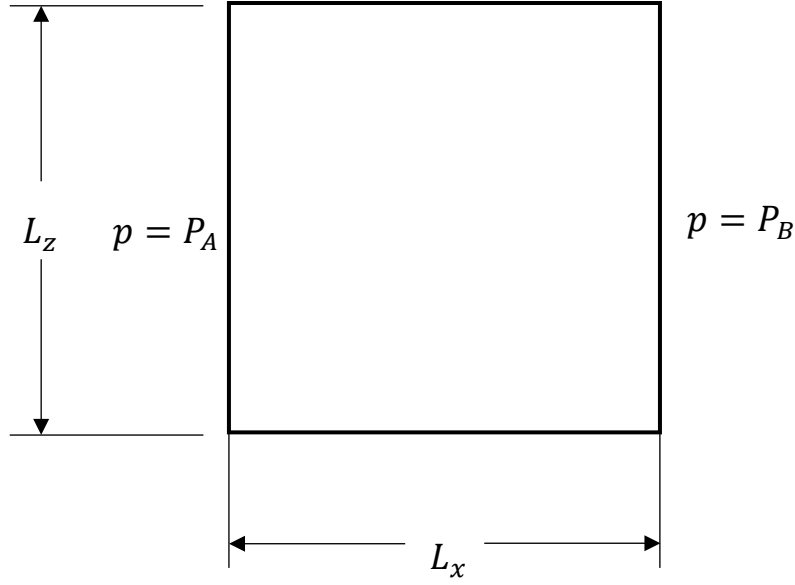


Figure 4.2: Pressure flow region for model

The average film thickness,  $h$ , is iteratively varied to get several different flow factor ratios at each of their respective surface separations. At low ratios of average film thickness no contact or overlap of the surfaces occurs for  $h/\sigma \geq 2.55$  in this piston ring-pack assembly. At locations below this film ratio, contact exists in the simulations. In the derivation of the flow factors these contact zones are set to zero pressure. However, this will change in the overall piston ring model (Chapter 5) where contact is accounted for. For every node, there is one solution of rough surface flow rate to smooth surface flow rate.

To obtain  $\varphi_x$ , we consider the following model (see Figure 4.2):

$$\frac{\partial}{\partial x} \left( \frac{h_T^3}{12\mu} \frac{\partial \bar{p}}{\partial x} \right) + \frac{\partial}{\partial z} \left( \frac{h_T^3}{12\mu} \frac{\partial \bar{p}}{\partial z} \right) = \frac{U_1 + U_2}{2} \frac{\partial h_T}{\partial x} \quad (64)$$

In looking only at the pressure flow factors, i.e. pressure driven flow between the cylinder wall and piston ring, relative sliding velocity is set to zero to isolate the effect of the applied nominal pressure gradient on the surface topography. By doing so, Eq. (64) becomes

$$\frac{\partial}{\partial x} \left( \frac{h_T^3}{12\mu} \frac{\partial \bar{p}}{\partial x} \right) + \frac{\partial}{\partial z} \left( \frac{h_T^3}{12\mu} \frac{\partial \bar{p}}{\partial z} \right) = 0 \quad (65)$$

Using the mean flow rate in the  $x$  direction ( $\bar{q}_x$ ) by setting Eqs. (58) and (60) equal, cancelling terms, and simplifying, the  $x$  direction pressure flow factor becomes:

$$\varphi_x = \frac{\frac{1}{\Delta z} \int_z^{z+\Delta z} \left( -\frac{h_T^3}{12\mu} \frac{\partial p}{\partial x} \right) dz}{\frac{h^3}{12\mu} \frac{\partial \bar{p}}{\partial x}} \quad (66)$$

For the  $z$  direction pressure flow factor, a pressure gradient is applied in the  $z$  direction. Following a similar procedure, the  $z$  direction pressure flow factor becomes:

$$\varphi_z = \frac{\frac{1}{\Delta x} \int_x^{x+\Delta x} \left( -\frac{h_T^3}{12\mu} \frac{\partial p}{\partial z} \right) dx}{\frac{h^3}{12\mu} \frac{\partial \bar{p}}{\partial z}} \quad (67)$$

The pressure flow factors are now in their final form representing the ratio of rough surface flow rate to smooth surface flow rate.  $\varphi_x$  and  $\varphi_z$  are calculated at each node and then averaged over the entire surface to find a single value representing the average flow rate of the entire surface at that respective film thickness.

The shear flow factor is calculated differently than the pressure flow factors and requires the cylinder wall surface and piston ring surface to be analyzed separately. With this, the transportation of lubricant due to surface roughness is obtained for each surface. From Patir and Cheng [40] it is known that

$$\varphi_s \rightarrow 0 \text{ as } h/\sigma \rightarrow \infty \quad (68)$$

The discretization technique resembles that of Section 3.3.2. Thusly, in conjunction with the average Reynolds equation (Eq. (32)) the shear flow factor for each respective surface is calculated as

$$\Phi_{s,i} = \frac{2}{L_x L_z} \int_0^{L_x} \int_0^{L_z} \left( -\frac{h_T^3}{12\eta} \frac{\partial p}{\partial x} \right) dz dx \quad i = 1,2 \quad (69)$$

The compound shear flow factor is a function of  $\Phi_{s,1}$  and  $\Phi_{s,2}$  and are convoluted through each surfaces variance ratios given as

$$V_{r1} = \left( \frac{\sigma_1}{\sigma} \right)^2 \quad \text{and} \quad V_{r2} = \left( \frac{\sigma_2}{\sigma} \right)^2 \quad (70)$$

Therefore, in combining Eqs. (69) and (70) the cumulative shear flow factor may be written as

$$\varphi_s = \left( \frac{\sigma_1}{\sigma} \right)^2 \Phi_{s,1} + \left( \frac{\sigma_2}{\sigma} \right)^2 \Phi_{s,2} \quad (71)$$

Keeping in mind that  $\Phi_s$  is associated with a single surface and  $\varphi_s$  is associated with the case when both surfaces are brought together.

#### 4.2 Boundary Conditions

In solving the Reynolds equation the initial conditions, or boundary conditions, must be set to solve the hydrodynamic pressure at each node. The boundary conditions depend on the type of flow being analyzed, Poiseuille or Couette. These specific boundary conditions are set for the derivation of the flow factors only. Other applications-based boundary conditions are set in the whole piston ring model.

#### *4.2.1 Pressure Flow Factor Boundary Conditions*

In order to derive the pressure flow factors, an arbitrary pressure gradient is induced between the cylinder wall and the piston ring in the  $x$  and  $z$  directions separately without any shearing or sliding velocity of the surfaces. This ensures only Poiseuille flow is simulated in examining  $\varphi_x$  and  $\varphi_z$ . In this case from 100 Pa to 400 Pa. While those two boundaries remain fixed, the other two sides of the surface have periodic boundary conditions. This ensures that at the same rate any amount of lubricant leaves one side, it enters the opposite side. Thus there is no net change in volume of fluid leaving the system. These boundary conditions are held for any pressure gradient applied, effectively holding the mass flow rate constant.

#### *4.2.2 Shear Flow Factor Boundary Conditions*

When considering the shear flow factor, only shearing effects are considered. No initial pressure gradient is applied, however a relative sliding velocity between the surfaces is. Therefore, on all four sides of the surface interactions periodic boundary conditions are applied. This ensures the amount of mass flowing in the simulation stays the same. As the lubricant enters from one direction it leaves in the other direction. This is true in the direction of flow and in the transverse direction.

These periodic boundary conditions were not utilized in Patir and Cheng's [1, 40] derivation of the flow factor equations. Instead, it was assumed there was no flow across the boundaries.

### 4.3 Pressure Flow Factor

The  $x$  and  $z$  direction pressure flow factors must be derived separately. Figures 4.3 and 4.4 show the interaction of these two surfaces in the rough surface Poiseuille flow calculations.

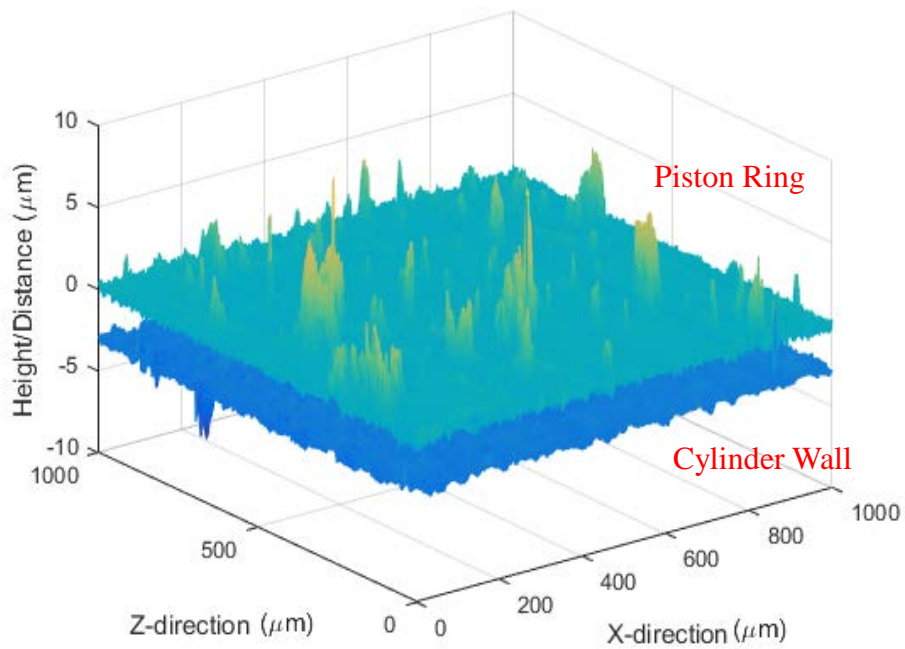


Figure 4.3: Interacting power cylinder components (Isometric View)

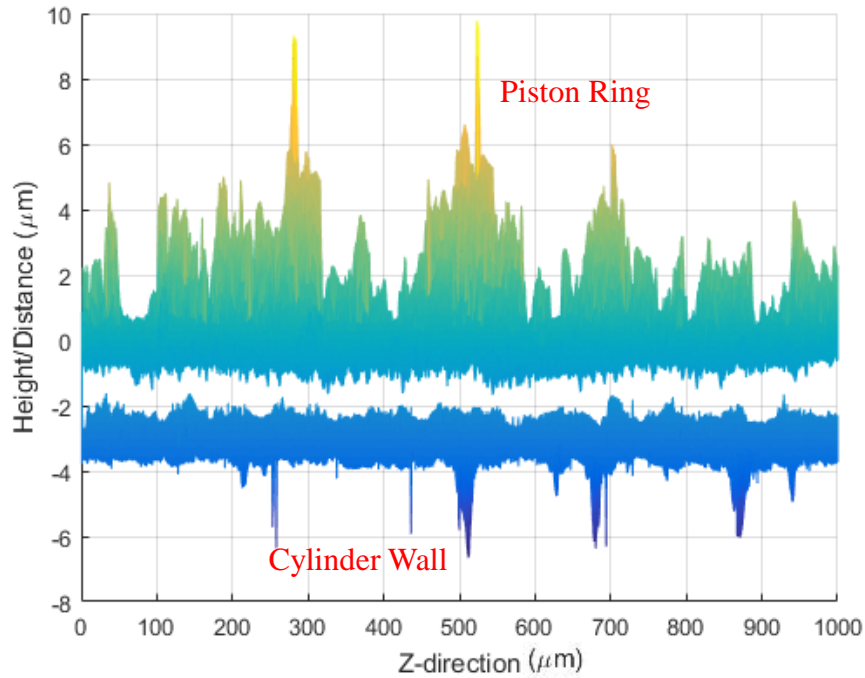


Figure 4.4: Interacting power cylinder components (Y-Z View)

The Reynolds equation is solved for the pressure flows using the finite difference method by setting up a nodal network shown in Fig. 3.20, as previously mentioned. Upon discretization of the film thickness at each intermediate node, the pressure at each node is solved for based on a convergence criteria of 0.1%. By using this same methodology for the rough surfaces in question, as well as two arbitrary smooth surfaces with the same nominal film thickness and induced pressure gradient, we are able to get the ratio of rough surface flow rate to smooth surface flow rate.

The range of the pressure gradient does not matter in this case, what does matter is the pressure changes due to the asperities relative to the smooth surface case. The flow factor looks at

the change in hydrodynamic pressure between the smooth surface pressure gradient and the rough surface pressure gradient. This ensures the results are a function of local asperities effect on hydrodynamic pressure only. As previously mentioned, the arbitrary pressure gradient applied is from  $100Pa$  to  $400Pa$ . The gradient is first applied in the  $x$  direction, followed by the  $z$  direction.

#### *4.4 Shear Flow Factor*

The derivation of the shear flow factor is more complex, and requires the problem to be broken down into several parts. The shear flow factor is a numerically simulated flow quantity that relates the effect of neighboring asperities with each other in terms of pure shearing. When shearing is introduced there is the possibility of cavitation at the trailing edge of the asperities [40]. In the present study, cavitation is included in the numerical Reynolds solution. However, a relative sliding speed of  $1m/s$  was used in the derivation and did not induce negative pressures large enough to induce cavitation. The magnitude of these pressures is related to the sliding speed and rough surface geometry.

In dealing with shearing between channels, locations of decreased pressure (e.g. below the reference pressure) are possible along the flow direction just at the edge of the channel. The load-carrying capacity is not greatly affected, when this reference pressure is above atmospheric, as these sites occur near the trailing edge of the valleys of the surface.

Two reference pressures are tested to validate the consistency of the change in the hydrodynamic pressure. One pressure is tested in a vacuum at  $0 kPa$  to test for cavitation and the second is tested at atmospheric ( $101,325 Pa$ ) for the solution among power cylinder components.

The change in hydrodynamic pressure among the surfaces can then be compared and validated regardless of reference pressure.

An analysis of the two interacting surfaces is completed by simulating the hydrodynamic effects of each surface separately, sliding against a smooth surface in the absence of any pressure induced gradient. This allows for the extraction of the flow parameters from each surface individually based only on shearing effects. The model was run with the parameters shown in Table 4.1.

Table 4.1: System Parameters

Parameter	Variable	Value	Units
Dynamic viscosity	$\mu$	0.1	$Pa \cdot s$
Relative Velocity	$u$	1	$m/s$

#### 4.4.1 Ambient Pressure of 0 kPa

Figures 4.5-4.7 show the results of the pressure calculations from the cylinder wall sliding parallel to a smooth surface along the  $z$  direction. In Figure 4.5, pressure is seen to be larger in the grooves, as marked by the lighter colors. This agrees with theory as this is where the load-carrying capacity is generated (Seen in Section 3.1.4.1). It can also be seen that the fluid cavitates at the trailing edge of the grooves in the direction of flow, as marked by the darker colors. In Figure 4.6 the entire surface's hydrodynamic pressure gradient is seen as a result of pure shearing. Figure 4.7 is a zoomed in isometric view of Figure 4.5. The grooves can be seen clearly where the pressure is primarily generated.

Based on the common practice of assuming fluid cavitates at negative pressures, this suggests cavitation could occur. However, this neglects the effect of the ambient pressure, which is atmospheric in this case.

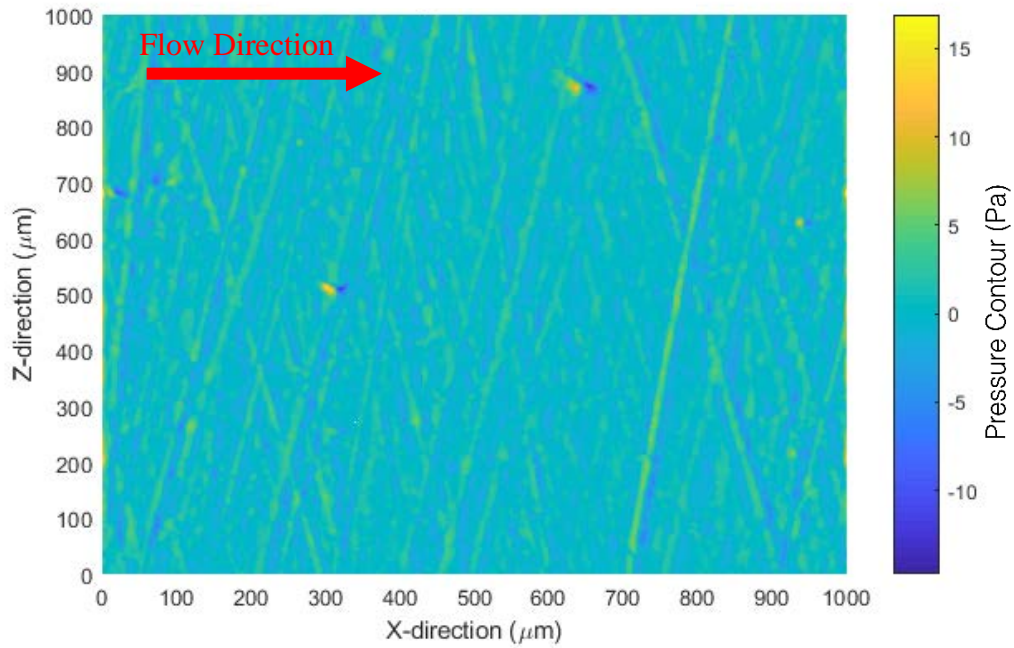


Figure 4.5: Cylinder wall pressure distribution due to shearing (Top View)

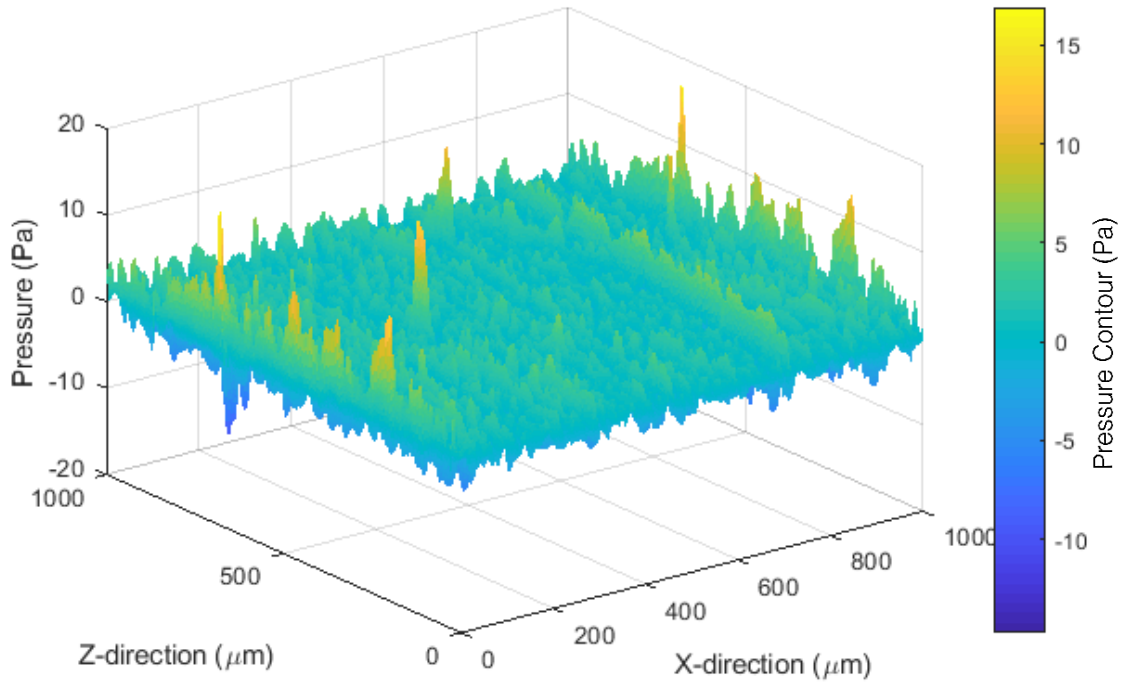


Figure 4.6: Cylinder wall pressure distribution due to shearing (Isometric View)

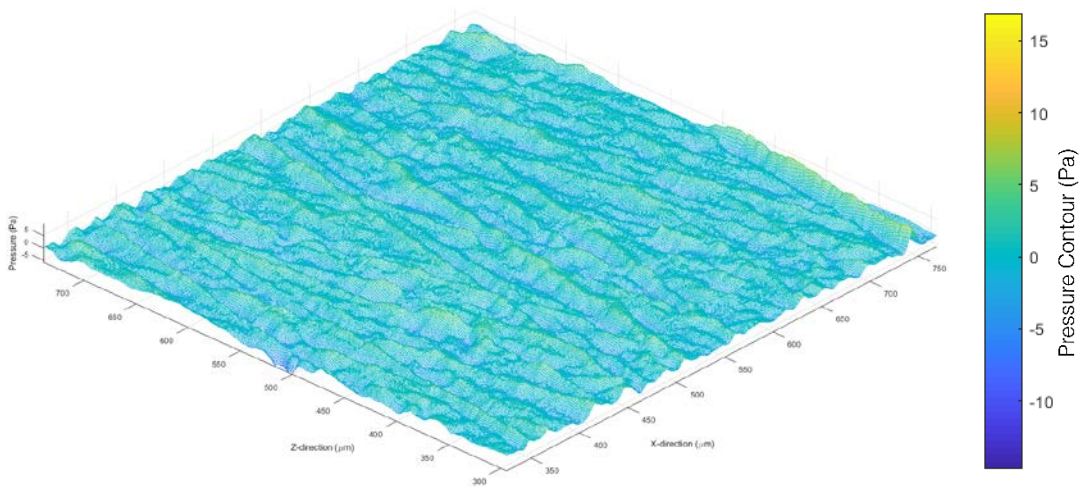


Figure 4.7: Cylinder wall pressure distribution due to shearing (Isometric View)

Due to the reference pressure being at zero, which is common when modeling using the gage pressure, this is also synonymous of a space of vacuum application. While beyond the scope of this thesis it is noted that even at this reference pressure this specific surface topography will generate cavitation sites at the trailing edge of the grooves, as marked by the negative pressure.

The total hydrodynamic load carrying capacity is given as

$$F = \int p dA \quad (72)$$

Recalling that the surface dimensions are  $1000\mu\text{m} \times 1000\mu\text{m}$ , the total load carrying capacity for the cylinder wall surface is  $0.001N$ . With no cavitation included in the model, this represents numerical error. This implies that there is just as much positive pressure as there is negative pressure in these grooves, which can be seen by the balance of pressure above and below zero in Figure 4.8.

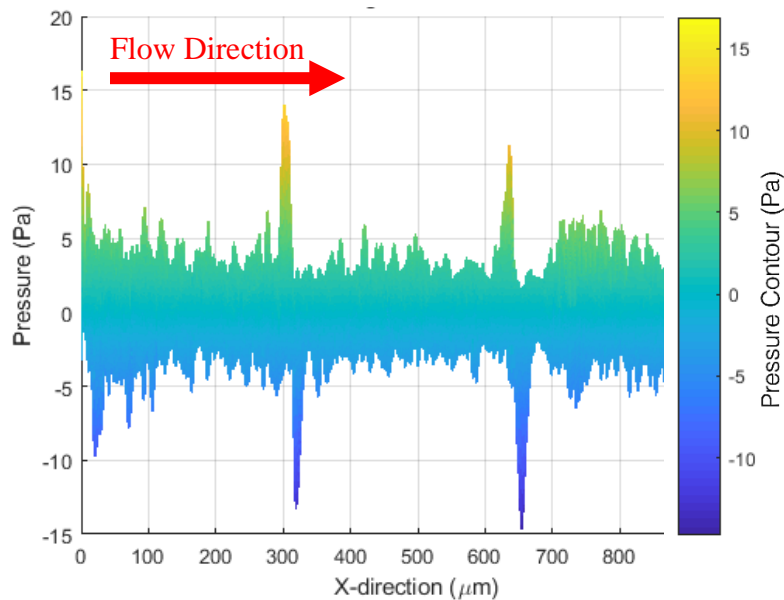


Figure 4.8: Cylinder wall pressure distribution due to shearing (X-Y View)

The piston ring is now run through the same model at  $0\text{ kPa}$ , with the same system parameters, against a smooth surface. In Figure 4.9, pressure is seen to be larger in the pores of the piston ring, as marked by the lighter colors, similar to the cylinder wall grooves. It can be seen that if the fluid is to leave these pores there is cavitation pressure at the trailing edge as marked by the darker colors. These pressures inside the pores are also observed to be larger than anywhere on the surface of the cylinder. This is due to the depth of the surface topography; as pressure is generated at the front of the wedge shape geometry, negative pressure is induced at the trailing edge of the pore. This resting fluid in the pore is able to generate large amounts of pressure over a small area. In Figure 4.10 the entire surface's hydrodynamic pressure gradient is seen as a result of pure shearing. Figure 4.11 shows a side view of the piston ring surface. The pressure in the pores can be seen by the lighter color spikes. Following the lighter color positive spikes, in the direction of flow, are the darker color negative spikes, i.e. the cavitation sites.

The load carrying capacity is calculated in the same manner and is seen to be  $0.003\text{ N}$ . Similarly, with no cavitation in the model, this is numerical error. For previously mentioned reasons this agrees with theory as this is the load carried in a vacuum.

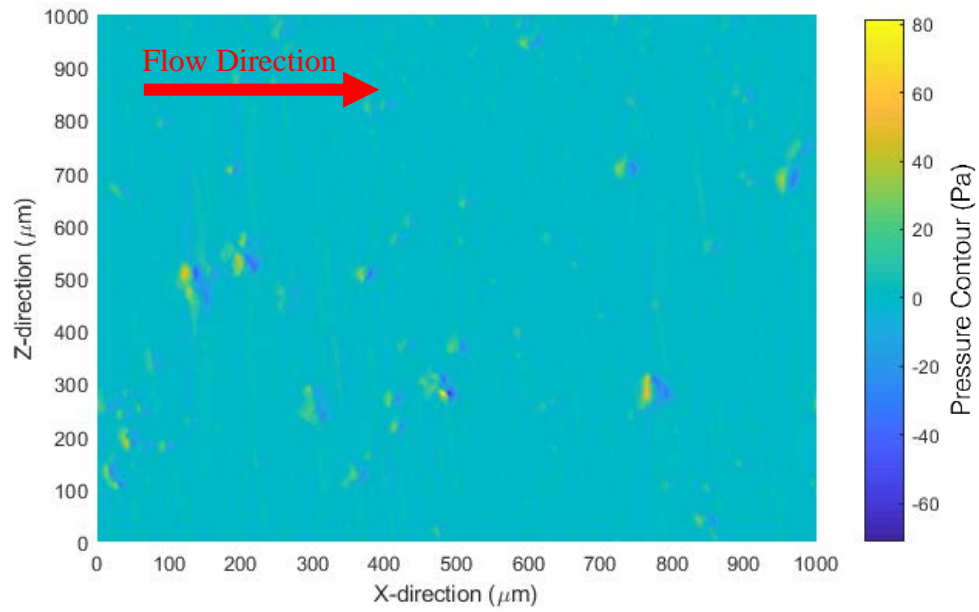


Figure 4.9: Piston ring pressure distribution due to shearing (Top View)

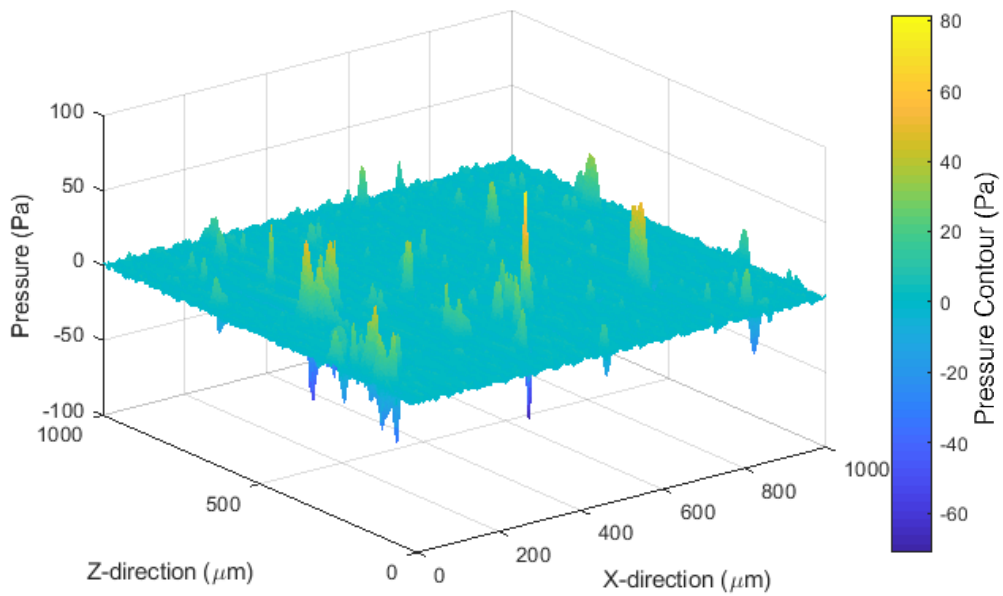


Figure 4.10: Piston ring pressure distribution due to shearing (Isometric View)

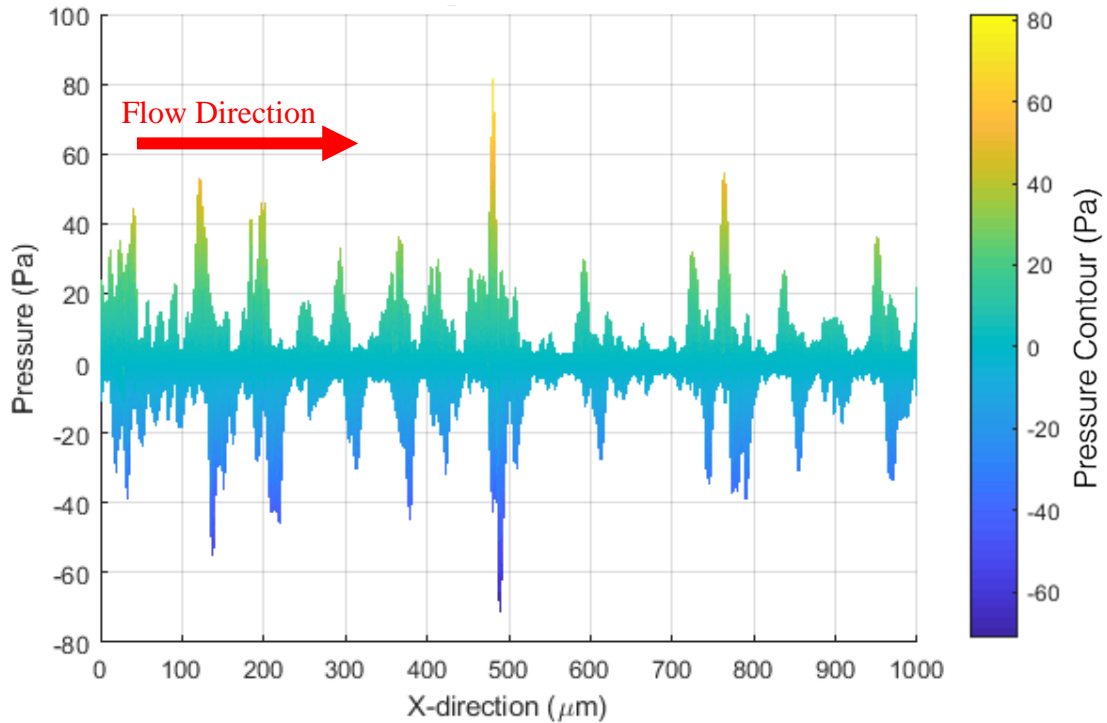


Figure 4.11: Piston ring pressure distribution due to shearing (X-Y View)

#### 4.4.2 Ambient Pressure of 101 kPa

The reference pressure is now raised to atmospheric (101kPa) with the same system parameters. With this the cylinder wall against a smooth surface is simulated first. The results of shearing for the cylinder wall at an ambient pressure of atmospheric are shown in Figures 4.12 and 4.13. Similar decreases in pressure are seen due to shearing across asperities near the grooves. The load carrying capacity was calculated in a similar manner using Eq. (72). The result was found to be a load of 101N, similar to the reference pressure. Since no cavitation is included, no load support is generated (i.e.  $F = P_{ambient}A$ ).

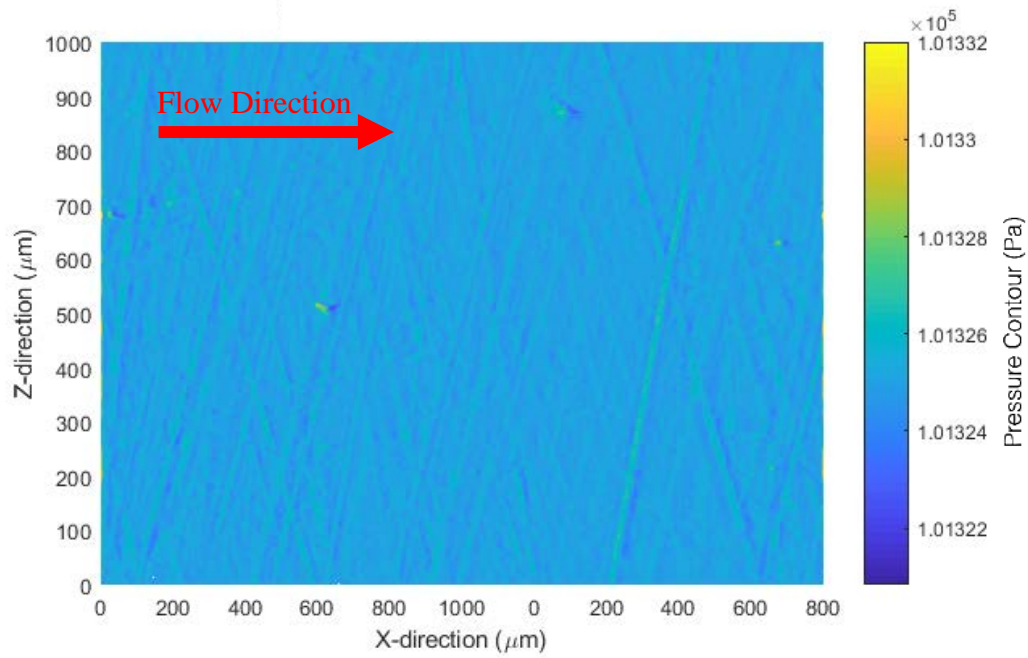


Figure 4.12: Cylinder wall pressure distribution due to shearing without cavitation (Top View)

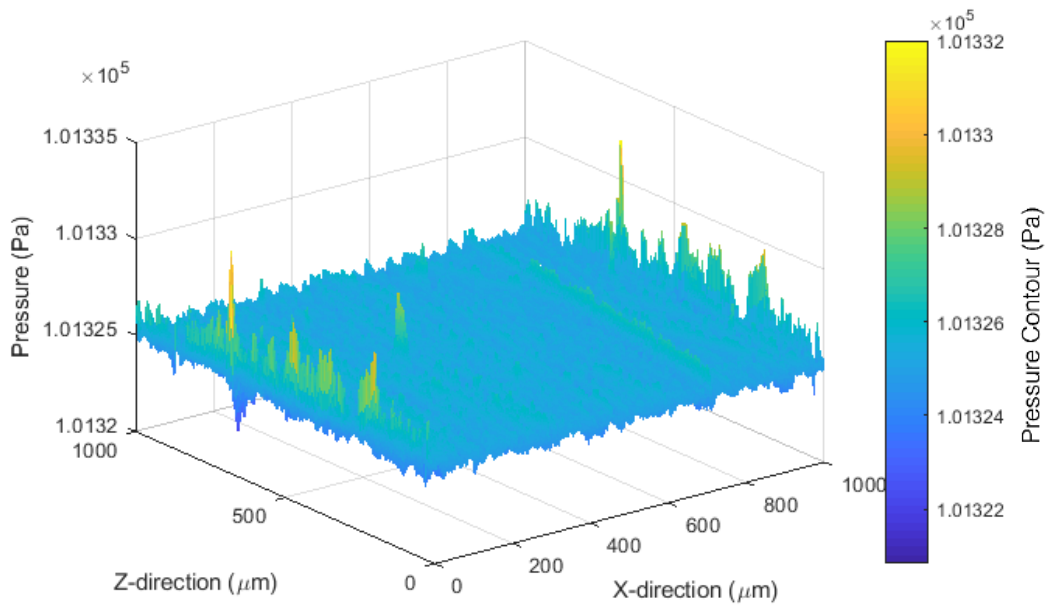


Figure 4.13: Cylinder wall pressure distribution due to shearing without cavitation (Isometric View)

The piston ring is now run through the same model at an ambient pressure of  $101\text{ kPa}$ , with the same system parameters, against a smooth surface. Similar decreases in pressure are seen due to shearing across asperities near the pores. Due to a much larger reference pressure, the relative change in pressures is very small and hence it is difficult to see the amount of change in pressures. This can be seen in Figures 4.14 and 4.15.

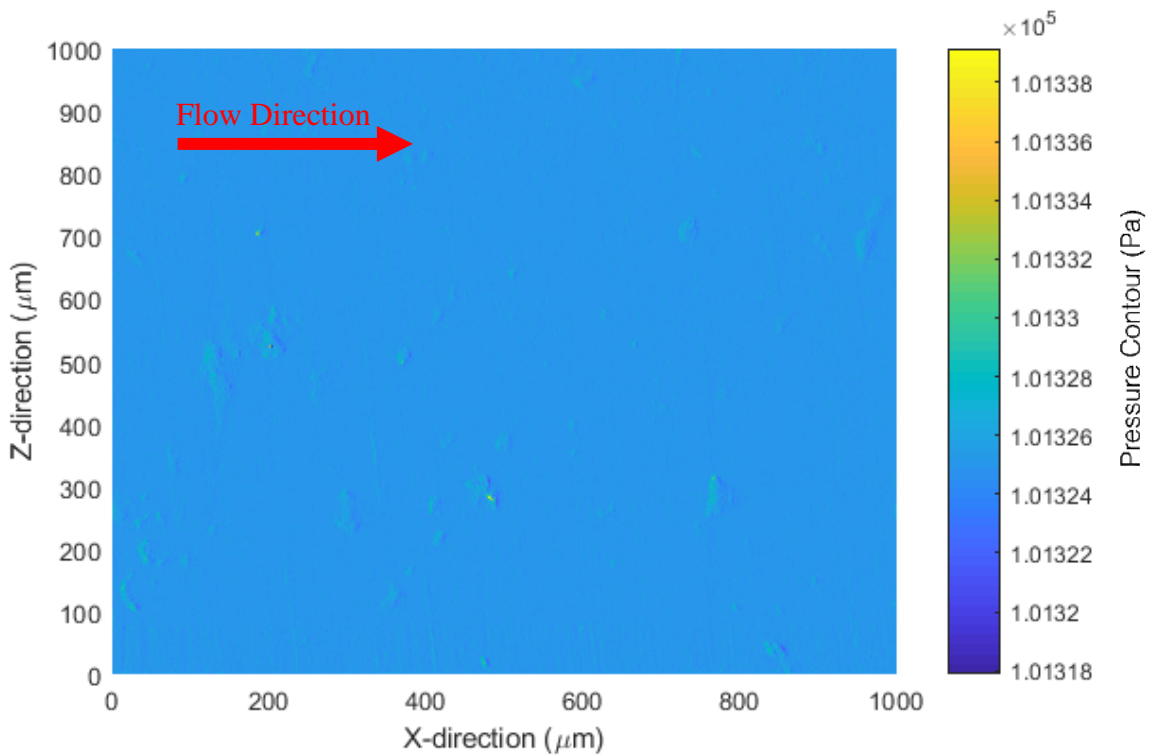


Figure 4.14: Piston ring pressure distribution due to shearing (Top View)

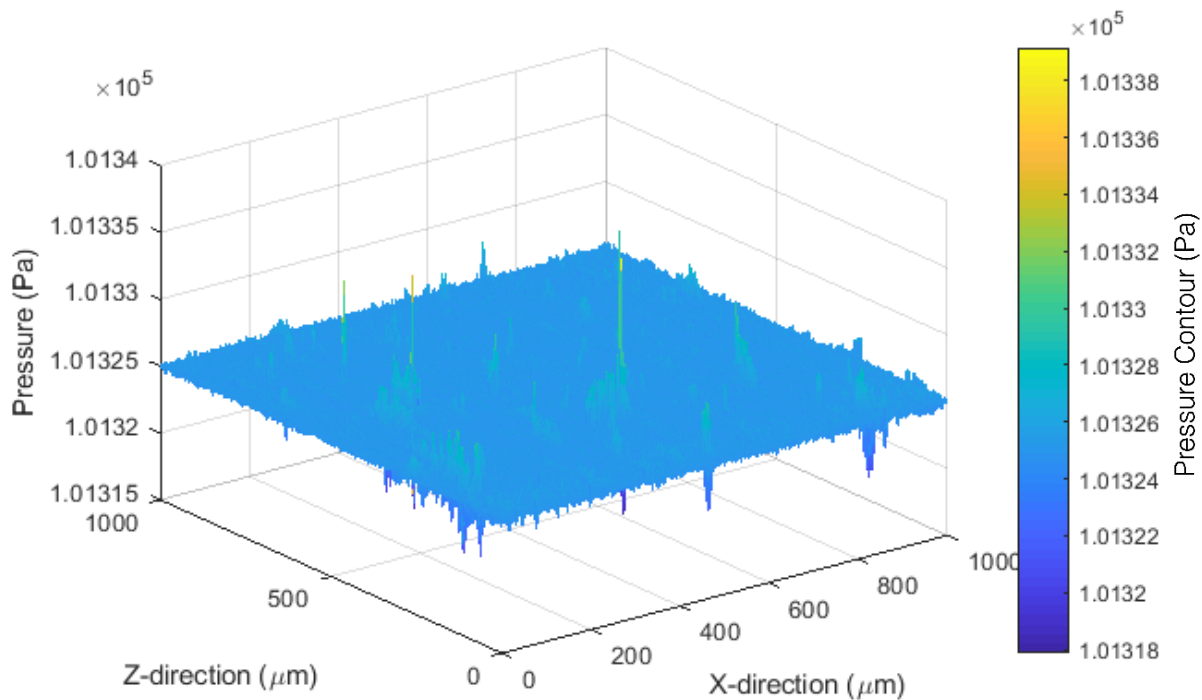


Figure 4.15: Piston ring pressure distribution due to shearing (Isometric View)

Table 4.2 shows the total calculated load-carrying capacity of each surface for the various cases. It may be noticed that the loads at ambient pressure are almost identical to the ambient pressure multiplied by the area. This is because the amount of pressure change due to the asperities is minimal in comparison to the atmospheric reference pressure. The simulation using zero ambient pressure shows the hydrodynamic pressures to be on the scale of ( $10^1 Pa$ ), as opposed to the case when assuming atmospheric at the boundaries, the hydrodynamic pressures are on the sale of ( $10^5 Pa$ ).

Table 4.2: Load carrying capacity due to numerical error results

Surface	$P_{Reference}$ (kPa)	Load-Carrying Capacity (N) due to numerical error
Cylinder wall	0	0.001
Piston ring	0	0.003
Cylinder wall	101	101
Piston ring	101	101

With this change in pressure, the hydrodynamic pressure deviations from the reference pressure are noticed to be very similar at each node from both cases of reference pressure. This validates the hydrodynamic pressures are correct in the calculation of the shear flow factor.

#### 4.5 Numerical Results

Following the surface specific flow factor method outlined, several iterations were run by varying the film thickness in analyzing the sample surface set. Along with this, the  $x$  and  $z$  direction pressure gradients are also altered for  $\varphi_x$ , and  $\varphi_z$ , respectively. With the Cross Correlation Function also calculated, a comparison to previous works [1, 40] can now be made knowing both Peklenik numbers. When Patir and Cheng [1, 40] fit their flow factor equations they modeled several different Peklenik values. They were able to generate coefficients for their empirical fits based on the Peklenik number ( $\gamma$ ). Their fit equation is of the form

$$\varphi_x = 1 - C e^{-r(h/\sigma)} \quad \text{for } \gamma \leq 1 \quad (73)$$

$$\varphi_x = 1 + C(h/\sigma)^{-r} \quad \text{for } \gamma > 1 \quad (74)$$

Their numerical results for the pressure flow factor coefficients are tabulated in Table 4.3.

Taking the same coordinate system, they also found  $\varphi_z$  to be equal to  $\varphi_x$  corresponding to the reciprocal directional properties. In functional form

$$\varphi_x(H, \gamma) = \varphi_z(H, 1/\gamma) \quad (75)$$

Table 4.3: Coefficient of Eqs. (73) and (74) for  $\varphi_x$  and  $\varphi_z$  [1]

$\gamma$	<b>C</b>	<b>r</b>	<b>Range</b>
1/9	1.48	0.42	$H > 1$
1/6	1.38	0.42	$H > 1$
1/3	1.18	0.42	$H > 0.75$
1	0.90	0.56	$H > 0.5$
3	0.225	1.5	$H > 0.5$
6	0.520	1.5	$H > 0.5$
9	0.870	1.5	$H > 0.5$

Their shear flow factor is of the form

$$\varphi_s = A_1(h/\sigma)^{\alpha_1} e^{-\alpha_2(h/\sigma) + \alpha_3(h/\sigma)^2} \quad \text{for } (h/\sigma) \leq 5 \quad (76)$$

$$\varphi_s = A_2 e^{-0.25(h/\sigma)} \quad \text{for } (h/\sigma) > 5 \quad (77)$$

where the coefficients are given in Table 4.4

Table 4.4: Coefficient of Eqs. (76) and (77) for  $\varphi_s$  [40]

$\gamma$	$A_1$	$\alpha_1$	$\alpha_2$	$\alpha_3$	$A_2$
1/9	2.046	1.12	0.78	0.03	1.856
1/6	1.962	1.08	0.77	0.03	1.754
1/3	1.858	1.01	0.76	0.03	1.561
1	1.899	0.98	0.92	0.05	1.126
3	1.560	0.85	1.13	0.08	0.556
6	1.290	0.62	1.09	0.08	0.388
9	1.011	0.54	1.07	0.08	0.295

Keep in mind that these values were calculated for statistically generated Gaussian surfaces. There are differences expected in this work having derived the flow factor quantities from specific surfaces. Recall that it was shown in Sections 4.1 as  $h/\sigma \rightarrow \infty$  we know, that the average Reynolds equation (Eq. (62)) becomes the Reynolds equation for smooth surfaces and the flow factors  $\varphi_x$ ,  $\varphi_z$ , and  $\varphi_s$  satisfy

$$\varphi_x, \varphi_z \rightarrow 1 \text{ and } \varphi_s \rightarrow 0 \text{ as } h/\sigma \rightarrow \infty \quad (78)$$

As mentioned in Section 3.3.4, relaxation techniques were taken enhance convergence based on the flow factor being derived. Table 4.5 summarizes the relaxation factors for the various simulations.

Table 4.5: Relaxation factors for simulation cases

<b>Simulation Case</b>	<b>Relaxation Factor</b>
Couette flow, Cylinder wall against Smooth surface	1.1
Couette flow, Piston ring against Smooth surface	1.1
Poiseuille flow, Rough surfaces, X direction	1.2
Poiseuille flow, Smooth surfaces, X direction	1.9
Poiseuille flow, Rough surfaces, Z direction	1.2
Poiseuille flow, Smooth surfaces, Z direction	1.9

#### *4.5.1 X-Direction Pressure Flow Factor*

It can be seen in Figures 4.16 and 4.17 that the pressure is constant at the boundaries of  $x = 0$  and  $x = 1000\mu m$ . Figure 4.16 shows the pressure gradient between two smooth surfaces. Figure 4.17 shows the results for the same nominal pressure gradient applied between the cylinder wall and the piston ring rough surfaces at the same nominal film thickness.

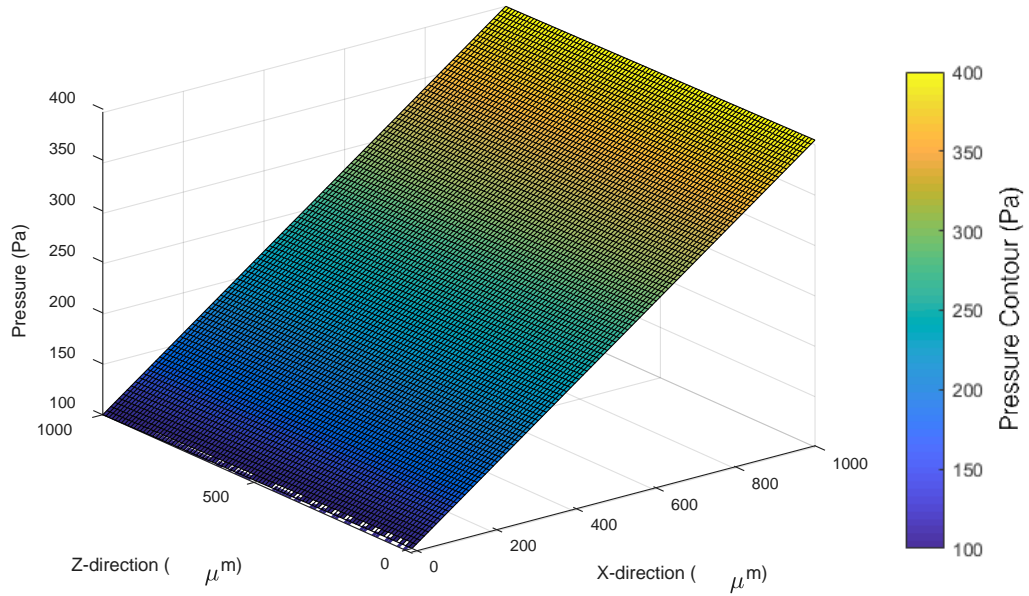


Figure 4.16: Poiseuille flow in  $x$  direction for smooth surfaces

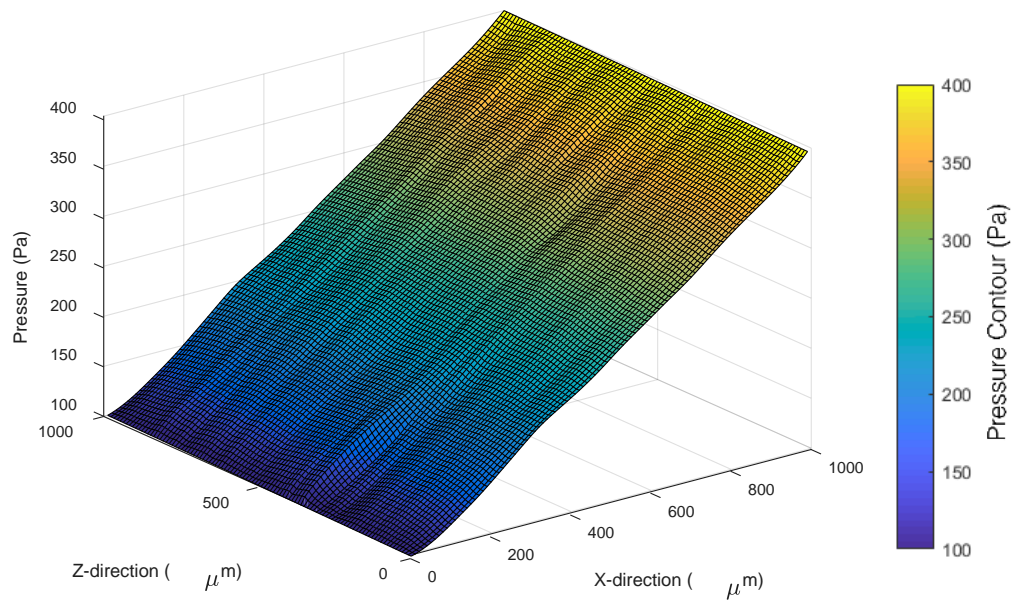


Figure 4.17: Poiseuille flow in the  $x$  direction for rough surfaces

The surface asperity features are seen to affect the pressure gradient in the direction of flow, thus influencing the flow rate at each node as well. From this, the ratio of the rough surface flow rate to smooth surface flow rate, at this film thickness, is able to be calculated for the prescribed flow factor.

Multiple flow factor ratios are calculated by iterating the film thickness. The flow factor value can then be plotted against the changing film thickness. Shown in Figure 4.18 is the derived  $x$  direction pressure flow factor,  $\phi_x$ , raw data and its curve fit for the considered power cylinder surfaces, as well as its comparison to Patir and Cheng's [1] statistical model.

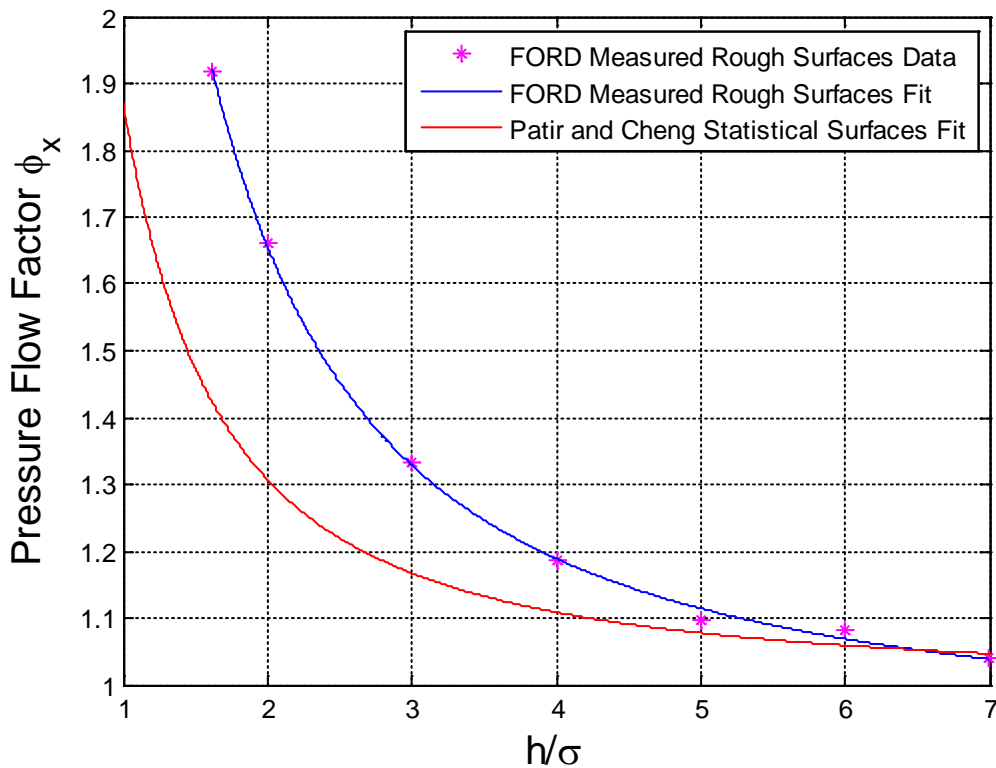


Figure 4.18:  $\phi_x$  pressure flow factor

Fitting the flow factor curve with an empirical equation results in the new flow factor equation given by Eq. (79).

$$\varphi_x = 2.4827(h/\sigma)^{-1.6955} + 0.9752 \quad (79)$$

It is noticed that with the derived  $x$  direction pressure flow factor, surface specific roughness is predicted to have a larger influence on pressure driven flow than a Gaussian surface roughness.

#### *4.5.2 Z-Direction Pressure Flow Factor*

The  $z$  direction flow factor is calculated in a similar manner; by applying the same pressure gradient between the two surfaces in the  $z$  direction, calculating the flow rate ratio, and iterating the film thickness to calculate several flow rate ratios to acquire an empirical flow factor curve.

The result for the smooth surfaces can be seen in Figure 4.19, while the rough surface result can be seen in Figure 4.20. In the  $z$  direction the roughness is seen to have less effect than in the  $x$  direction (Figure 4.17). This is due to the grooves and specific surface topography mentioned in Section 3.1.4.1.

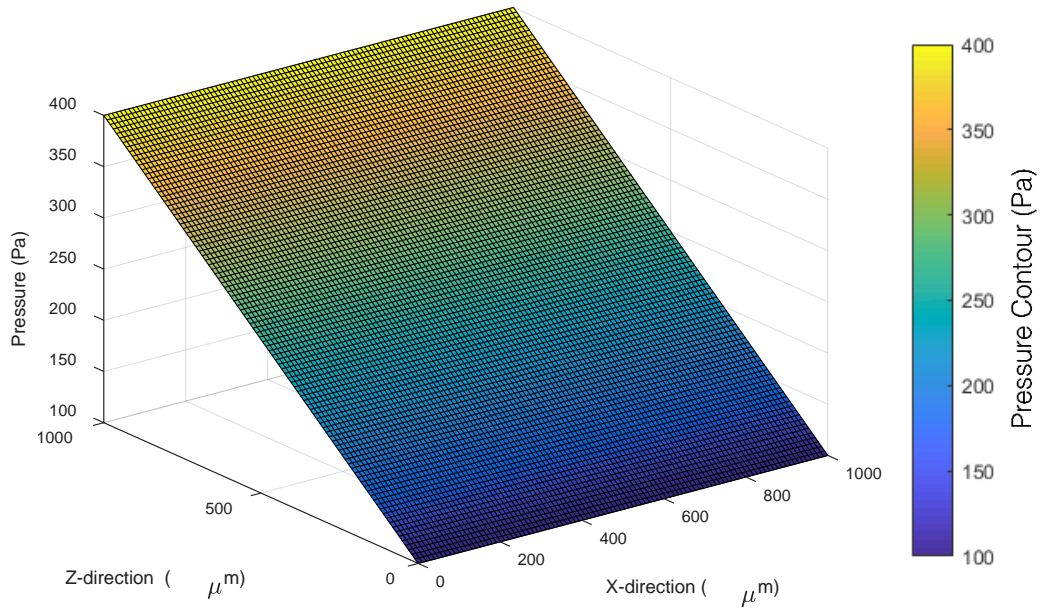


Figure 4.19: Poiseuille flow in  $z$  direction for smooth surfaces

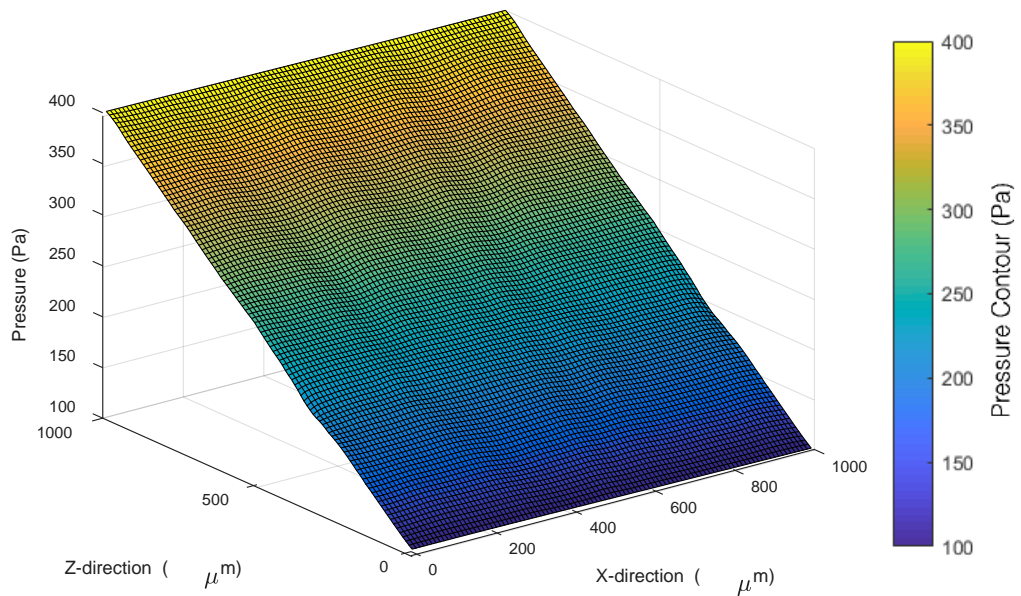


Figure 4.20: Poiseuille flow in the  $z$  direction for rough surfaces

Upon iterating the film thickness, the  $z$  direction pressure flow factor curve is obtained. With the  $z$  direction pressure flow factor there is a larger discrepancy between the statistical models and the surface specific model, as seen in Figure 4.21. At  $h/\sigma$  less than 4, the measured surfaces are seen to better channel the flow of lubricant compared to the statistically generated surfaces. This agrees with the theory behind the cross-hatching as discussed in Section 3.1.4.2.

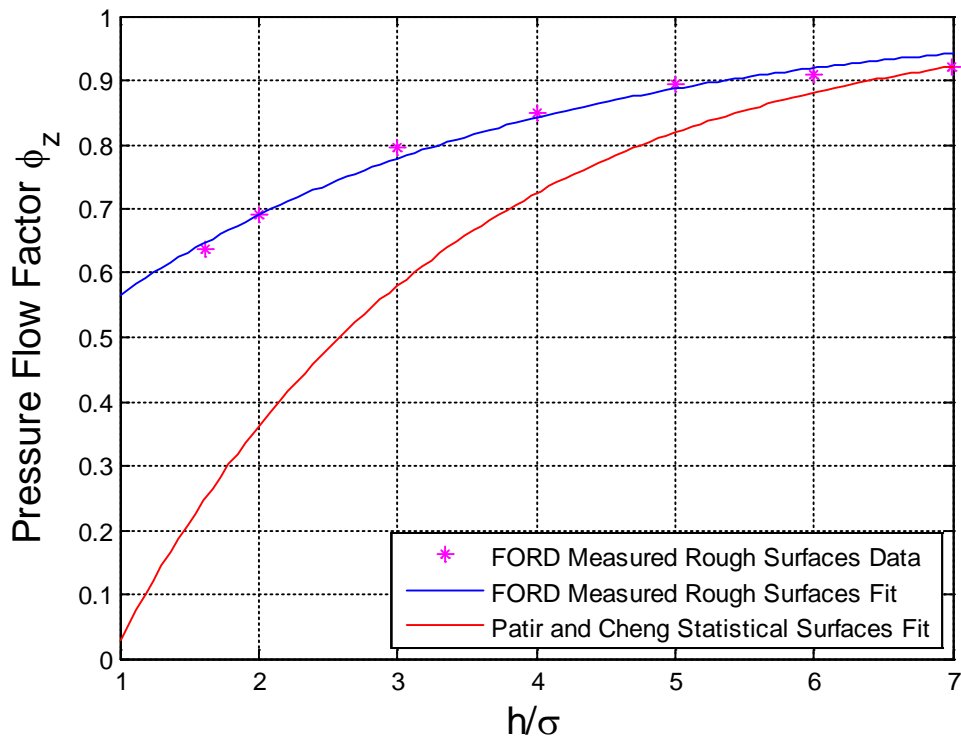


Figure 4.21:  $\phi_z$  pressure flow factor

The new  $z$  pressure flow factor's empirical fit for the piston ring and cylinder wall surfaces is

$$\phi_z = 1 - 0.4824e^{-0.2477(h/\sigma)} \quad (80)$$

Similar to Patir and Cheng, the same relationship is established for surface specific flow factor quantities. For the same set of surfaces,  $\varphi_x$  and  $\varphi_z$  are seen to be related through their film thickness, root mean square roughness, and the Peklenik number as

$$\varphi_x(H, \gamma) = \varphi_z(H, 1/\gamma) \quad (81)$$

#### 4.5.3 Shear Flow Factor

The shear flow factor, as previously stated, must be calculated for each surface separately against a smooth surface then convoluted for the governing shear flow factor. Figure 4.22 shows the cylinder wall shear flow factor,  $\Phi_{s,1}$ , as well as the piston ring shear flow factor,  $\Phi_{s,2}$ . With the convolution of  $\Phi_{s,1}$  and  $\Phi_{s,2}$ , the governing shear flow factor,  $\phi_s$  is able to be calculated, plotted, and curve fit.

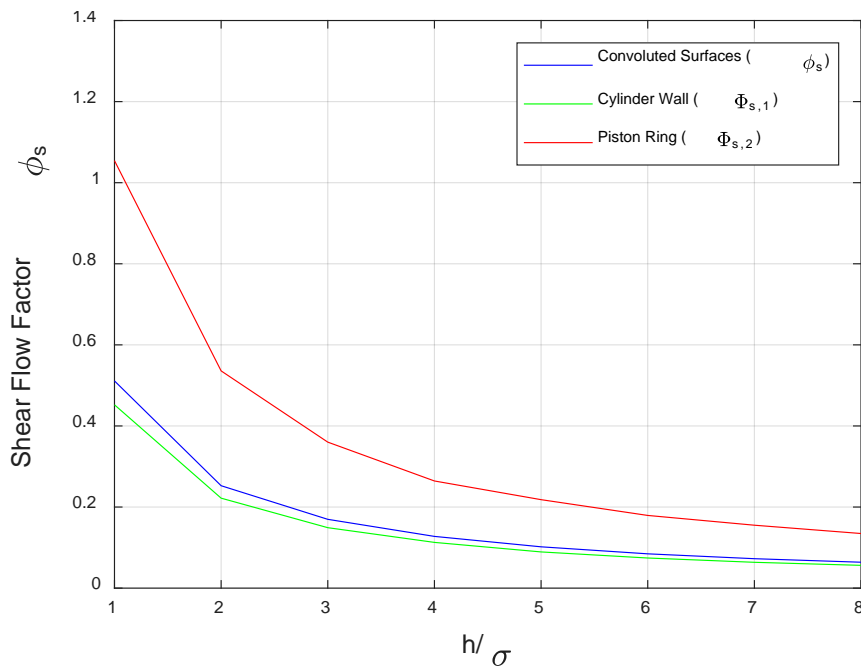


Figure 4.22: Shear flow factors

The resulting shear flow factor is also seen to vary from Patir and Cheng's [1, 40] model, shown in Figure 4.23. As the film thickness between the surfaces decreases, the engineered surfaces are seen to predict less obstruction of lubricant by surface roughness. This results in larger amounts of lubricant transported across asperities by way of shearing. In previous works, at values of  $h/\sigma$  greater than 5, several piece-wise models had to be used. With the use of a surface specific shear flow factor one continuous equation is needed.

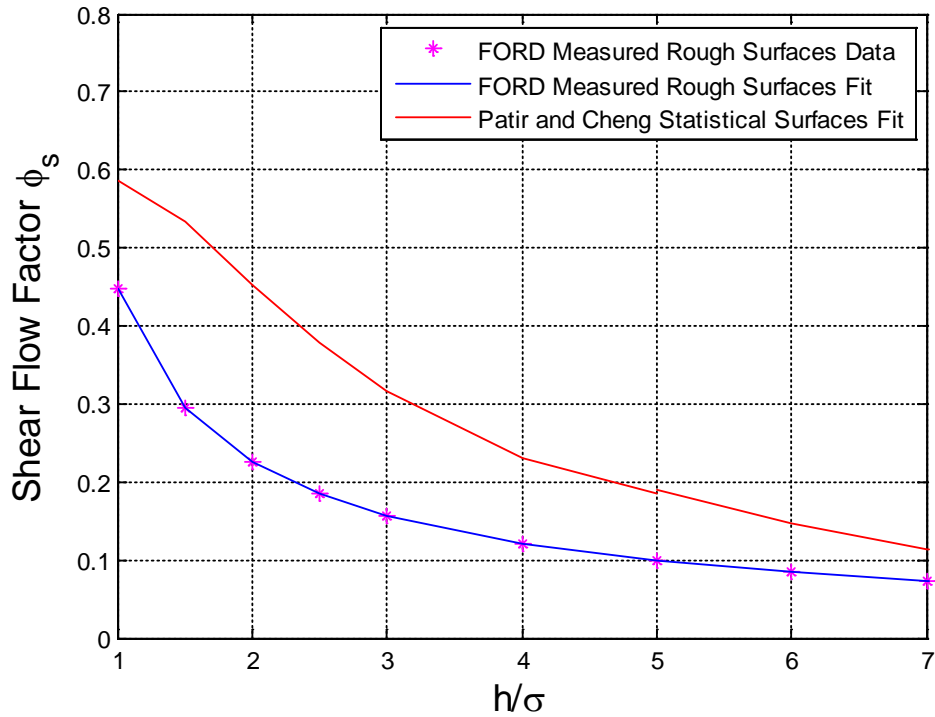


Figure 4.23: Shear flow factor comparison

The empirical equation for the shear flow factor for the convoluted surfaces is able to be fit and is given as

$$\phi_s = 0.5086(h/\sigma)^{-1.0149} + 0.0022 \quad (82)$$

The shear flow factor was attempted to be fit in the same form as Patir and Cheng's, however the solution was unstable and diverged. This is because they fit their shear flow factor using a Gaussian fit. This fit is very stable for a Gaussian surface, however in using measured surfaces this form was seen as an unstable fit. Thus, an exponential form was fit for the shear flow factor. For comparison, Patir and Cheng's empirical equations are given in the Appendix for the same Peklenik number,  $\gamma$ , of 2.79 as previously calculated. With the governing empirical flow factor equations derived, the Reynolds equation is now able to be modified to account for surface roughness features in the pressure calculations involving the cylinder wall and piston ring surfaces.

## CHAPTER 5

### PISTON RING MODEL

This chapter outlines how the various mechanisms were incorporated into the overall piston ring model. This model pairs MATLAB and ABAQUS to calculate the piston ring deformations due to various forces that are transmitted throughout the power cylinder components. The governing piston ring model includes the previously derived flow factors from the cylinder wall and piston ring interface for a lubrication model. A contact model, force and moment calculations, and their application to the piston ring-pack assembly is also discussed.

#### *5.1 Lubrication Model*

The primary focus of this model is on the piston, piston ring, and cylinder wall lubricated surface interactions. The modeling of these hydrodynamic rough surface interactions gives a better understanding of the dynamics involved and can lead to superior surfaces, surface coatings, lubricants, etc. The method chosen for modeling this lubricant flow is the method of flow factors.

Flow factors were shown as a method used to statistically model a rough surface as a smooth surface in solving a thin film lubrication problem. In previous models [1, 40] the layout of asperities was assumed to be either purely transverse, isotropic, or purely longitudinal and the flow

past and around these points were modeled with a statistically generated surface. These models were then able to be used in conjunction with the Reynolds equation for a more accurate solution which takes into account small-scale surface features. While far more accurate than modeling the hydrodynamic properties of flow across smooth surfaces, these generic flow model equations are less accurate than deriving surface specific flow factor models for predicting the fluid interactions in the hydrodynamic regime. Flow factors need to be derived for specific surfaces because generalized results are not always accurate for a specific surface. Thus more precise flow modeling equations are necessary for more accurate flow predictions and computational efficiency.

Three flow factors are paired with the Reynolds equation to account for surface impedance on the flow of a lubricant. The first of these,  $\varphi_z$ , measures the flow resistance across asperities due to a pressure induced gradient along the flow direction. Similarly,  $\varphi_x$  measures the flow resistance along the transverse direction. Lastly,  $\varphi_s$  measures the lubricant transport due to shearing effects. These flow parameters are a function of the film thickness, standard deviation of the surfaces (i.e. RMS surface roughness), and the Peklenik number ( $\gamma$ ) as defined by the auto-correlation function derived from the specific surface topography [2].

A rough surface profile of the cylinder wall from the current production internal combustion engine was shown in Figure 3.2. In dealing with surface specific flow factors, only the small-scale surface features are needed while the Reynolds equation handles the large scale geometry. Therefore, the curvature of the piston ring is subtracted out, resulting in a nominally flat surface with the same small-scale surface features. The piston ring without curvature can be seen in Figure 3.7. The interaction of the cylinder wall and the piston ring is seen in Figure 4.3.

Using the cylinder wall and nominally flat piston ring surfaces several cases were run, as outlined in Sections 4.3 and 4.4. These results were plotted against film thickness and the results are seen in Figures 4.18 and 4.21 for the  $x$  and  $z$  direction pressure flow factors respectively. For comparison, Patir and Cheng's curves are plotted for the same Peklenik number. Similarly the shear flow factor is calculated by applying a sliding velocity at various film thicknesses. The results for each case are plotted in Figure 4.22. With these three curves empirical relationships were fit and described as the governing flow factor equations for this set of specific surfaces. The three equations are shown below.

$$\varphi_x = 2.4827(h/\sigma)^{-1.6955} + 0.9752 \quad (83)$$

$$\varphi_z = 1 - 0.4824e^{-0.2477(h/\sigma)} \quad (84)$$

$$\varphi_s = 0.5086(h/\sigma)^{-1.0149} + 0.0022 \quad (85)$$

By employing these equations, the Reynolds equation (Eq. (32)) is able to be modified to account for surface roughness.

With this surface specific flow factor derivation method, the three piston rings on the piston and each of their respective housings could also be modeled as rough surfaces and account for surface asperities. This model would still be able to run at a computational time equivalent to modeling the surfaces as smooth, while still considering the roughness of the surfaces. The modeling of multiple piston rings considering surface roughness is, however, beyond the scope of this current ring model.

## 5.2 Solid Contact Model

The following solid contact model was derived by Nolan Chu [66], who is a partner on this piston ring model project for Ford Motor Company. To represent the contact mechanics model, three different rough surface contact models were considered.

The first model, the Greenwood-Williamson statistical model [67], assumes a Gaussian distribution of spherical asperities. From the surface profile, the asperity density,  $\eta$ , the asperity radius,  $R_{ah}$ , and the asperity height roughness,  $\sigma_s$ , were calculated in two different directions. However, it was found that the distribution of surface heights in one of the directions for the cylinder wall had a highly non-Gaussian distribution. The use of the statistical parameters directly from that direction ( $z$ ) rendered the Greenwood and Williamson model ineffective. Thus, two sets of parameters were evaluated: those based on the heights in the  $x$  direction, and those based on the averaging of parameters found independently in both directions.

The second model considered was the full multiscale model [68]. In this model the asperities were assumed to be sinusoidal in shape. The surface profile was transformed into the frequency domain, and a one dimensional equivalency was obtained. On each scale level, the force was assumed to be applied equally to all asperities. This model considered both elastic and elastic-plastic deformation as well, but does not depend on the surface being Gaussian.

The third model applied sinusoidal asperities to the Greenwood-Williamson statistical model. As the surface separation must be known, results from a finite element model were adapted [69]. Both elastic and elastic-plastic deformation were considered as well.

All three models were applied to the combined surfaces. The variables  $\eta$ ,  $R_{ah}$ , and  $\sigma_s$  were calculated in a similar manner. There were no problems with the distribution of surface heights, and three sets of parameters were evaluated: those based on the heights in the  $x$  direction, those based on the heights in the  $z$  direction, and those based on the averaging of parameters found independently in both directions. Both the wall and the piston ring were assumed to have identical material properties.

Figure 5.1 shows the normalized load as a function of normalized surface separation. The three different types of models are represented: the statistical model using spherical asperities, the statistical model using sinusoidal asperities, and the multiscale model.

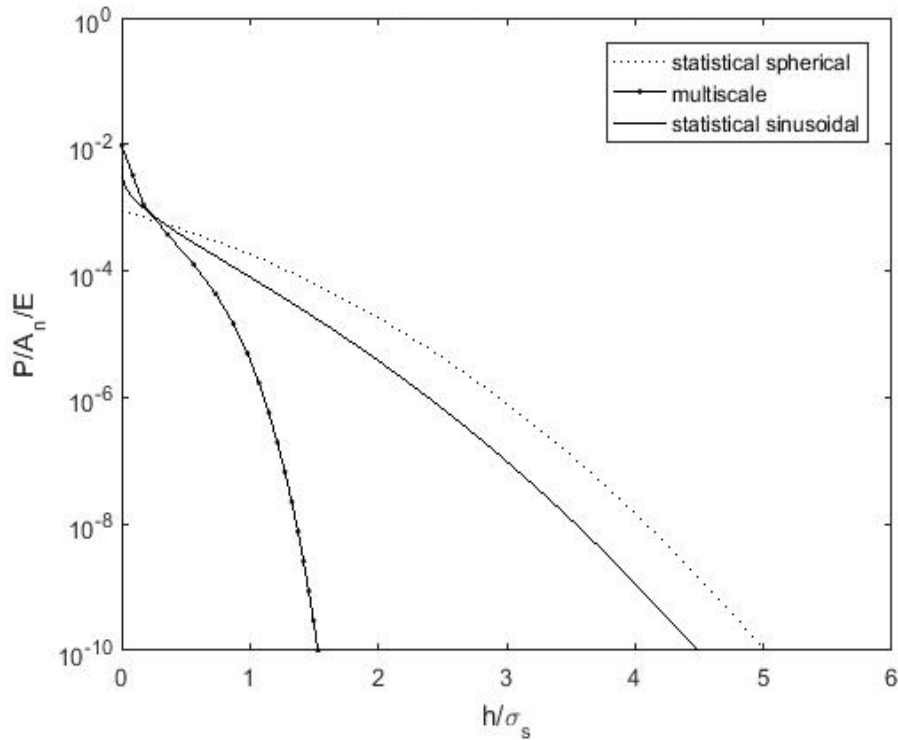


Figure 5.1: Elastic-Plastic contact pressure for the combined surfaces

As seen in Figure 5.1, pressure decreases as the surface separation grows and as they come out of contact. As the multiscale model predicts a much different relation, the more established statistical model will be used in the piston-cylinder model to consider solid contact between the cylinder wall and piston ring. This solid contact effects the orientation of the piston ring in the groove as the piston traverses in a linear fashion from TDC to BDC. This in turn effects the amount of lubricant distributed across the bore of the cylinder, which has a large effect on component performance, efficiency, and longevity.

### *5.3 Coupled Lubrication and Solid Contact Model*

To model the cylinder wall and piston ring interface the coupled effect of the lubricant hydrodynamic pressure and the rough surface contact pressure must be considered. These pressures are predicted by the models in Sections 5.1 and 5.2, respectively. The hydrodynamic pressure and rough surface contact pressure are then superimposed to find their net effect on the ring, the cylinder, and the piston through

$$P_{Total} = P_{Hydrodynamic} + P_{Contact} \quad (86)$$

The hydrodynamic and contact pressures are superimposed on each side of the piston ring. With the pressures acting through a known area of the piston ring, the net forces on the ring may be calculated.

### *5.3.1 Coupled Model Test Cases*

Before the forces on all sides of the ring are calculated, several test cases are run to verify the coupled lubrication solid contact model. The first test case is run at a larger film thickness to demonstrate the accuracy of the hydrodynamic model. The second test case was run at a much smaller film thicknesses that brings the surfaces into contact. This will demonstrate the accuracy of the rough surface contact model. The test cases are run for a one-dimensional slider bearing (Figure 3.21), which is meant to simulate the cylinder wall and piston ring interactions. The nodal discretization can be seen in Figure 3.22. The upper surface is treated as the axial width of the piston ring, and the lower surface is treated as the cylinder wall. The axial width of the piston ring is modeled as a converging diverging gap; the system parameters for this test case are given in Table 5.1.

Table 5.1: Coupled model test case 1 parameters

Parameter	Variable	Value	Units
Axial width of piston ring	$a$	1.2	$mm$
Radial width of piston ring	$r$	2.9	$mm$
Dynamic viscosity	$\mu$	0.1	$Pa \cdot s$
Relative velocity	$u$	9	$m/s$
Length of bearing	$L$	0.0012	$m$
Height at inlet of incline	$h_1$	$8 \times 10^{-6}$	$m$
Height at outlet of incline	$h_2$	$7 \times 10^{-6}$	$m$
Crankcase pressure	$p_1$	101	kPa
Chamber pressure	$p_2$	1500	kPa

The relative velocity of  $9 \text{ m/s}$  was chosen to match the typical Mean Piston Speed (MPS) for this engine's application. The predicted pressure due to the hydrodynamic and rough surface interactions is given in Figure 5.2.

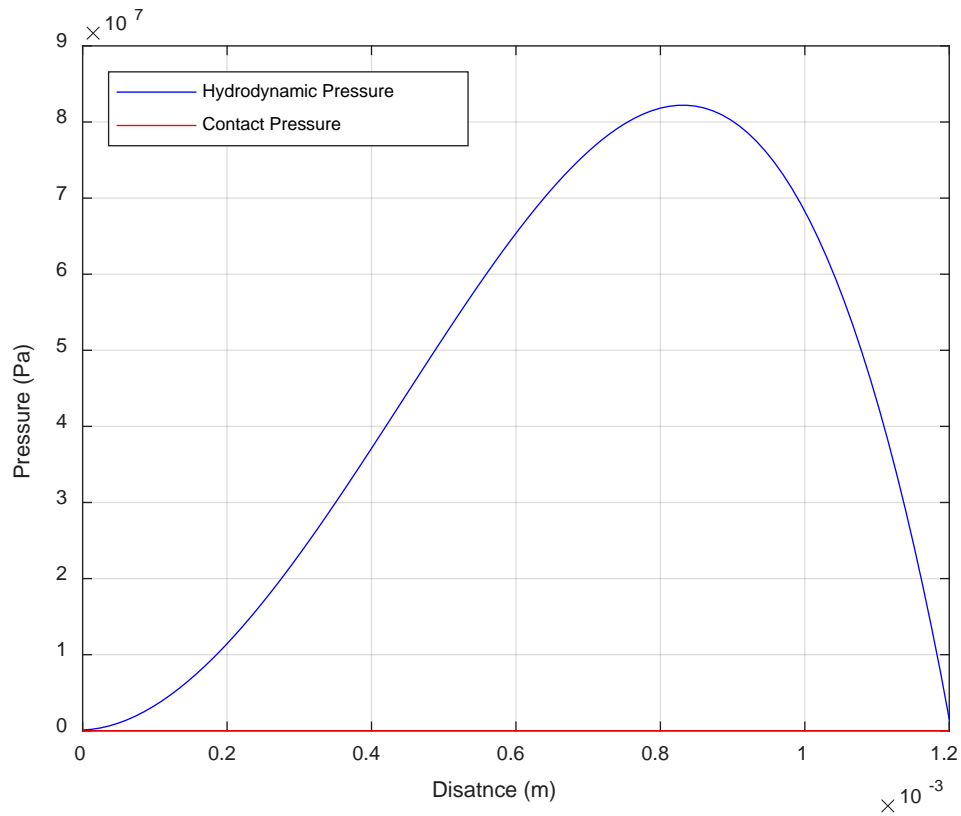


Figure 5.2: Total pressure acting on outer piston ring surface

As expected with these inlet ( $h_1$ ) and outlet ( $h_2$ ) gaps, the pressure is seen to be only hydrodynamic. As the film thickness gets larger, and the surfaces move further apart, the contact model is weighted less and the hydrodynamic model is weighted heavier.

The second case was run with the exact same parameters, except the inlet and outlet gaps are decreased to  $h_1 = 1\mu m$  and  $h_2 = 0.5\mu m$ , respectively. With this decrease in film thickness, the pressure profile across the piston ring and cylinder wall become Figure 5.3.

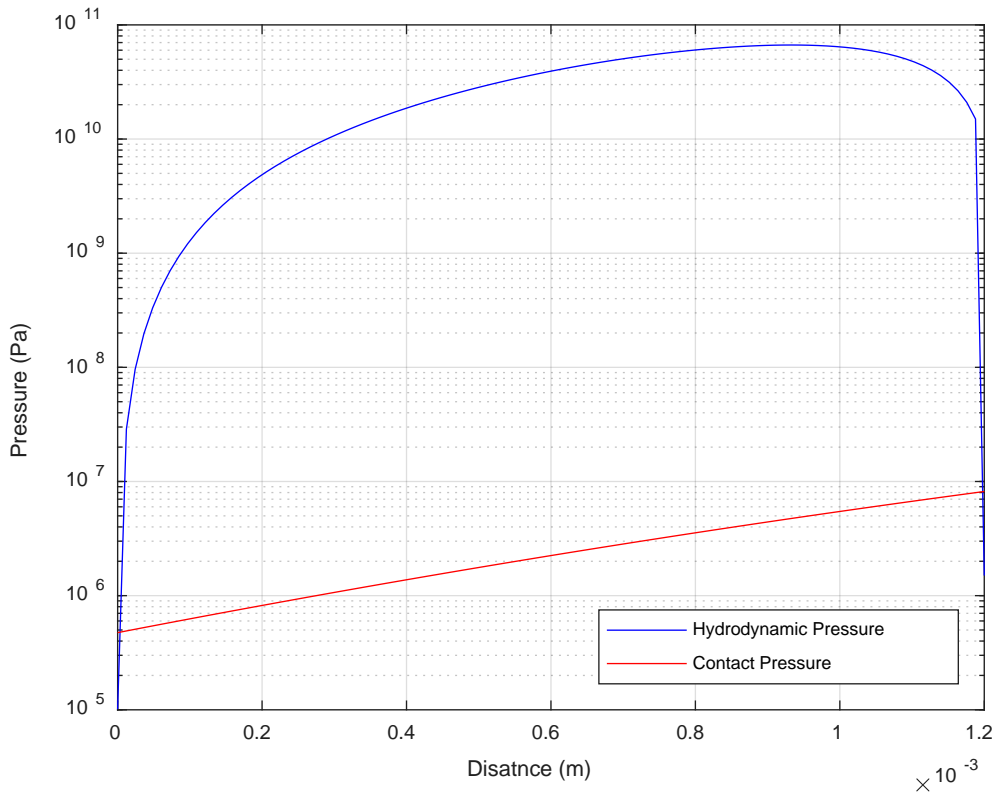


Figure 5.3: Pressure acting on outer piston ring surface

As expected, the contact pressure is largely increased as the film thickness decreased such that the surfaces came into contact. Interestingly, the hydrodynamic pressure also increased. This is due to the implementation of the flow factors, simultaneously in the absence of a piston ring deformation model. This will change upon integration of the ring deformation model.

The combined lubrication and contact model has been demonstrated for the cylinder wall, piston ring interface with macroscale deformations neglected. This same methodology of applying the hydrodynamic pressures and contact pressures is now expanded to each side of the piston ring.

#### 5.4 Finite Element Ring Model

This section demonstrates the ability to use the pressures from the lubrication and solid contact models in a finite element model of the ring to then calculate the ring deformations. The ring pressures due to the lubrication and contact models are calculated in MATLAB and sent to ABAQUS, where the ring deformations are calculated and the data is sent back to MATLAB.

A simple finite element model of an axisymmetric ring was implemented in ABAQUS to demonstrate this. The axisymmetric ring was meshed, as seen in Figure 5.4, then forces and boundary conditions were applied to it. The analysis was run to generate an .inp file, which could be written exclusively within MATLAB so the fluid and contact pressures could be applied. Using the toolbox `abaqus2matlab`, displacements can then be calculated for the piston ring analysis in ABAQUS and extracted then plotted in MATLAB.

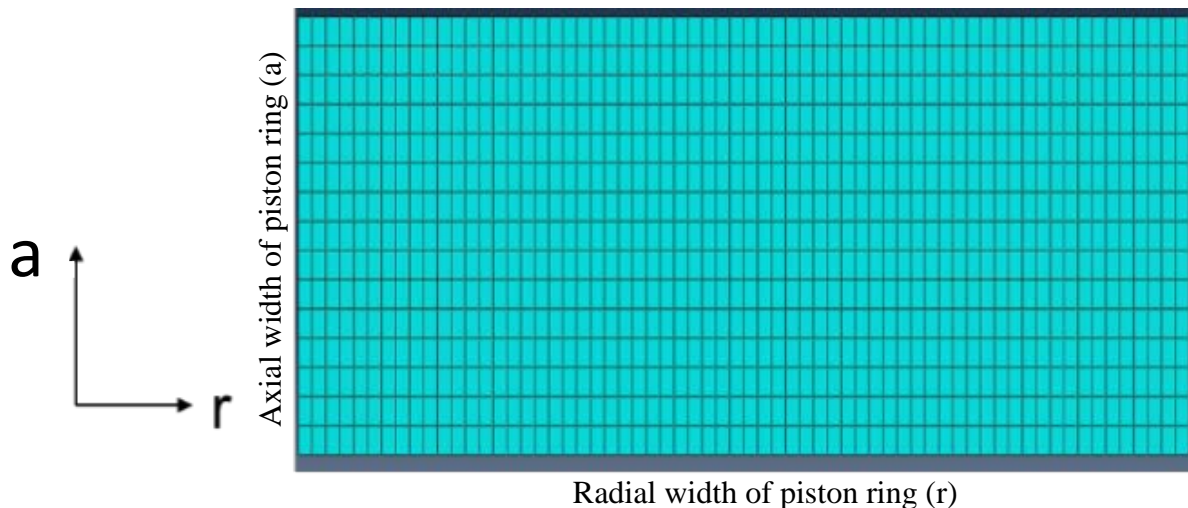


Figure 5.4: Sample ABAQUS mesh

### *5.5 Boundary Conditions*

The lubricant flow around the ring is broken up into six different sections to account for the various conditions each part of the ring experiences, as seen in Figure 5.5. Each sections' boundary conditions are assumed to have a pressure applied, consisting of a hydrodynamic pressure and a solid contact pressure. Also specified along each piston ring surface is the relative velocity of the lubricant, used for the hydrodynamic pressure calculations.

Section 1 of the piston ring (Figure 5.5) is assumed to experience the pressure from the combustion chamber. The relative sliding velocity of the lubricant on the surface is assumed to be zero.

In a similar manner, Section 5 is assumed to experience the pressure from the crankcase with a relative lubricant sliding velocity of zero as well.

As the pressure in the combustion chamber is larger than the crankcase pressure, which is at atmospheric, there is assumed to be a linear decreasing pressure gradient from Sections 2 through 4. This linear decreasing pressure gradient forces lubricant to flow from the combustion chamber (higher pressure) to the crankcase (lower pressure) around the groove housing. The relative fluid velocity around these three sections is also assumed to be zero. While the fluid shearing velocity is assumed to be zero, there are still minimal amounts of lubricant that leak past the ring through the groove housing due to the pressure gradient. These leakage rates can be calculated.

Lastly, at section 6 is the piston ring, cylinder wall interface. The pressures here are due to hydrodynamic and contact interactions, as well as the boundary pressures. There also exists a large sliding velocity between these two surfaces. More is discussed in Appendix B.

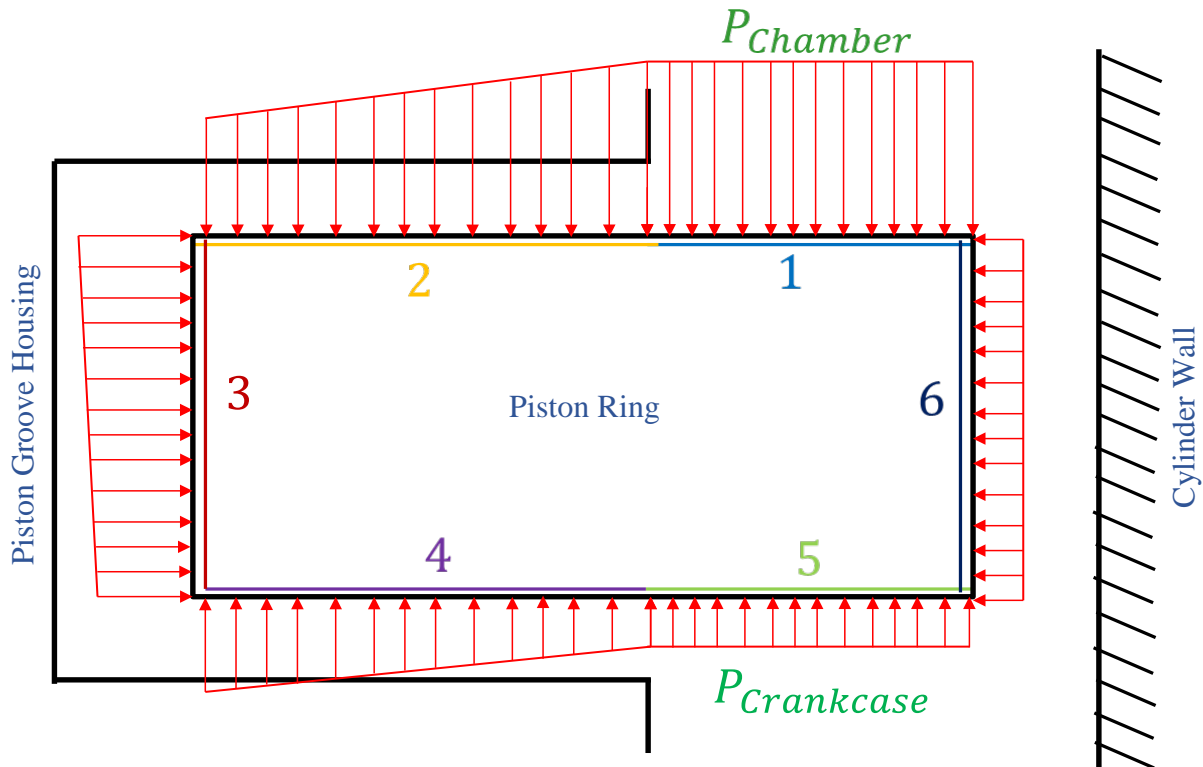


Figure 5.5: Free Body Diagram of piston, piston ring, and cylinder wall interface with boundary condition breakdowns

### 5.6 Force and Moment Balance

To find a pseudo-steady state solution, the position of the ring relative to the piston groove is adjusted until all the forces on the ring balance. Figure 2.5 shows the motion of the piston ring in the groove housing. The pressure at each node is calculated by superimposing hydrodynamic

and solid contact pressures over the area at each node. The force is then found by integrating over the entire surface. The force at node  $(i,j)$  is expressed as

$$F_{total} = \int_{A_{i,j}} p_{hydrodynamic} dA_{i,j} + \int_{A_{m,n}} p_{contact} dA_{i,j} \quad (87)$$

The pseudo-steady state position of the piston ring has been reached when the forces and moments sum to zero. Taking the center of mass of the piston ring to be the point where the moments are summed about gives

$$(F_{total})_x = \sum F_i = 0 \quad (88)$$

$$(F_{total})_z = \sum F_j = 0 \quad (89)$$

$$M_{CM} = \sum F_i \cdot z - \sum F_j \cdot x = 0 \quad (90)$$

The piston ring with the applied forces due to lubrication, contact, shearing, and the combustion cycle are drawn in the free-body diagram depicted in Figure 5.5. The pressure is also used to calculate the deformed shape of the ring, which will in turn affect the surface separation between the parts, which govern the hydrodynamic and contact pressures. Therefore the models are coupled together and must be solved iteratively; this iterative process is examined in more detail in Section 5.7.

It should be noted that the surface specific derived flow factors only accurately model the surface topography on the outer piston ring interface with the cylinder wall. For flow models involving rough surfaces on any other side of the piston ring, additional surface data must be acquired. This includes the flow around the piston ring through the piston groove housing (seen in

Figure 5.7). Accurate flow models are still applied, however the effect of those specific surface roughnesses is not taken into account. Instead the flow factors derived from the piston ring – cylinder wall interface are used to model the flow past those surfaces topography. While not specific to that respective face of the piston ring, the use of flow factors still improves the accuracy of the average flow model to include roughness.

### 5.7 Convergence

The previously outlined methods are combined together through their boundary conditions. The piston ring model must be solved iteratively in order to reach a specified tolerance with the converged solution. The Newton-Raphson method is used to solve the coupled nonlinear force and moment equations on the piston ring (Eqs. (88-90)). The Newton-Raphson method is used in numerical analysis for finding successively better approximations of the root of a function. This allows to find the steady-state position of the ring where the forces and moments sum to zero. Newton’s method is outlined as

$$x_{n+1} = x_n - \frac{f(x_n)}{f'(x_n)} \quad (91)$$

Due to the fact that the derivative of these functions is not an analytical expression, the centered finite difference method must be used to discretize the derivative. Using centered finite difference, Newton’s method becomes

$$x_{n+1} = x_n - \frac{f(x_n)}{\frac{f(x_{n+1}) - f(x_{n-1}))}{x_{(n+1)} - x_{(n-1)}} \quad (92)$$

where the function,  $f$ , is the sum of the unbalanced forces and  $x$  is the height of the center of mass of the ring inside the groove housing to achieve the steady-state position. The flow chart for the governing piston ring model is shown in Figure 5.6. Several models have not yet been implemented, however significant progress has been made on them. Several included are the temperature model, viscosity model, and a dynamic model which are discussed in greater detail in Appendix B.

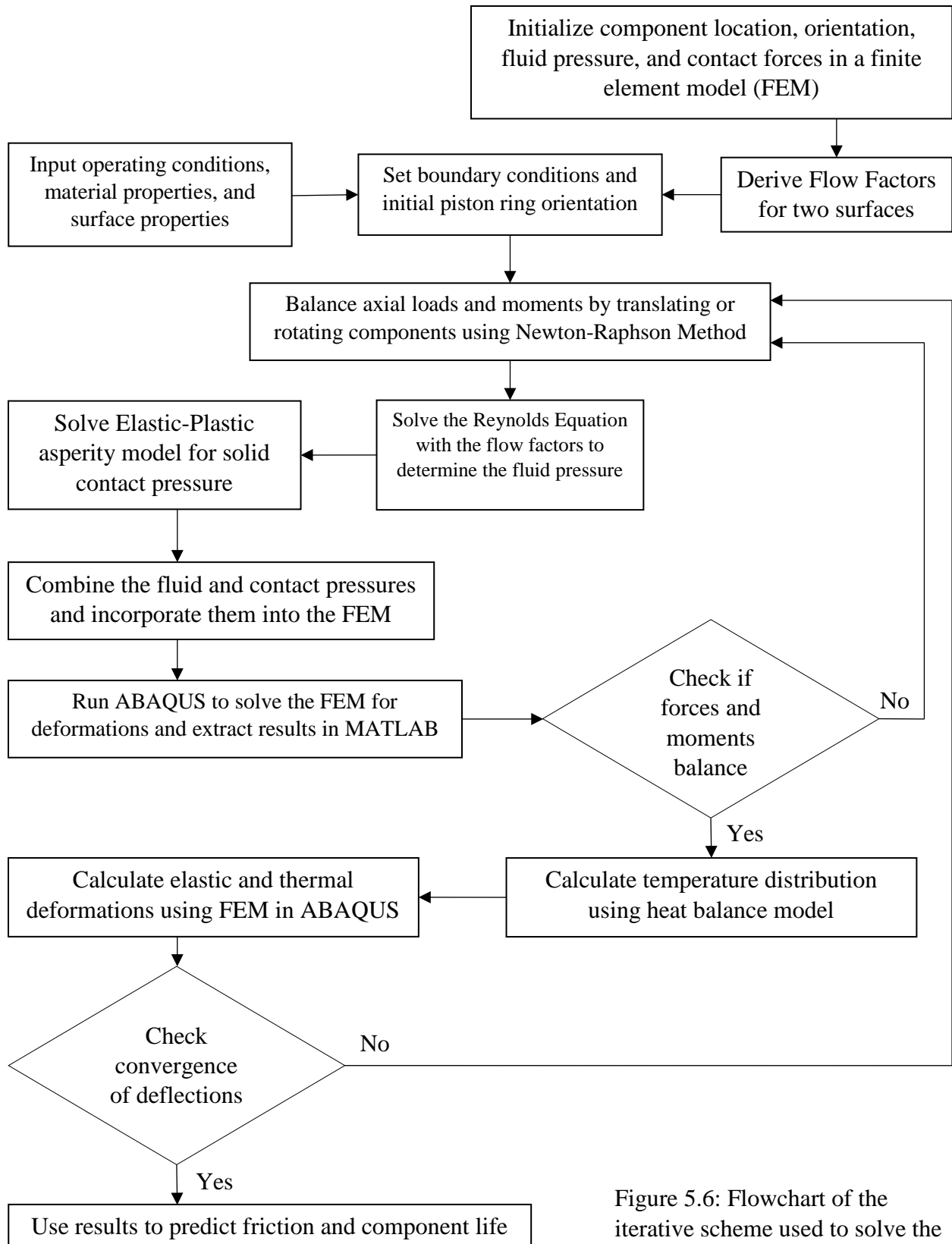


Figure 5.6: Flowchart of the iterative scheme used to solve the coupled contact and lubrication problem

### *5.8 Piston Ring Model Results*

The numerical results from the combined and fully coupled model is able to give the superimposed hydrodynamic and contact pressures on all sides of the piston ring. These results can then be implemented in the design and optimization of various coatings and materials for the cylinder wall or the piston ring. Along with coatings, the geometry of the piston ring can also be optimized in terms of leakage past the piston ring by way of the piston ring groove housing. For example, some piston rings have rounded edges to allow for smoother pressure transition regions, as well as hydrodynamic lift even for a diverging gap. At the corner of each surface of the ring the pressures are larger as there is seen to be a discontinuity. This causes the mechanical instability and stress to greatly build up over the cyclic nature of the piston. The following case was run in accordance with the parameters from Table 5.1.

Recall from Figure 5.5 that the piston ring was broken down into six different sections to solve for the pressures acting on each surface. Figure 5.7 shows the orientation of the piston ring at a  $10^\circ$  angle from its horizontal position. The flow is forced to move past the piston ring from north to south while the piston ring orientation remains fixed. This is to demonstrate the lift on the surfaces. Future models will be implemented where the piston ring tilts as the piston moves in a rectilinear fashion.

The piston ring is assumed to be at its maximum piston speed of  $9m/s$  halfway in between TDC and BDC. The outer wall interface with the cylinder wall is observed to be the same geometry as the slider bearing in Section 3.3.3, therefore the pressure profile is observed to be similar (Figure 5.8).

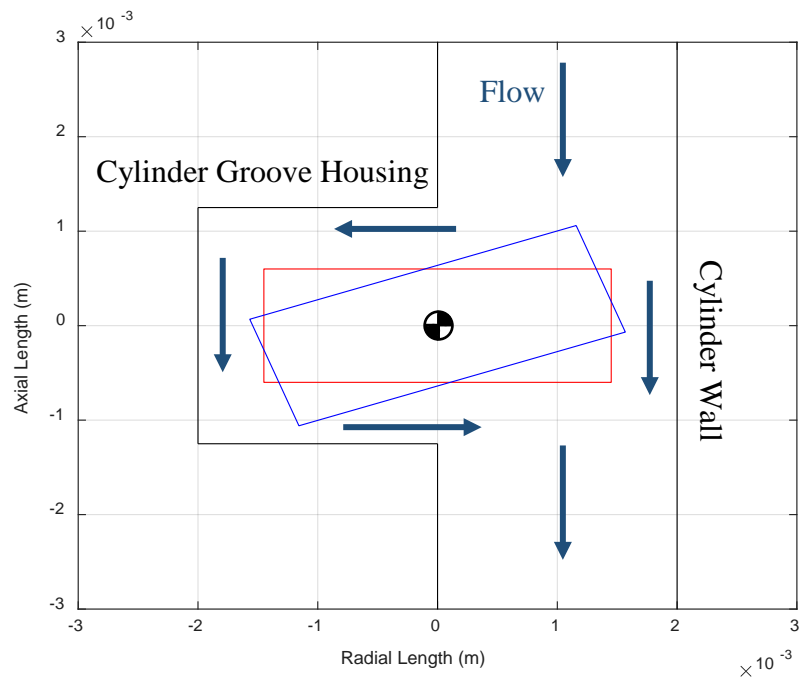


Figure 5.7: Piston ring rotation about the Center of Mass

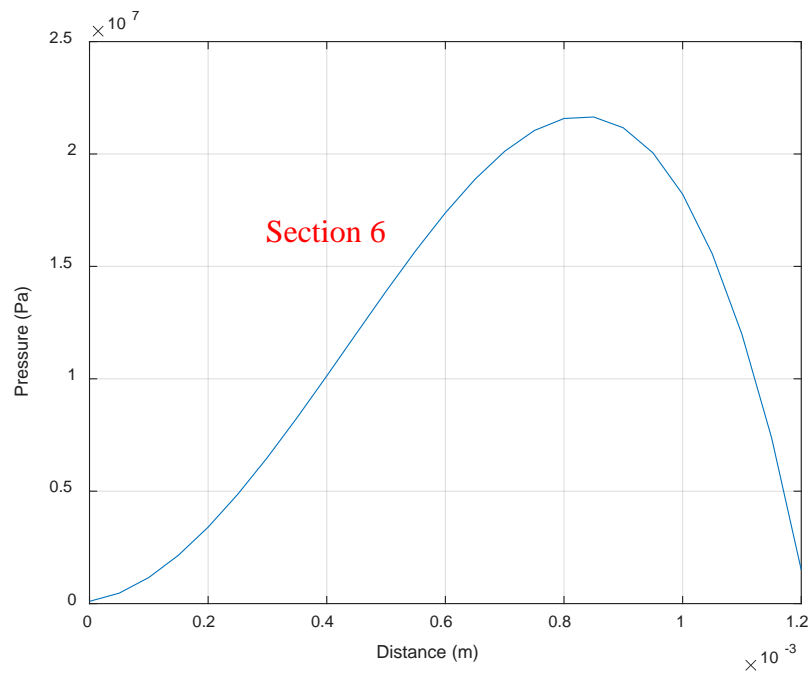


Figure 5.8: Pressure on outer ring surface

As previously mentioned, there is an assumed linear decreasing pressure gradient from the combustion chamber to the crankcase around the piston ring through the groove housing. In Figure 5.9 the pressure gradient is shown for the upper surface. The sections of the piston ring are labeled. As expected, section 1 is seen to be at the same pressure as the combustion chamber. The geometry for section 2, as seen in Figure 5.7, is seen to be the opposite of the slider bearing geometry, and is a diverging wedge shape instead of a converging wedge shape. This results in a pressure drop across the upper surface. As previously mentioned, it can also be noticed from Figure 5.9, that there is a sudden drop in pressure at the corner of the surface. Two pressure profiles are affecting this section of the upper surface and result in the sudden decrease. The first are the boundary conditions that are governed by the linear decreasing pressure from the combustion chamber to the crankcase. The second are the pressures generated due to the reverse wedged shape of the upper surface from hydrodynamic and contact forces. This results in the pressure curve shown for the entire upper surface of the piston ring.

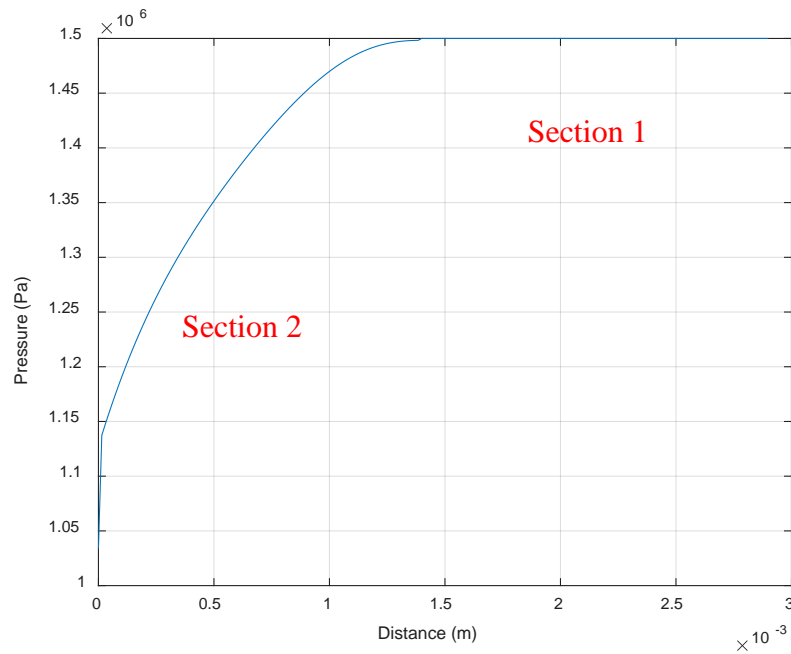


Figure 5.9: Pressure on upper ring surface

The inner surface of the piston ring is also seen to be a diverging gap in the direction of lubricant flow, as seen in Figure 5.7. Similar to the upper piston ring surface, there are two pressure profiles that effect the net pressure acting on the inner piston ring surface, as seen in Figure 5.10. The firstly being the linear decrease in pressure from the combustion chamber to the crankcase. The second is from the reverse wedge shape of the piston ring that affect the hydrodynamic and contact forces. Both of these result in a net decrease in pressure across the inner surface.

The pressure profile for the lower piston ring surface is seen in Figure 5.11. Similar to the upper surface, it can be seen that at section five, the crankcase pressure is constant across that part of the piston ring. Across section four is the same decreasing pressure gradient and diverging wedge slider bearing shape.

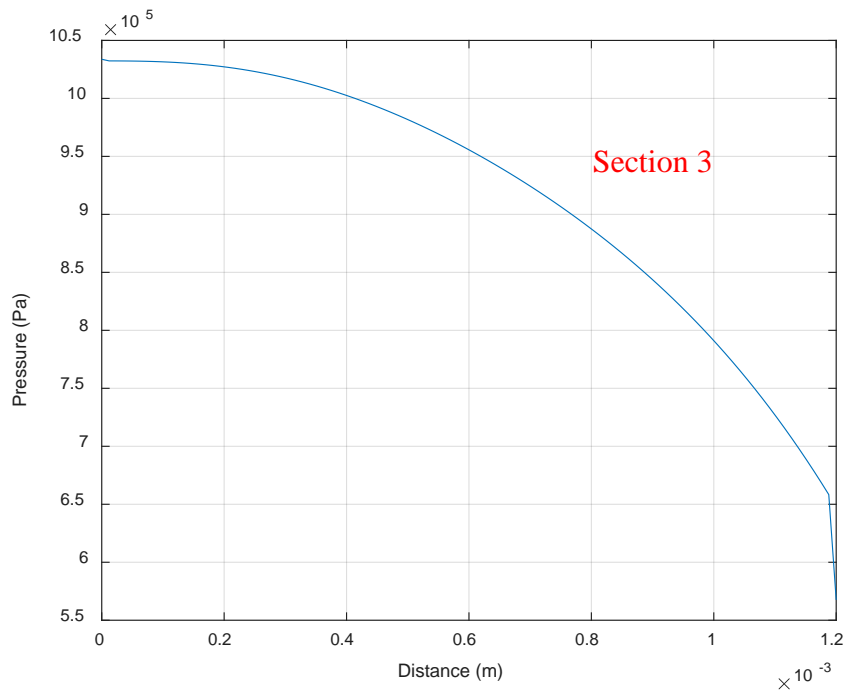


Figure 5.10: Pressure on inner ring surface

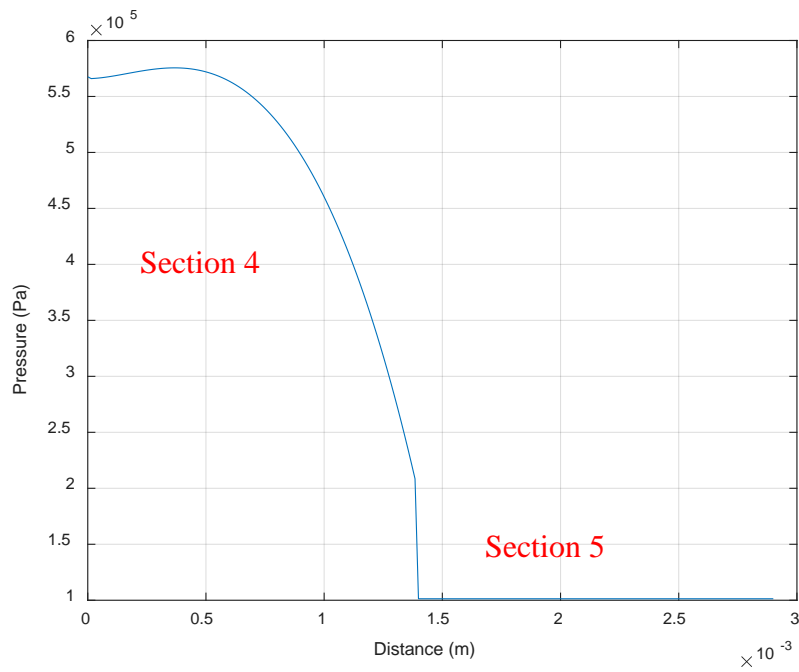


Figure 5.11: Pressure on lower ring surface

Figure 5.12 shows the pressure change across all 6 sections of the piston ring, in accordance with the test case parameters of Table 5.1. The pressure is seen to be the largest on the outer piston ring surface (section 6). To show the pressure profiles of each section in greater detail, the film thickness is increased to  $h_1 = 0.1mm$  and  $h_2 = 0.2mm$ . This can be seen in Figure 5.13. Also the linear decreasing pressure through the piston groove housing can be seen. At each of the sections around the ring in the piston groove housing (sections 2, 3, and 4), diverging surface geometry is observed and hence no lift is generated.

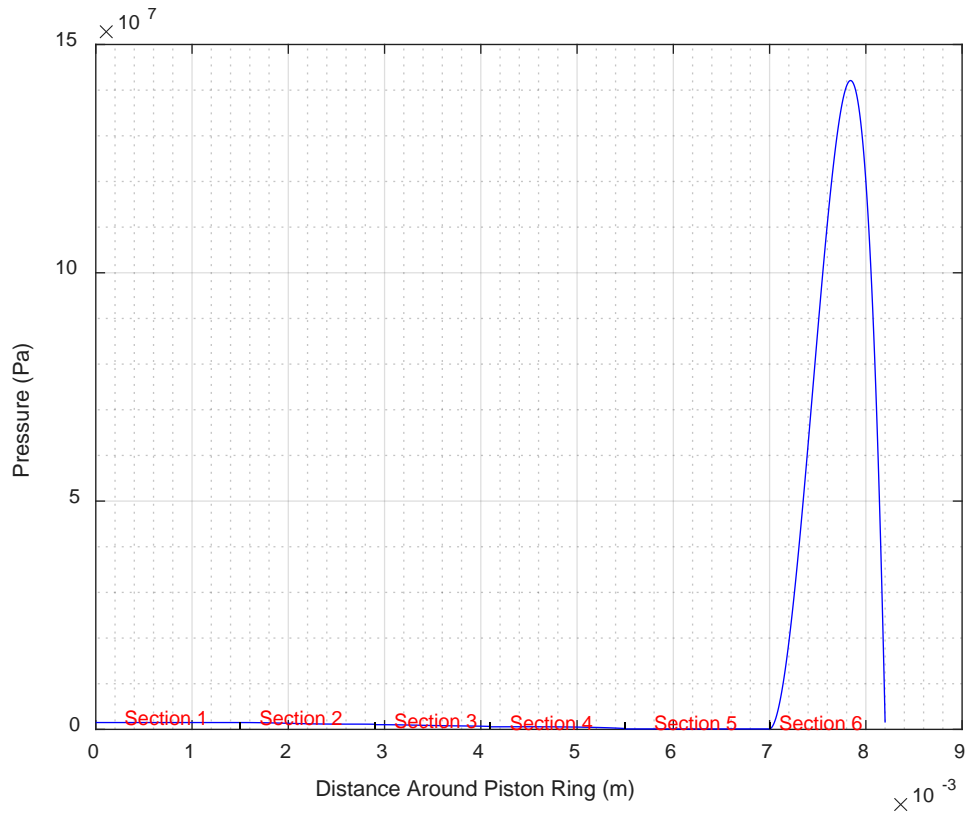


Figure 5.12: Total pressure on piston ring surfaces (smaller film thickness)

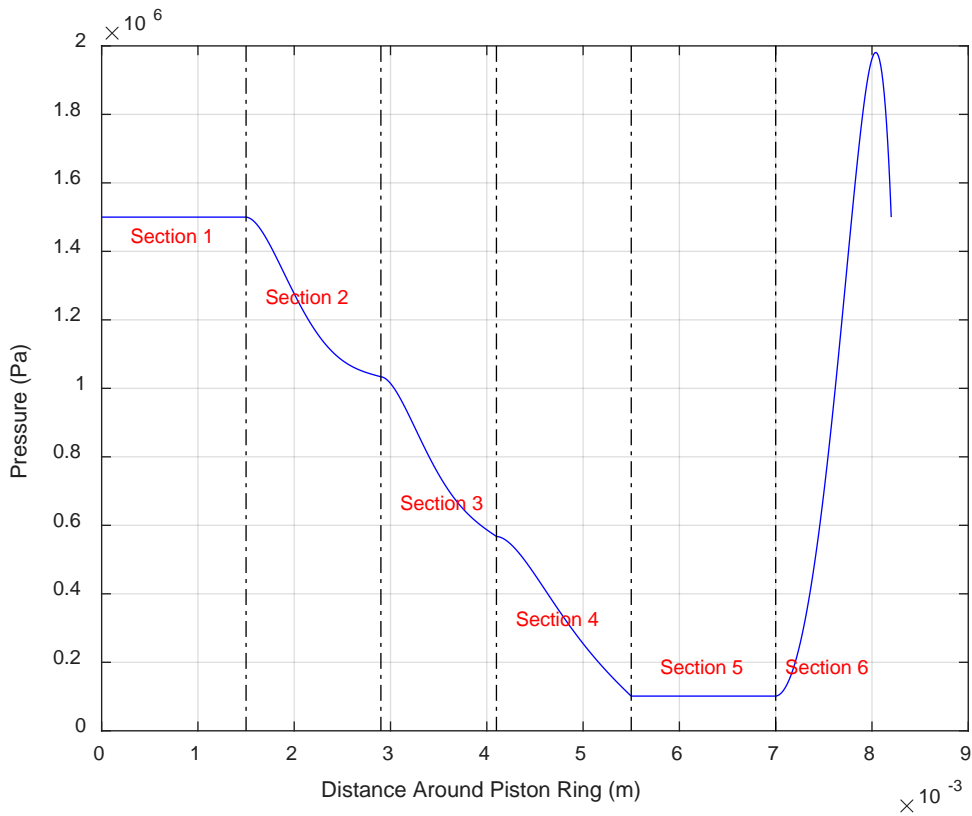


Figure 5.13: Total pressure on piston ring surfaces (larger film thickness)

With the pressures calculated on each side of the ring, the deformations of the ring are calculated in ABAQUS and are iterated through MATLAB. The deformations for the piston ring due to mechanical interactions are seen in Figure 5.14. The y-displacement represents the axial height displacement of the upper surface on the piston ring.

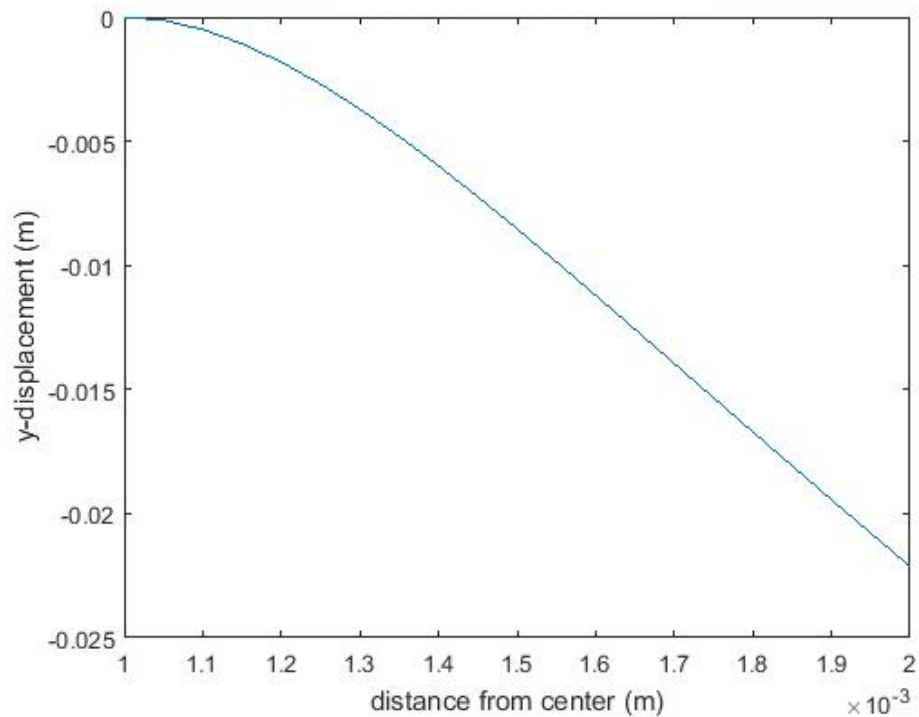


Figure 5.14: Output deformation results in MATLAB

It can be seen that at distances further from the center of the piston ring, the deformations become more exaggerated. This is attributed to the points that see the initial stresses and pressures generated on the surfaces, as governed by the boundary conditions. Also, as seen, this can be attributed to the larger pressures at each corner of the piston ring. Therefore it can be designed that the piston ring corners should be rounded. Ford has taken this into account and their piston rings are designed such to eliminate these abnormally higher pressures at the corners. Figure 5.15 shows a cross sectional schematic of a piston ring from one of their internal combustion engines. The inner corners are noticed to be rounded to eliminate any abnormal discontinuous pressures. Also

it is noticed that a coating has been applied in the spray filled groove. This is to improve the tribological interactions the piston ring makes with the cylinder wall.

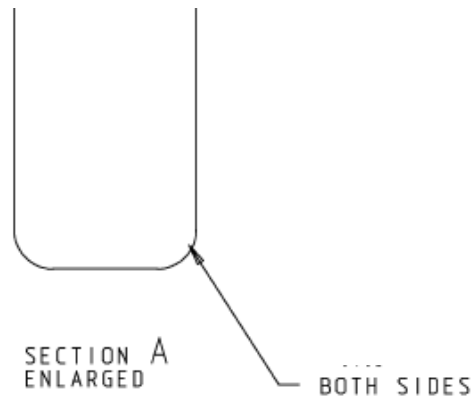


Figure 5.15: Ford piston ring with rounded edges

### *5.9 Future Model Implementations*

There are several other modules that have made smaller advancements since the initiation of this project, however have not yet been integrated into the whole piston ring model. Those can be found in Appendix B. This section goes into detail about the implementation of a dynamic model that is also forthcoming on this project, and its effect it will have on the entirety of the piston ring model.

### 5.9.1 Dynamic Model

Currently, the piston ring model assumes a constant velocity of the piston throughout the cycle in order to calculate the forces on the piston ring. In practice, the piston's Mean Piston Speed (MPS) varies from 0 to  $25\text{m/s}$  for all internal combustion engines. Among average automotive engines, the value of MPS will reach  $12\text{m/s}$ . For racing vehicle engines this value is higher.

A dynamic velocity model was implemented for the test case of a slider bearing. This simulation is nearly identical to the 2-D simulation in Section 3.3.3. The only difference is that the velocity of the bearing is not constant. The current piston speed model is taken from a racing engine which results in larger piston speeds. The piston speed model can be seen in Figure 5.16.

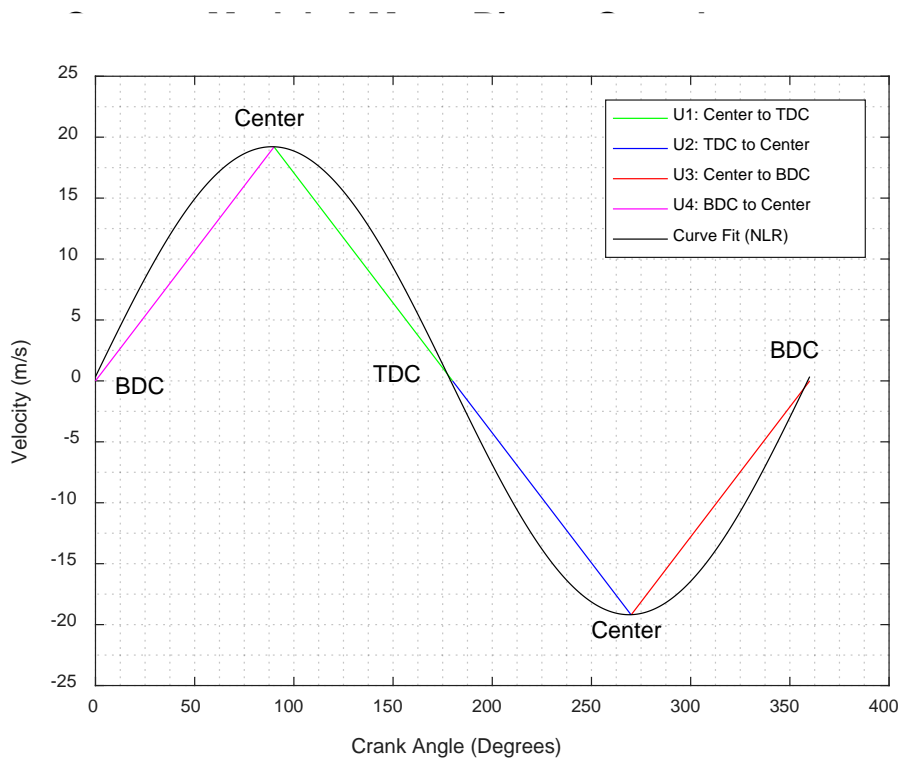


Figure 5.16: Modeled piston speed for slider bearing

As the piston traverses the bore, the head starts at rest at TDC. It accelerates to its maximum piston velocity half way down the chamber at the center. Followed by a gradual deceleration from at its maximum piston velocity at the center of the bore to rest at BDC. This piston cycle continues throughout operation and can be seen in Figure 5.16.

In practice the piston velocity is modeled as a sinusoidal curve governed by the velocity equation

$$\dot{x} = \frac{dx}{dt} = v = -r \left( \sin \theta + \frac{\sin 2\theta}{2\sqrt{\left(\frac{l}{r}\right)^2 - \sin^2 \theta}} \right) \quad (93)$$

where  $l$  is the connecting rod length,  $r$  is the crankshaft radius, and  $\theta$  is the crankshaft angle. This practical modeled equation can be seen in Figure 5.16. In working towards a sinusoidal piston speed model, a linear velocity model is first implemented. The stroke of the piston cycle is broken into four parts, each with a different linear velocity gradient. The velocity sections are broken down as follows:

1. Center to TDC
2. TDC to Center
3. Center to BDC
4. BDC to Center

In applying these velocity profiles to the modeled slider bearing, the pressures are able to be calculated at each location in the bore due to the nature of the converging gap geometry of the sliding piston ring. This dynamic piston model will be incorporated into the entire piston ring model in the future.

## CHAPTER 6

### CLOSURE

#### *6.1 Conclusions*

Surface topography was seen to play a large role in not only power cylinder component longevity, but also more importantly efficiency and performance. In the past hydrodynamic lubrication models, stochastic theory, along with random process analysis, all have been used to predict the flow of lubricant across rough surfaces. The direct asperity interactions within the fluid flow varies from surface to surface. The research presented in this thesis sought to modify existing theories that govern flow over general surfaces, to a more accurate model of flow over specific surface topography, namely power cylinder surfaces. For this very reason the governing lubricant flow equation, the Reynolds equation, was able to be modified by the use of pressure and shear flow factors.

An updated method of deriving surface specific flow factors uses the average Reynolds equation to calculate specialized pressure and shear flow factors, which are able to predict surface specific roughness effects in the hydrodynamic lubrication regime. While numerical iterations are required, the method of flow factors is computationally more efficient for accurate flow model predictions. The empirical flow factor models are used in conjunction with the Reynolds equation

for any Gaussian or non-Gaussian surface. This method of deriving surface specific empirical flow models has minimal limitations among the application of engineered surfaces throughout a multitude of fields considering tribological interactions, and is able to be used confidently and more accurately in the analysis of any surface interaction.

## *6.2 Future Work*

This work found the importance of surface texturing among power cylinder components. Surface texturing provides a foundation for component efficiency and performance. Therefore, the presence of a coating on the surface should also be considered. This can be accomplished using three possible methods, depending on the thickness of the coating. For coatings that are thinner than the scale of the roughness, the coating will be considered at the asperity scale. For instance, models are available to predict initial yield and possible failure of coated asperities [70-73]. Second, by using a hierarchal multiscale model a coating can be considered by changing the properties of the material at the different scales in the model (see these works by Jackson: [11, 14, 74, 75]). Third, the coating could be considered deterministically as necessary (where it is modeled in the macroscale FEM model as in [11]). This also considers the failure initiated due to thermal expansion mismatch between the materials.

The future model should include heat generation due to solid and viscous friction. This heat generation can then be used to predict the temperature rise in the lubricant and components. Thermal deflections and temperature dependent viscosity should also be considered. A thermal

contact resistance model can be included to consider heat conduction across the interfaces, similar to Jackson's previous work [76, 77].

Using this, along with models for viscous and solid friction, a Stribeck curve can be generated. Each Stribeck Curve is unique to a certain surface geometry, lubricant, and material. The code can provide a prediction of the separation distance between the surfaces at each location. This surface separation can then be used to predict the fluid flow across the piston, or blow-by. In addition, the code could be able to make predictions of film thickness, pressure profiles, frictional torques, temperature rises in the material and lubricant, stresses in the material, and other quantities. Most importantly, the stresses can also be used to predict failure and wear of the coating and surface material itself.

The future model should also include the transient nature of the combustion cycle as it is a time variant process and should be modeled as such. For this reason, a transient model would better predict the relative velocity between the piston, piston ring, and the cylinder wall. This transient model thusly would predict a more accurate film thickness, pressure induced gradients, thermal stresses, and more importantly the cyclic stresses experienced. This leads to a more accurate prediction of failure and wear among the power cylinder component interface.

## APPENDIX A

### PROGRAM CODE

The following is a list of all the scripts and functions in this Appendix and the pages where they appear.

Governing Program..... 141

#### Functions

CylinderWall\_GP..... 149

FlattenedTopRing\_GP ..... 151

True\_FF\_CalculationsWallRing\_X\_GP..... 152

    True\_FF\_Calculations\_RoughSurfaceWallRing\_X\_GP ..... 153

    True\_FF\_Calculations\_SmoothSurfaceV2XDIRECTION\_GP ..... 159

True\_FF\_CalculationsWallRing\_Z\_GP ..... 164

    True\_FF\_Calculations\_RoughSurfaceWallRing\_Z\_GP..... 165

    True\_FF\_Calculations\_SmoothSurfaceV2ZDIRECTION\_GP ..... 171

True\_FF\_Calculations\_ShearV2\_GP ..... 176

True_FF_CalculationsRoughSurfaceWallShear_GP.....	178
True_FF_CalculationsRoughSurfaceRingShear_GP.....	184
Fit_FF_Curves_GP.....	191
RE2DwithFF_GP.....	196
ACF_SurfaceTest.....	200
eplasticG_Wcf_GP.....	206
Simpsons_1_3_GP.....	207

```

%*****
%*****
%***          USE OF SURFACE SPECIFIC FLOW FACTORS IN A MULTI-          ***
%*                                                    *
%*          PHYSICAL MODEL OF POWER CYLINDER COMPONENTS                *
%*                                                    *
%*          MASTERS THESIS 2018                                         *
%*                                                    *
%*          ALEX J. LOCKER IV                                           ***
%*****
%*****

```

```

%*****
% The following program is the governing program for the combined lubrication
% and contact models. The program first takes in two sets of surfaces, assuming
% they are the same size. Then the program derives the three set of flow factor
% equations, namely (X,Z,S), for the two interacting surfaces. Following this
% derivation the program iterates the film thickness, h, and utilizes the flow
% factor equations along with the contact models to predict the pressure at
% each point in the mesh. The program is assumed that at film thickness greater
% than 10*Rq the pressure is solely due to hydrodynamic forces and the contact
% pressures are ignored.
%*****

```

```

%*****Call the Two Surfaces*****

```

```

%          |-----|
%          | Plot the Cylinder Wall Surface |
%          |-----|

```

```

CylinderWall_GP
figure()
mesh(Leveledz2);
xlabel('X-direction')
ylabel('Z-direction')
zlabel('Height (\mum)')
title('D35 Cylinder Wall Surface','FontSize',20)

```

```

%Calculate Root Mean Square Roughness (Standard Deviation) of Surface 1
(Cylinder Wall)
Rq1 = 0;
len = length(Leveledz2);
for j = 1:len
    OldRq1 = Rq1;
    Rq1 = (z2(j)-avgz(j))^2 + OldRq1;
    if j == len
        Rq1 = (Rq1/len)^(1/2);
    end

```

```

    j = j + 1;
end
Rq1 = Rq1 * (1e-4);

```

```

%
%
%

```

```

|-----|
| Plot the Piston Ring Surface |
|-----|

```

```

FlattenedTopRing_GP
figure()
mesh(LeveledFit)
% axis([0 1000 0 1000 -2 4])
xlabel('X-direction')
ylabel('Z-direction')
zlabel('Height (\mum)')
title('D35 Piston Ring Surface without Curvature','FontSize',20)
grid on

```

```

%Calculate Root Mean Square Roughness (Standard Deviation) of Surface 2 (D35
Ring)

```

```

Rq2 = 0;
len2 = length(fitwall);
for j = 1:len2
    OldRq2 = Rq2;
    Rq2 = (fitwall(j)-AverageData)^2 + OldRq2;
    if j == len2
        Rq2 = (Rq2/len2)^(1/2);
    end
    j = j + 1;
end
Rq2 = Rq2 * (1e-4);

```

```

%Calculate the Composite RMS Roughness
sigma = sqrt(Rq1^2 + Rq2^2);

```

```

%*****Derive the Flow Factors*****
%*****
% NOTE: The following is derived under several assumptions:
%   -Below 2*sigma: Only the shear flow factor, and contact models are used
%   -Between 2*sigma and 10*sigma all flow factors and contact models are used
%   -Above 10*sigma only flow factor are used
%*****

for FR = 1:1:12
    h = FR*sigma;
    if FR < 2
        [phis(FR),LPS1(FR),LPS2(FR)] = True_FF_Calculations_ShearV2_GP(h);

    elseif FR < 10
        phix(FR) = True_FF_CalculationsWallRing_X_GP(h);
        phiz(FR) = True_FF_CalculationsWallRing_Z_GP(h);
        [phis(FR),LPS1(FR),LPS2(FR)] = True_FF_Calculations_ShearV2_GP(h);

    else
        phix(FR) = True_FF_CalculationsWallRing_X_GP(h);
        phiz(FR) = True_FF_CalculationsWallRing_Z_GP(h);
        [phis(FR),LPS1(FR),LPS2(FR)] = True_FF_Calculations_ShearV2_GP(h);

    end
end

phix = phix(1,2:end); %Unstable below 1.5*sigma -> Only extract 2*sigma and
greater
phiz = phiz(1,2:end); %Unstable below 1.5*sigma -> Only extract 2*sigma and
greater

%
%
%
% FilmRatio = [ 1      2      3      4      5      6      7      8
                9      10     11     12 ];
% phis      = [0.5111  0.2526  0.1697  0.1276  0.1019  0.0846  0.0726  0.0639
                0.0573  0.0513  0.0466  0.0427];
% LPS1      = [0.4522  0.2219  0.1491  0.1128  0.0893  0.0743  0.0637  0.0562
                0.0504  0.0453  0.0412  0.0377];
% LPS2      = [1.0544  0.5358  0.3601  0.2643  0.2182  0.1793  0.1552  0.1347
                0.1216  0.1065  0.0965  0.0882];
% phix      = [ 1.7376  1.3714  1.2198  1.1351  1.0872  1.0430  1.0379
                1.0339  1.0306  1.0280  1.0257];
% phiz      = [ 0.6779  0.7838  0.8396  0.8866  0.9038  0.9166  0.9263
                0.9340  0.9402  0.9454  0.9497];

%Set up Film Ratio Vector

```





```

BC16 = P_chamber;           % Section 1
BC12 = P_chamber;           % Between Section 1 and Section 2
BC23 = P_chamber - BCs;     % Pressure decreases going from Section 1 to Section 5
around ring
BC34 = P_chamber - 2*BCs;   % Between Section 3 and Section 4, two nodes away
from BC1
BC45 = P_crankshaft;       % Between Section 4 and Section 5
BC56 = P_crankshaft;       % Between Section 5 and Section 6

%*****Pressure On Upper Ring Surface*****
%*****SECTION 1 & SECTION 2*****
%-----SECTION 1-----
P_total1(1:Sec1) = P_chamber;

%-----SECTION 2-----
count = 1;
for i = 1:Sec2
    z2(i) = dx * (i-1);
    h2(i) = testz(1,(width-(Sec2-count)));
    count=count+1;
end

%Combined location along width of ring
for i = 1:width
    zland2(i) = dx * (i-1);
end

P_hydro2 = RE2DwithFF_GP(h2,z2,dx,u2,BC12,BC23,az,bz,as,bs,cs,sigma);
%Calculate the hydrodynamic pressure at each node
P_contact2 = eplasticG_Wcf_GP(h2);
% Calculate the contact pressure at each node
P_contact2 = P_contact2(:,3)';
% Column1=X-Direction Column2=Z-Direction Column3=Average
P_total2 = P_hydro2 + P_contact2;
% Sum the hydrodynamic and contact pressures (Pa)
P_TotalUpper = [P_total2 P_total1];
% Total Pressure forces on upper ring surface
% zland2 = [z1 z2];
% Combined Numerical discretization grid

%*****Pressure On Inner Ring Surface*****
%*****SECTION 3*****
% Set up numerical grid along axial width of the ring
for i = 1:height
    z3(i) = dz * (i-1);
    h3(i) = testz(i,width);
end

```

```

P_hydro3 = RE2DwithFF_GP(h3,testz(:,1),dz,u3,BC23,BC34,az,bz,as,bs,cs,sigma)
% Calcualte the hydrodynamic pressure at each node
P_contact3 = eplasticG_Wcf_GP(h3);
% Calculate the contact pressure at each node
P_contact3 = P_contact3(:,3)';
% Column1=X-Direction Column2=Z-Direction Column3=Average
P_total3 = P_hydro3 + P_contact3;
% Sum the hydrodynamic and contact pressures (Pa)
P_TotalInner = [P_total3]; % Total Pressure forces on inner ring surface

%*****Pressure On Lower Ring Surface*****
%*****SECTION 4 & SECTION 5 *****
%-----SECTION 4-----
count = 1;
for i = 1:Sec2 %Try last 5 nodes [5 would be #2]
    z4(i) = dx * (i-1);
    h4(i) = testz(1,(width-(Sec2-count)));
    count=count+1;
end

%-----SECTION 5-----
P_total5(1:Sec1) = P_crankshaft; %15 would be #1

%Combined location along width of ring
for i = 1:width
    z4and5(i) = dx * (i-1);
end

P_hydro4 = RE2DwithFF_GP(h2,z2,dx,u2,BC12,BC23,az,bz,as,bs,cs,sigma);
% Calculate the hydrodynamic pressure at each node
P_contact4 = eplasticG_Wcf_GP(h2);
% Calculate the contact pressure at each node
P_contact4 = P_contact4(:,3)';
% Column1=X-Direction Column2=Z-Direction Column3=Average
P_total4 = P_hydro4 + P_contact4;
% Sum the hydrodynamic and contact pressures (Pa)
P_TotalLower = [P_total4 P_total5];
% Total Pressure forces on lower ring surface
% zland2 = [z1 z2];
% Combined Numerical discretization grid

%*****Pressure On Outer Ring Surface*****
%*****SECTION 6*****
% Set up numerical grid along axial width of the ring
for i = 1:height
    z6(i) = dz * (i-1); %Z location at each node
    h6(i) = ho + (hi-ho)/(height-1)*(i-1); %Linear equation for film
    thickness at each node

```

```

end

P_hydro6 =
RE2DwithFF_GP(h6,z6,dz,u6,P_crankshaft,P_chamber,az,bz,as,bs,cs,sigma);
% Calculate the hydrodynamic pressure at each node
P_contact6 = eplasticG_Wcf_GP(h6);
% Calculate the contact pressure at each node
P_contact6 = P_contact6(:,3)';
% Column1=X-Direction Column2=Z-Direction Column3=Average
P_total6 = P_hydro6 + P_contact6;
% Sum the hydrodynamic and contact pressures (Pa)
P_TotalOuter = [P_total6]
% Total Pressure forces on outer ring surface

%*****Plot the Pressure on each ring surface*****
%-----UPPER-----
figure()
plot(z1and2,P_TotalUpper) %Can also make (z1and2,P_TotalUpper)
title('Pressure on Upper Ring Surface','FontSize',20)
ylabel('Pressure (Pa)')
xlabel('Distance (m)')
grid on

%-----Inner-----
figure()
plot(z3,P_TotalInner) %Can also make (z3,P_TotalOuter)
title('Pressure on Inner Ring Surface','FontSize',20)
ylabel('Pressure (Pa)')
xlabel('Distance (m)')
grid on

%-----Lower-----
figure()
plot(z4and5,P_TotalLower) %%Can also make (z4and5,P_TotalUpper)
title('Pressure on Lower Ring Surface','FontSize',20)
ylabel('Pressure (Pa)')
xlabel('Distance (m)')
grid on

%-----Outer-----
figure()
plot(z6,P_TotalOuter) %Can also make (z6,P_TotalOuter)
title('Pressure on Outer Ring Surface','FontSize',20)
ylabel('Pressure (Pa)')
xlabel('Distance (m)')
grid on

```

```

%*****
%*****
%***          CYLINDER WALL FUNCTION          ***
%*
%*          MASTERS THESIS 2018              *
%*
%***          ALEX J. LOCKER IV              ***
%*****
%*****

%*****
% The following function calls the raw surface data heights from a text file
% that was created by the profilometer. Upon collecting the surface heights,
% the data heights are then leveled, where the average is subtracted out. The
% average is subtracted out one row at a time in the order the profilometer
% measured the surface row.
%*****

%////////////////////////////////////
%
%          -----
%          |  FORD SURFACE 1  |
%          -----
%////////////////////////////////////

%Read in the data into 5 columns
[A B C D E] = textread('Surfacel_NoWords_GP.txt','%f %c %f %c
%c','headerlines',20);          %Need file to end with numbers

%FOR THE Y VALUES USE THIS CODE
w = 1000; %Number of Samples per row
n = 999; %Number of Repeating Samples
v = repmat(0:n,[w 1]);
v = v(:);

x1 = A;
y1 = v;
z1 = C;

%*****LEVEL THE DATA*****
for j = 1:1000
    sumz = 0;

    if j==1

        for i = 1:1000          %Sum points from 1 to 1000
            sumz = sumz + z1(i);
        end
        a = polyfit(i,j,1);
        avgz(j) = sumz/1000;
    end
end

```

```

        k=0;
        for i = 1 : 1000 %Sum points from X001 to (X+1)000
            k=k+1;
            z2(j,k)=z1(i)-avgz(j)-a(1);
        end
elseif j<=999
    sumz=0;
(X+1)000    for i = (1000*j+1) : (1000*j+1000) %Sum points from X001 to

            sumz = sumz + z1(i);
        end
        w = polyfit(i,j,1);
        avgz(j) = sumz/1000;
        k=0;
(X+1)000    for i = (1000*j+1) : (1000*j+1000) %Sum points from X001 to

            k=k+1;
            z2(j,k)=z1(i)-avgz(j)-w(1);
        end

    else %For the last point
        for i = 999001:1000000
            sumz = sumz + z1(i);
        end
        e = polyfit(i,j,1);
        avgz(j) = sumz/1000 - e(1);
        k=0;
        for i = 999001:1000000 %Sum points from X001 to (X+1)000
            k=k+1;
            z2(j,k)=z1(i)-avgz(j)-e(1);
        end

    end %End j decision loop
end %End j loop

```

```

%*****
%*****
%***          PISTON RING FUNCTION          ***
%*
%*          MASTERS THESIS 2018          *
%*
%***          ALEX J. LOCKER IV          ***
%*****
%*****

%*****
% The piston ring data was supplied from ford with its curvature. This function
% eliminates any curvature.
%*****

RingX = xlsread('RingData_GP.xlsx',1);
RingY = xlsread('RingData_GP.xlsx',2);
RingZ = xlsread('RingData_GP.xlsx',3);

fitwall = xlsread('No Curve Cylinder Wall_GP.xlsx',1);

%*****Level the Data by putting the average at zero*****
% size(fit) %The size of variable fit is 1000x1000
% Total data points is 1e6
AverageData = (sum(sum(fitwall))) / 1e6;
LeveledFit = fitwall - AverageData;

%Check Leveled fit (Average should be zero)
AverageDataCheck = (sum(sum(LeveledFit))) / 1e6;

```



```

%*****
%*****
%***          ROUGH SURFACE X DIRECTION PRESSURE FLOW FACTOR          ***
%*
%*          MASTERS THESIS 2018          *
%*
%***          ALEX J. LOCKER IV          ***
%*****
%*****

%*****
% The following function is used to calculate the nodal pressures at one film
% thickness for the rough surface. The film thickness is iterated in the %
governing program code.
%*****

function [ q_x_RS ] =
True_FF_Calculations_RoughSurfaceWallRingXDIRECTION_GP(h)

%film thickness (h) is used in line 186

clc;
warning('off','all')

%////////////////////////////////////
%
%          |  VARIABLES AND CONSTANTS  |
%          |-----|
%////////////////////////////////////

mu      = 0.1;      %Viscosity of the fluid (0.1)
u       = 0;       %Velocity of the bearing (1)
M       = 100;     %Number of nodes (Rows)
N       = 100;     %Number of nodes (Columns)
ho      = 2e-5;    %Height at edge of incline (2e-6)
hi      = 1e-5;    %Height at edge of incline (1e-6)
L       = 0.01;    %Length of whole bearing (0.01)
dx      = L/(N-1); %Distance between nodes
dz      = L/(M-1); %Distance between nodes
PRS     = zeros(M,N); %Initial pressure guess
PRS(:, :) = 250;
PRS(:,1) = 100;    %Pressure in combustion chamber just after combustion
                (~30 bar = 30e6 Pa)
PRS(:,M) = 400;    %Pressure in crankcase (~assuming atmospheric)
PRSSmall = 100;
PRSLarge = 400;

error   = 10;      %Large initial error to enter loop
crit    = 0.01;    %Convergence criteria of percent error (1%)
sigma   = 1e-6;    %Standard Deviation

```

```

%Call Cylinder Wall
CylinderWall_GP

%Calculate Root Mean Square Roughness (Standard Deviation) of Surface 1
(Cylinder Wall)
Rq1 = 0;
len = length(Leveledz2);
for j = 1:len
    OldRq1 = Rq1;
    Rq1 = (z2(j)-avgz(j))^2 + OldRq1;

    if j == len
        Rq1 = (Rq1/len)^(1/2);
    end

    j = j + 1;
end
Rq1 = Rq1 * (1e-6);

%Call Second Surface (D35 Ring)
FlattenedTopRing_GP

%%%%%%%%%%%%%%%%%%%%%%%%%%%%%%%%%%%%%%%%%%%%%%%%%%%%%%%%%%%%%%%%%%%%%%%%
%
%          |  CALCULATION  |
%          |-----|
%
%%%%%%%%%%%%%%%%%%%%%%%%%%%%%%%%%%%%%%%%%%%%%%%%%%%%%%%%%%%%%%%%%%%%%%%%

% dx = 2.0408e-6 meters;
% dz = 2.0408e-6 meters;

for i = 1:M

    for j = 1:N
        z(i) = dz * (i-1);

        %*****Basic Equation for h*****
        hRS(i,j) = (LeveledFit(i) - Leveledz2(i,j))*(10^-5) + h*(1e-1);

        x(j) = dx * (j-1);           %X location at each node

        %Initial Pressure Guess (Line)
        PRS(i,j) = PRSsmall + (PRSlarge-PRSsmall)/(N-1)*(j-1);
    end
end
end

```

```

%Plot the Film Thickness
figure()
surf(hRS)
axis([0 100 0 100 0 5e-5])
xlabel('X-direction')
ylabel('Z-direction')
zlabel('Height/Distance (\mum)')
title('Film Thickness','FontSize',20)
grid on

%Plot the two Sliding Surfaces
figure()
mesh(z2-3)
hold on
mesh(fit)
xlabel('X-direction')
ylabel('Z-direction')
zlabel('Height/Distance (\mum)')
title('Two Sliding Surfaces','FontSize',20)
grid on

% FOR DISTANC BEWTEEN TWO SURFACES - UPDATED FILM THICKNESS
% hRS = hRS - (-hRS);

%*****2D PRESSURE PROFILE*****
figure();
grid on;
plot(x,PRS);      %Plots every tenth iteration to show convergence
grid on
xlabel('x (m)');
ylabel('P (pa)');
hold off;        %Shows all lines (hold off = show most recent)

%*****CALCULATE UNTIL CONVERGENCE CRITERA REACHED*****
it = 0;  %Iteration counter
it2=0;
while (error>crit)
    it2=it2+1;  %Uncomment for increment
    it = it + 1;    %Increment iteration counter
    OldPressure = PRS; %Updates new pressure
    error = 0;      %Set error to zero to initialize it

%*****NUMERICAL GRID CALCULATIONS*****
for i = 1:(M)      %Calculate Pressure at all nodes with periodic BC's [i
                    direction]

    for j = 2:(N-1) %Calculate Pressure at all nodes with periodic BC's
                    [j direction]

```

```

%Periodic Boundary Conditions with Ghost Nodes
%*****M Direction (i direction)*****
    ii_1 = i+1;
    ii_2 = i-1;

    if ii_1 > M
        ii_1 = ii_1 - M;
    end

    if ii_2 < 1
        ii_2 = ii_2 + M;
    end

%*****NUMERICAL FILM THICKNESS GRID*****
%In the i direction
h3 = (hRS(ii_1,j)+hRS(i,j))/2; %Halfway in between node ahead
h4 = (hRS(i,j)+hRS(ii_2,j))/2; %Halfway in between node behind

%In the j direction
h1 = (hRS(i,j+1)+hRS(i,j))/2; %Halfway in between node ahead
h2 = (hRS(i,j)+hRS(i,j-1))/2; %Halfway in between node behind

%*****NUMERICAL GRID FOR DELTA*****
%In the j direction
delx(j+1) = dx; %x(j+1)-x(j); %Halfway in between node ahead
delx(j) = dx; %x(j)-x(j-1); %Halfway in between node behind

%In the i direction
delz(ii_1) = dz; %z(i+1)-z(i); %Halfway in between node ahead
if i==1
    delz(i) = 0.000101;
else
    delz(i) = dz; %z(i)-z(ii_2); %Halfway in between node behind
end

%*****REYONLDS COEFFICIENTS*****
a0 = 6*mu*u*((h3-h4)/(delx(j)+delx(j+1)));
a1 = (h4^3)/(delx(j)*(delx(j)+delx(j+1)));
a2 = (h3^3)/(delx(j+1)*(delx(j)+delx(j+1)));
a3 = (h2^3)/(delz(i)*(delz(i)+delz(ii_1)));
a4 = (h1^3)/(delz(ii_1)*(delz(i)+delz(ii_1)));
a5 = a1 + a2 + a3 + a4;

%*****3D PRESSURE EQUATION*****
PRS(i,j) = a1*PRS(i,j-1) + a2*PRS(i,j+1) + a3*PRS(ii_2,j) +
          a4*PRS(ii_1,j) - a0;
PRS(i,j) = PRS(i,j)/(a5);

%*****FLOW RATES FOR POISEULLE FLOW*****
q_z_RS = (-hRS^3)/(12*mu) * ((PRS(ii_1,j)-PRS(ii_2,j))/dz);

```

```

q_x_RS = ((-(hRS^3)/(12*mu)) * ((PRS(i,j+1)-PRS(i,j-1))/dx)) +
u*hRS;

%*****FLOW RATES FOR COUETTE FLOW*****
q_x_RS_C = (u/2) * (hRS/M);

%*****CALCULATE ERROR*****
%Make sure Pressure is not zero and add errors
if(abs(PRS(i,j))>0)
    error = error + abs((PRS(i,j)-OldPressure(i,j))/PRS(i,j));
end

%*****RELAXATION*****
PRS(i,j)=0.9*PRS(i,j)-0.8*OldPressure(i,j);    %Relaxation of 0.8

end    %End j Loop

end    %End i Loop

%Calculate average error in percent
error = error/(N-2)*100/M; %/N    Uncomment to see error decrease
if(it<10)
    error=10;
end

%*****PLOT THE TENTH ITERATION*****
if (it==10)
    plot(x,PRS);
    title('Pressure Distribution','FontSize',20)
    grid on
    grid minor
    xlabel('x(m)')
    ylabel('P(pa)')

    hold off
    plot(z,PRS);
    title('Z-Pressure Distribution','FontSize',20)
    grid on
    grid minor
    xlabel('z(m)')
    ylabel('P(pa)')
    it=0;    %Reset iteration counter
end

end    %End convergence criteria loop

```

```

%////////////////////////////////////
%
%          -----
%          |   OUTPUT   |
%          -----
%\\////////////////////////////////////
%*****PLOT FILM THICKNESS*****
figure()
plot(x,hRS)
title('Film Thickness','FontSize',20)
grid on
figure()
surf(hRS)
title('Film Thickness','FontSize',20)
xlabel('X-direction')
ylabel('Z-direction')
zlabel('Height(\mum)')
grid on

%*****PLOT FLOW RATES*****
figure()
surf(q_x_RS_C)
title('3D Flow Rates - Couette Flow','FontSize',20)
xlabel('X-direction (\mum)')
ylabel('Z-direction (\mum)')
zlabel('Flow Rate (m^3/s)')
set(gca,'XTickLabel',{'0';'200';'400';'600';'800';'1000'})
set(gca,'YTickLabel',{'0';'500';'1000'})
grid on

%*****PLOT 3D PRESSURE CURVES*****
%Plot Surface Mesh
figure()
surf(PRS)
xlabel('X-direction (\mum)')
ylabel('Z-direction (\mum)')
zlabel('Pressure (Pa)')
set(gca,'XTickLabel',{'0';'200';'400';'600';'800';'1000'})
set(gca,'YTickLabel',{'0';'500';'1000'})
axis([0 50 0 50 -10e6 10e6])
colorbar
title('3D Reynolds Plot - Poiseuille Flow','FontSize',20)
%Plot Mesh
figure()
mesh(PRS)
xlabel('X-direction (\mum)')
ylabel('Z-direction (\mum)')
zlabel('Pressure (Pa)')
set(gca,'XTickLabel',{'0';'200';'400';'600';'800';'1000'})
set(gca,'YTickLabel',{'0';'500';'1000'})
title('3D Reynolds Plot - Couette Flow ','FontSize',20)
end %End function

```

```

%*****
%*****
%***          SMOOTH SURFACE X DIRECTION PRESSURE FLOW FACTOR          ***
%*
%*          MASTERS THESIS 2018
%*
%***          ALEX J. LOCKER IV          ***
%*****
%*****

%*****
% The following function is used to calculate the nodal pressures at one film
% thickness for the smooth surface. The film thickness is iterated in the
% governing program code.
%*****

function [q_x_SS] = True_FF_CalculationsV2XDIRECTION_GP(h)

%film thickness (h) is used in line 58

%////////////////////////////////////
%
%          |  VARIABLES AND CONSTANTS  |
%          |-----|
%
%////////////////////////////////////

mu      = 0.1;      %Viscosity of the fluid (0.1)
u       = 0;       %Velocity of the bearing (1)
M       = 100;     %Number of nodes (Rows)
N       = 100;     %Number of nodes (Columns)
ho      = 2e-5;    %Height at edge of incline (2e-6)
hi      = 1e-5;    %Height at edge of incline (1e-6)
L       = 0.01;    %Length of whole bearing (0.01)
dx      = L/(N-1); %Distance between nodes
dz      = L/(M-1); %Distance between nodes
PSS     = zeros(M,N); %Initial pressure guess

PSS(:, :) = 250;
PSS(:, 1) = 100;      %Pressure in combustion chamber just after combustion
                    (~30 bar = 30e6 Pa)
PSS(:, M) = 400;     %Pressure in crankcase (~assuming atmospheric)
PSSsmall = 100;
PSSlarge = 400;

error   = 10;        %Large initial error to enter loop
crit    = 0.1;       %Convergence criteria of percent error (0.1%)

```

```

%%%%%%%%%%%%%%%%%%%%%%%%%%%%%%%%%%%%%%%%%%%%%%%%%%%%%%%%%%%%%%%%%%%%%%%%
%
%
%
%
%%%%%%%%%%%%%%%%%%%%%%%%%%%%%%%%%%%%%%%%%%%%%%%%%%%%%%%%%%%%%%%%%%%%%%%%

for i = 1:M      %i is top and bottom (Z Direction)

    for j = 1:N  %j is left and right sides (X Direction)
        %Set z = i for infinitely long bearing
        z(i) = dz * (i-1);

        hSS(i,j) = h*(1e-1);%2e-5; %take complete average of hRS (5.7665e-5)

        x(j) = dx * (j-1);          %X location at each node

        %Initial Pressure Guess (Line)
        PSS(i,j) = PSSsmall + (PSSlarge-PSSsmall)/(N-1)*(j-1);

    end
end

figure()
surf(hSS)
axis([0 100 0 100 1e-5 5e-5])
xlabel('X-direction')
ylabel('Z-direction')
zlabel('Height (\mum)')
title('Film Thickness','FontSize',20)
grid on

%*****2D PRESSURE PROFILE*****
figure();
grid on;
plot(x,P); %Plots every tenth iteration to show convergence
grid on
xlabel('x (m)');
ylabel('P (pa)');
hold off; %Shows all lines (hold off = show most recent)

%*****CALCULATE UNTIL CONVERGENCE CRITERIA REACHED*****
it = 0; %Iteration counter
it2=0;
while (error>crit)
    it2=it2+1;
    it = it + 1; %Increment iteration counter
    OldPressure = PSS; %Updates new pressure
    error = 0; %Set error to zero to initialize it

%*****NUMERICAL GRID CALCULATIONS*****

```

```

for i = 1:(M)      %Calculate Pressure at all nodes except at the
                  edge(Boundary Conditions) {i direction}

    for j = 2:(N-1) %Calculate Pressure at all nodes except at the edge
                  {j direction}

        %Periodic Boundary Conditions with Shost Nodes
        %*****M Direction (i direction)*****
        ii_1 = i+1;
        ii_2 = i-1;

        if ii_1 > M
            ii_1 = ii_1 - M;
        end

        if ii_2 < 1
            ii_2 = ii_2 + M;
        end

        %*****NUMERICAL FILM THICKNESS GRID*****
        %In the i direction
        h3 = (hSS(ii_1,j)+hSS(i,j))/2; %Halfway in between node ahead
        h4 = (hSS(i,j)+hSS(ii_2,j))/2; %Halfway in between node behind

        %In the j direction
        h1 = (hSS(i,j+1)+hSS(i,j))/2; %Halfway in between node ahead
        h2 = (hSS(i,j)+hSS(i,j-1))/2; %Halfway in between node behind

        %*****NUMERICAL GRID FOR DELTA*****
        %In the j direction
        delx(j+1) = dx; %x(j+1)-x(j); %Halfway in between node ahead
        delx(j)   = dx; %x(j)-x(j-1); %Halfway in between node behind

        %In the i direction
        delz(ii_1) = dz; %z(ii_1)-z(i); %Halfway in between node ahead
        if i==1
            delz(i) = 0.000101;
        else
            delz(i) = dz; %z(i)-z(ii_2); %Halfway in between node behind
        end

        %*****REYONLDS COEFFICIENTS*****
        a0 = 6*mu*u*((h3-h4)/(delx(j)+delx(j+1)));
        a1 = (h4^3)/(delx(j)*(delx(j)+delx(j+1)));
        a2 = (h3^3)/(delx(j+1)*(delx(j)+delx(j+1)));
        a3 = (h2^3)/(delz(i)*(delz(i)+delz(ii_1)));
        a4 = (h1^3)/(delz(ii_1)*(delz(i)+delz(ii_1)));
        a5 = a1 + a2 + a3 + a4;

        %*****3D PRESSURE EQUATION*****

```

```

PSS(i,j) = a1*PSS(i,j-1) + a2*PSS(i,j+1) + a3*PSS(ii_2,j) +
          a4*PSS(ii_1,j) - a0;
PSS(i,j) = PSS(i,j)/(a5);

%*****FLOW RATES FOR POISEULLE FLOW*****
q_z_SS = (-hSS^3)/(12*mu) * ((PSS(ii_1,j)-PSS(ii_2,j))/dz);
q_x_SS = ((-hSS^3)/(12*mu) * ((PSS(i,j+1)-PSS(i,j-1))/dx)) +
          u*hSS;

%*****FLOW RATES FOR COUETTE FLOW*****
q_x_SS_C = (u/2)* (hSS/M);

%*****CALCULATE ERROR*****
%Make sure Pressure is not zero and add errors
if(abs(PSS(i,j))>0)
    error = error + abs((PSS(i,j)-OldPressure(i,j))/PSS(i,j));
end

%*****RELAXATION*****
PSS(i,j)=1.9*PSS(i,j)-0.9*OldPressure(i,j);    %Relaxation of 1.9

end    %End j Loop

end    %End i Loop

%Calculate average error in percent
error = error/(N-2)*100/M;    %Uncomment for decreasing error
if(it<10)
    error=10;
end

%*****PLOT THE TENTH ITERATION*****
if (it==10)
    plot(x,PSS);
    title('X-Pressure Distribution','FontSize',20)
    grid on
    grid minor
    xlabel('x(m)')
    ylabel('P(pa)')

    hold off
    plot(z,PSS);
    title('Z-Pressure Distribution','FontSize',20)
    grid on
    grid minor
    xlabel('z(m)')
    ylabel('P(pa)')
    it=0;    %Reset iteration counter
end
end    %End convergence criteria loop

```

```

%////////////////////////////////////
%
%
%
%
%////////////////////////////////////
%NOTE: Pressure is induced between the two sliding surfaces due to pressure
%in the chamber and the crankcase.

%*****PLOT FILM THICKNESS*****
figure()
plot(x,hSS)
title('Film Thickness','FontSize',20)
grid on

%*****PLOT FLOW RATES*****
figure()
mesh(q_x_SS_C)
title('3D Flow Rates - Couette Flow','FontSize',20)
xlabel('X-direction (\mum)')
ylabel('Z-direction (\mum)')
zlabel('Flow Rate (m^3/s)')
axis([0 100 0 100 0.5e-7 2.5e-7])
set(gca,'XTickLabel',{'0';'200';'400';'600';'800';'1000'})
set(gca,'YTickLabel',{'0';'500';'1000'})
grid on

%*****PLOT 3D PRESSURE CURVES*****
%Plot Surface Mesh
figure()
surf(x,z,PSS)
xlabel('X-direction (\mum)')
ylabel('Z-direction (\mum)')
zlabel('Pressure (Pa)')
set(gca,'XTickLabel',{'0';'200';'400';'600';'800';'1000'})
set(gca,'YTickLabel',{'0';'500';'1000'})
title('3D Reynolds Plot - Poiseuille Flow','FontSize',20)

% %Normalized Surface Mesh
figure()
surf(x/L,z/L,P)
xlabel('X-direction')
ylabel('Z-direction')
title('3D Reynolds Plot')

%Plot Mesh
figure()
mesh(x,z,PSS)
xlabel('X-direction')
ylabel('Z-direction')
title('3D Reynolds Plot - Couette Flow','FontSize',20)
end %End function

```



```

%*****
%*****
%***          ROUGH SURFACE Z DIRECTION PRESSURE FLOW FACTOR          ***
%*
%*          MASTERS THESIS 2018          *
%*
%***          ALEX J. LOCKER IV          ***
%*****
%*****

```

```

%*****
% The following function is used to calculate the nodal pressures at one film
% thickness for the rough surface. The film thickness is iterated in the
% governing program code.
%*****

```

```

function [ q_z_RS ] =
True_FF_Calculations_RoughSurfaceWallRingZDIRECTION_GP(h)

```

```

%film thickness (h) is used in line 182

```

```

clc;
warning('off','all')

```

```

%////////////////////////////////////
%
%          |  VARIABLES AND CONSTANTS  |
%          |-----|
%
%////////////////////////////////////

```

```

mu      = 0.1;      %Viscosity of the fluid (0.1)
u       = 0;       %Velocity of the bearing (1
M       = 100;    %Number of nodes (Rows)
N       = 100;    %Number of nodes (Columns)
ho      = 2e-5;   %Height at edge of incline (2e-6)
hi      = 1e-5;   %Height at edge of incline (1e-6)
L       = 0.01;   %Length of whole bearing (0.01)
dx      = L/(N-1); %Distance between nodes
dz      = L/(M-1); %Distance between nodes
PRS     = zeros(M,N); %Initial pressure guess

PRS(:, :) = 250; %PRS(z,x)
PRS(1, :) = 100; %Pressure in combustion chamber just after combustion
              (~30 bar = 30e6 Pa)
PRS(M, :) = 400; %Pressure in crankcase (~assuming atmospheric)
PRSSmall = 100;
PRSLarge = 400;

error   = 10;     %Large initial error to enter loop
crit    = 0.01;   %Convergence criteria of percent error (1%)

```

```

sigma = 1e-6;      %Standard Deviation

%Call Cylinder Wall
CylinderWall_GP

%Calculate Root Mean Square Roughness (Standard Deviation)
Rq = 0;
for j = 1:N
    OldRq = Rq;
    Rq = (avgz(j)^2 + OldRq);

    if j == N
        Rq = (Rq/N)^(1/2);
    end

    j = j + 1;
end

%Call Second Surface (D35 Ring)
FlattenedTopRing_GP
figure()
mesh(LeveledFit)
% axis([0 1000 0 1000 -2 4])
xlabel('X-direction')
ylabel('Z-direction')
zlabel('Height/Distance (\mum)')
title('D35 Piston Ring Surface without Curvature','FontSize',20)
grid on

%////////////////////////////////////
%
%          -----
%          |  CALCULATION  |
%          -----
%////////////////////////////////////

% dx = 2.0408e-6; meters
% dz = 2.0408e-6; meters

for i = 1:M

    for j = 1:N
        z(i) = dz * (i-1);

        %*****Basic Equation for h*****
        hRS(i,j) = (LeveledFit(i) - Leveledz2(i,j))*(10^-5) + h*(1e-1);
    end
end

```

```

x(j) = dx * (j-1);          %X location at each node

    %Initial Pressure Guess (Line)
    PRS(i,j) = PRSsmall + (PRSlarge-PRSsmall)/(N-1)*(i-1);

end
end

figure()
surf(hRS)
% axis([0 100 0 100 0 5e-5])
xlabel('X-direction')
ylabel('Z-direction')
zlabel('Height/Distance (\mum)')
title('Film Thickness','FontSize',20)
grid on

%Plot the two Sliding Surfaces
figure()
mesh(z2-3)
hold on
mesh(fit)
xlabel('X-direction')
ylabel('Z-direction')
zlabel('Height/Distance (\mum)')
title('Two Sliding Surfaces','FontSize',20)
grid on

% FOR DISTANC BEWTEEN TWO SURFACES - UPDATED FILM THICKNESS
% hRS = hRS - (-hRS);

%*****2D PRESSURE PROFILE*****
figure();
grid on;
plot(z,PRS);      %Plots every tenth iteration to show convergence
grid on
xlabel('x (m)');
ylabel('P (pa)');
hold off;        %Shows all lines (hold off = show most recent)

%*****CALCULATE UNTIL CONVERGENCE CRITERA REACHED*****
it = 0;    %Iteration counter
it2=0;
while (error>crit)
    it2=it2+1;    %Uncomment to see error and and iterations go up
    it = it + 1;    %Increment iteration counter
    OldPressure = PRS; %Updates new pressure
    error = 0;      %Set error to zero to initialize it
end

```

```

%*****NUMERICAL GRID CALCULATIONS*****
for i = 2:(M-1) %Calculate Pressure at all nodes with periodic BC's
               {i direction} [z]

    for j = 1:(N) %Calculate Pressure at all nodes with periodic BC's {j
                  direction} [x]

        %Periodic Boundary Conditions with Ghost Nodes
        %*****N Direction (j direction)*****
        jj_1 = j+1;
        jj_2 = j-1;

        if jj_1 > N
            jj_1 = jj_1 - N;
        end

        if jj_2 < 1
            jj_2 = jj_2 + N;
        end

        %*****NUMERICAL FILM THICKNESS GRID*****
        %In the i direction
        h3 = (hRS(i+1,j)+hRS(i,j))/2; %Halfway in between node ahead
        h4 = (hRS(i,j)+hRS(i-1,j))/2; %Halfway in between node behind

        %In the j direction
        h1 = (hRS(i,jj_1)+hRS(i,j))/2; %Halfway in between node ahead
        h2 = (hRS(i,j)+hRS(i,jj_2))/2; %Halfway in between node behind

        %*****NUMERICAL GRID FOR DELTA*****
        %In the j direction
        delx(jj_1) = dx; %x(j+1)-x(j); %Halfway in between node ahead
        delx(j) = dx; %x(j)-x(j-1); %Halfway in between node behind

        %In the i direction
        delz(i+1) = dz; %z(i+1)-z(i); %Halfway in between node ahead
        if i=1
            delz(i) = 0.000101;
        else
            delz(i) = dz; %z(i)-z(ii_2); %Halfway in between node behind
        end

        %*****REYNOLDS COEFFICIENTS*****
        a0 = 6*mu*u*((h3-h4)/(delx(j)+delx(jj_1)));
        a1 = (h4^3)/(delx(j)*(delx(j)+delx(jj_1)));
        a2 = (h3^3)/(delx(jj_1)*(delx(j)+delx(jj_1)));
        a3 = (h2^3)/(delz(i)*(delz(i)+delz(i+1)));
        a4 = (h1^3)/(delz(i+1)*(delz(i)+delz(i+1)));
        a5 = a1 + a2 + a3 + a4;
    end
end

```

```

%*****3D PRESSURE EQUATION*****
PRS(i,j) = a1*PRS(i,jj_2) + a2*PRS(i,jj_1) + a3*PRS(i-1,j) +
          a4*PRS(i+1,j) - a0;
PRS(i,j) = PRS(i,j)/(a5);

%*****FLOW RATES FOR POISEULLE FLOW*****
q_z_RS = (-hRS^3)/(12*mu) * ((PRS(i+1,j)-PRS(i-1,j))/dz);
q_x_RS = ((-hRS^3)/(12*mu)) * ((PRS(i,jj_1)-PRS(i,jj_2))/dx) +
          u*hRS;

%*****FLOW RATES FOR COUETTE FLOW*****
q_x_RS_C = (u/2) * (sum(hRS'))/M;

%*****CALCULATE ERROR*****
%Make sure Pressure is not zero and add errors
if(abs(PRS(i,j))>0)
    error = error + abs((PRS(i,j)-OldPressure(i,j))/PRS(i,j));
end

%*****RELAXATION*****
PRS(i,j)=0.9*PRS(i,j)-0.8*OldPressure(i,j);    %Relaxation of 0.8

end    %End j Loop

end    %End i Loop

%Calculate average error in percent
error = error/(N-2)*100/M; %/N Uncomment to see error go down
if(it<10)
    error=10;
end

%*****PLOT THE TENTH ITERATION*****
if (it==10)
    plot(x,PRS);
    title('Pressure Distribution','FontSize',20)
    grid on
    grid minor
    xlabel('x(m)')
    ylabel('P(pa)')

    hold off
    plot(z,PRS);
    title('Z-Pressure Distribution','FontSize',20)
    grid on
    grid minor
    xlabel('z(m)')
    ylabel('P(pa)')
    it=0;    %Reset iteration counter
end
end

```

```

end    %End convergence criteria loop

%////////////////////////////////////
%
%                -----
%                |  OUTPUT  |
%                -----
%\\////////////////////////////////

%*****PLOT FILM THICKNESS*****
figure()
plot(x,hRS)
title('Film Thickness','FontSize',20)
grid on

figure()
surf(hRS)
title('Film Thickness','FontSize',20)
xlabel('X-direction')
ylabel('Z-direction')
zlabel('Height(\mum)')
grid on

%*****PLOT 3D PRESSURE CURVES*****
%Plot Surface Mesh
figure()
mesh(PRS)
xlabel('X-direction')
ylabel('Z-direction')
zlabel('Pressure (Pa)')
axis([0 50 0 50 -10e6 10e6])
colorbar
title('3D Reynolds Plot - Couette Flow','FontSize',20)

%Plot Mesh
figure()
surf(PRS)
xlabel('X-direction (\mum)')
ylabel('Z-direction (\mum)')
zlabel('Pressure (Pa)')
%Set axis labels
set(gca,'XTickLabel',{'0';'200';'400';'600';'800';'1000'})
set(gca,'YTickLabel',{'0';'500';'1000'})
title('3D Reynolds Plot - Poiseuille Flow ','FontSize',20)

end    %End function

```

```

%*****
%*****
%***          SMOOTH SURFACE Z DIRECTION PRESSURE FLOW FACTOR          ***
%*
%*          MASTERS THESIS 2018
%*
%*          ALEX J. LOCKER IV
%*****
%*****

%*****
% The following function is used to calculate the nodal pressures at one film
% thickness for the smooth surface. The film thickness is iterated in the
% governing program code.
%*****

function [q_z_SS] = True_FF_CalculationsV2ZDIRECTION_GP(h)

%film thickness (h) is used in line 58

%////////////////////////////////////
%
%          |  VARIABLES AND CONSTANTS  |
%          |-----|
%////////////////////////////////////

mu      = 0.1;      %Viscosity of the fluid (0.1)
u       = 0;       %Velocity of the bearing (1)
M       = 100;     %Number of nodes (Rows)
N       = 100;     %Number of nodes (Columns)
ho      = 2e-5;    %Height at edge of incline (2e-6)
hi      = 1e-5;    %Height at edge of incline (1e-6)
L       = 0.01;    %Length of whole bearing (0.01)
dx      = L/(N-1); %Distance between nodes
dz      = L/(M-1); %Distance between nodes
PSS     = zeros(M,N); %Initial pressure guess

PSS(:, :) = 250;
PSS(1, :) = 100;      %Pressure in combustion chamber just after combustion
                    (~30 bar = 30e6 Pa)
PSS(M, :) = 400;     %Pressure in crankcase (~assuming atmospheric)
PSSsmall = 100;
PSSlarge = 400;

error   = 10;        %Large initial error to enter loop
crit    = 0.1;       %Convergence criteria of percent error (0.1%)
                    0.1=A little squiggly 0.01=straight

```

```

%%%%%%%%%%%%%%%%%%%%%%%%%%%%%%%%%%%%%%%%%%%%%%%%%%%%%%%%%%%%%%%%%%%%%%%%
%
%          -----
%          |  CALCULATION  |
%          -----
%%%%%%%%%%%%%%%%%%%%%%%%%%%%%%%%%%%%%%%%%%%%%%%%%%%%%%%%%%%%%%%%%%%%%%%%

for i = 1:M      %i is top and bottom (Z Direction)

    for j = 1:N  %j is left and right sides (X Direction)

        z(i) = dz * (i-1);

        hSS(i,j) = h*(1e-1);%2e-5;  %take complete average of hRS (5.7665e-5)

        x(j) = dx * (j-1);          %X location at each node

        %Initial Pressure Guess (Line)
        PSS(i,j) = PSSsmall + (PSSlarge-PSSsmall)/(N-1)*(i-1);

    end
end

figure()
surf(hSS)
axis([0 100 0 100 1e-5 5e-5])
xlabel('X-direction')
ylabel('Z-direction')
zlabel('Height/Distance (\mum)')
title('Film Thickness','FontSize',20)
grid on

% *****2D PRESSURE PROFILE*****
figure();
grid on;
plot(x,P);      %Plots every tenth iteration to show convergence
grid on
xlabel('x (m)');
ylabel('P (pa)');
hold off;      %Shows all lines (hold off = show most recent)

%*****CALCULATE UNTIL CONVERGENCE CRITERA REACHED*****
it = 0;  %Iteration counter
it2=0;
while (error>crit)
    it2=it2+1; %Uncomment to see go up with error
    it = it + 1; %Increment iteration counter
    OldPressure = PSS; %Updates new pressure
    error = 0; %Set error to zero to initialize it
end

```

```

%*****NUMERICAL GRID CALCULATIONS*****
for i = 2:(M-1)      %Calculate Pressure at all nodes except at the edge
                    (Boundary Conditions) {i direction}

    for j = 1:(N) %Calculate Pressure at all nodes except at the edge {j
                  direction}

        %Periodic Boundary Conditions with ghost Nodes
        %*****N Direction (j direction)*****
        jj_1 = j+1;
        jj_2 = j-1;

        if jj_1 > N
            jj_1 = jj_1 - N;
        end

        if jj_2 < 1
            jj_2 = jj_2 + N;
        end

        %*****NUMERICAL FILM THICKNESS GRID*****
        %In the i direction
        h3 = (hSS(i+1,j)+hSS(i,j))/2; %Halfway in between node ahead
        h4 = (hSS(i,j)+hSS(i-1,j))/2; %Halfway in between node behind

        %In the j direction
        h1 = (hSS(i,jj_1)+hSS(i,j))/2; %Halfway in between node ahead
        h2 = (hSS(i,j)+hSS(i,jj_2))/2; %Halfway in between node behind

        %*****NUMERICAL GRID FOR DELTA*****
        %In the j direction
        delx(jj_1) = dx; %x(j+1)-x(j); %Halfway in between node ahead
        delx(j)    = dx; %x(j)-x(j-1); %Halfway in between node behind

        %In the i direction
        delz(i+1) = dz; %z(ii_1)-z(i); %Halfway in between node ahead
        if i==1
            delz(i) = 0.000101;
        else
            delz(i) = dz; %z(i)-z(ii_2); %Halfway in between node behind
        end

        %*****REYONLDS COEFFICIENTS*****
        a0 = 6*mu*u*((h3-h4)/(delx(j)+delx(jj_1)));
        a1 = (h4^3)/(delx(j)*(delx(j)+delx(jj_1)));
        a2 = (h3^3)/(delx(jj_1)*(delx(j)+delx(jj_1)));
        a3 = (h2^3)/(delz(i)*(delz(i)+delz(i+1)));
        a4 = (h1^3)/(delz(i+1)*(delz(i)+delz(i+1)));
        a5 = a1 + a2 + a3 + a4;
    end
end

```

```

%*****3D PRESSURE EQUATION*****
PSS(i,j) = a1*PSS(i,jj_2) + a2*PSS(i,jj_1) + a3*PSS(i-1,j) +
          a4*PSS(i+1,j) - a0;
PSS(i,j) = PSS(i,j)/(a5);

%*****FLOW RATES FOR POISEULLE FLOW*****
q_z_SS = (-hSS^3)/(12*mu) * ((PSS(i+1,j)-PSS(i-1,j))/dz);
q_x_SS = ((-hSS^3)/(12*mu)) * ((PSS(i,jj_1)-PSS(i,jj_2))/dx) +
          u*hSS;

%*****FLOW RATES FOR COUETTE FLOW*****
q_x_SS_C = (u/2)* (sum(hSS'))/M;

%*****CALCULATE ERROR*****
%Make sure Pressure is not zero and add errors
if(abs(PSS(i,j))>0)
    error = error + abs((PSS(i,j)-OldPressure(i,j))/PSS(i,j));
end

%*****RELAXATION*****
PSS(i,j)=1.9*PSS(i,j)-0.9*OldPressure(i,j);    %Relaxation of 1.9

end    %End j Loop

end    %End i Loop

%Calculate average error in percent
error = error/(N-2)*100/M;    %Uncomment to see error go down
if(it<10)
    error=10;
end

%*****PLOT THE TENTH ITERATION*****
if (it==10)
    plot(x,PSS);
    title('X-Pressure Distribution','FontSize',20)
    grid on
    grid minor
    xlabel('x(m)')
    ylabel('P(pa)')

    hold off
    plot(z,PSS);
    title('Z-Pressure Distribution','FontSize',20)
    grid on
    grid minor
    xlabel('z(m)')
    ylabel('P(pa)')
    it=0;    %Reset iteration counter
end
end

```

```

end    %End convergence criteria loop

%////////////////////////////////////
%
%                -----
%                |  OUTPUT  |
%                -----
%////////////////////////////////////
%NOTE: Pressure is induced between the two sliding surfaces due to pressure
%in the chamber and the crankcase.

%*****PLOT FILM THICKNESS*****
figure()
plot(x,hSS)
title('Film Thickness','FontSize',20)
grid on

%*****PLOT 3D PRESSURE CURVES*****
%Plot Surface Mesh
figure()
surf(x,z,PSS)
xlabel('X-direction (\mum)')
ylabel('Z-direction (\mum)')
zlabel('Pressure (Pa)')
%Set axis labels
set(gca,'XTickLabel',{'0';'200';'400';'600';'800';'1000'})
set(gca,'YTickLabel',{'0';'500';'1000'})
title('3D Reynolds Plot - Poiseuille Flow','FontSize',20)

%Normalized Surface Mesh
figure()
surf(x/L,z/L,P)
xlabel('X-direction')
ylabel('Z-direction')
title('3D Reynolds Plot')

%Plot Mesh
figure()
mesh(x,z,PSS)
xlabel('X-direction')
ylabel('Z-direction')
title('3D Reynolds Plot - Couette Flow','FontSize',20)

end    %End function

```

```

%*****
%*****
%***          SHEAR FLOW FACTOR          ***
%*
%*          MASTERS THESIS 2018          *
%*
%***          ALEX J. LOCKER IV          ***
%*****
%*****

%*****
% The following function is used to calculate the nodal pressures at one film
% thickness. The film thickness is iterated in the governing program code. This
% is the function to run the two other functions for the shear flow factor. The
% shear flow factor is calculated for each surface separately, then convoluted
% together.
%*****

function [phis,LPS1,LPS2] = True_FF_Calculations_Shear_V2_GP(h)

%Call programs
[LPS1,Rq1] = True_FF_Calculations_RoughSurfaceWallShear_GP(h);
[LPS2,Rq2] = True_FF_Calculations_RoughSurfaceRingShear_GP(h);

%Calculate cmpostire RMS sigmRoughness
sigma = sqrt(Rq1^2 + Rq2^2);

%Calculate the Shear Flow Factor
phis = ((Rq1/sigma)^2)*(LPS1) + ((Rq2/sigma)^2)*(LPS2);

% RESULTS
% hRS      = [ 9.3884e-5      1.4083e-04      1.8777e-04      2.3471e-04
               2.8165e-4      3.7554e-04      4.6942e-04      5.6331e-04
               6.5719e-04      7.5107e-04      ]
% FilmRatio = [      1          1.5          2          2.5
                  3          4          5          6
                  7          8          ]
% phis      = [ 0.5111      0.3436      0.2526      0.2051
               0.1697      0.1276      0.1019      0.0846
               0.0726      0.0639      ]
% LPS1(Wall)= [ 0.4522      0.3027      0.2219      0.1809
                0.1491      0.1128      0.0893      0.0743
                0.0637      0.0562      ]
% LPS2(Ring)= [ 1.0544      0.7213      0.5358      0.4292
                0.3601      0.2643      0.2182      0.1793
                0.1552      0.1347      ]

figure()
plot(FilmRatio,phis)

```

```
legend('Convolutd Surfaces')
axis([0 9 0 1])
grid on

figure()
plot(FilmRatio, LPS1)
hold on
plot(FilmRatio, LPS2)
hold on
plot(FilmRatio,phis)
legend('Wall', 'Ring', 'Convolutd Surfaces')
axis([0 9 0 1])
grid on

end %End function
```

```

%*****
%*****
%***          WALL - SMOOTH SURFACE SHEAR FLOW FACTOR          ***
%*
%*          MASTERS THESIS 2018
%*
%*          ALEX J. LOCKER IV
%*****
%*****

%*****
% The following function is used to calculate the nodal pressures at one film
% thickness. The film thickness is iterated in the governing program code. This
% is the function that runs the wall against a smooth surface.
%*****

function [LPS1,Rq1] = True_FF_CalculationsWallShear_GP(h)

%film thickness (h) is used in line 95

%////////////////////////////////////
%
%          |  VARIABLES AND CONSTANTS  |
%          |-----|
%
%////////////////////////////////////

mu      = 0.1;      %Viscosity of the fluid (0.1)
u       = 1;       %Velocity of the bearing (1)
M       = 100;     %Number of nodes (Rows)
N       = 100;     %Number of nodes (Columns)
ho      = 2e-5;    %Height at edge of incline (2e-6)
hi      = 1e-5;    %Height at edge of incline (1e-6)
L       = 0.01;    %Length of whole bearing (0.01)
dx      = L/(N-1); %Distance between nodes
dz      = L/(M-1); %Distance between nodes
PRS1    = zeros(M,N); %Initial pressure guess
PRS1(:, :) = 0;
PRS1(:,1) = 0;     %Pressure in combustion chamber just after combustion (~30
                  bar = 30e6 Pa)
PRS1(:,M) = 0;    %Pressure in crankcase (~assuming atmospheric)
PRS1small = 0;
PRS1large = 0;
error    = 10;    %Large initial error to enter loop
crit     = 0.01;  %Convergence criteria of percent error (1%)
% sigma  = 1e-6;  %Standard Deviation

%Call the Cylinder Wall
CylinderWall_GP

```

```

%Calculate Root Mean Square Roughness (Standard Deviation) of Surface 1
(Cylinder Wall)
Rq1 = 0;
len = length(Leveledz2);
for j = 1:len
    OldRq1 = Rq1;
    Rq1 = (z2(j)-avgz(j))^2 + OldRq1;

    if j == len
        Rq1 = (Rq1/len)^(1/2);
    end

    j = j + 1;
end
Rq1 = Rq1 * (1e-4);

%////////////////////////////////////
%
%                |  CALCULATION  |
%                |                |
%////////////////////////////////////

% dx = 2.0408e-6; meters
% dz = 2.0408e-6; meters

for i = 1:M
    for j = 1:N
        z(i) = dz * (i-1);
        %*****Basic Equation for h*****
        hRS1(i,j) = Leveledz2(i,j)*(10^-5) + h; %1.6178 = point in contact
        x(j) = dx * (j-1); %X location at each node
        %Initial Pressure Guess (Line)
        PRS1(i,j) = PRS1small + (PRS1large-PRS1small)/(N-1)*(j-1);
    end
end

figure()
surf(hRS1)
% axis([0 100 0 100 0 5e-5])
xlabel('X-direction')
ylabel('Z-direction')
zlabel('Height/Distance (\mum)')
title('Film Thickness','FontSize',20)
grid on

% FOR DISTANC BEWTEEN TWO SURFACES - UPDATED FILM THICKNESS
% hRS = hRS - (-hRS);

%*****2D PRESSURE PROFILE*****
figure();

```

```

grid on;
plot(x,PRS1);      %Plots every tenth iteration to show convergence
grid on
xlabel('x (m)');
ylabel('P (pa)');
hold off;         %Shows all lines (hold off = show most recent)

%*****CALCULATE UNTIL CONVERGENCE CRITERIA REACHED*****
it = 0;   %Iteration counter
it2=0;
while (error>crit)
    it2=it2+1;   %Uncomment to see number of iterations
    it = it + 1;   %Increment iteration counter
    OldPressure = PRS1; %Updates new pressure
    error = 0;     %Set error to zero to initialize it

    %*****NUMERICAL GRID CALCULATIONS*****
    for i = 1:M     %Calculate Pressure at all nodes with periodic BC's {i
                        direction}

        for j = 1:N %Calculate Pressure at all nodes with periodic BC's {j
                        direction}

            %Periodic Boundary Conditions with Ghost Nodes
            %*****N Direction (j direction)*****
            jj_1 = j+1;
            jj_2 = j-1;

            if jj_1 > N
                jj_1 = jj_1 - N;
            end

            if jj_2 < 1
                jj_2 = jj_2 + N;
            end

            %*****M Direction (i direction)*****
            ii_1 = i+1;
            ii_2 = i-1;

            if ii_1 > M
                ii_1 = ii_1 - M;
            end

            if ii_2 < 1
                ii_2 = ii_2 + M;
            end

            %*****NUMERICAL FILM THICKNESS GRID*****
            %In the i direction

```

```

h3 = (hRS1(ii_1,j)+hRS1(i,j))/2; %Halfway in between node ahead
h4 = (hRS1(i,j)+hRS1(ii_2,j))/2; %Halfway in between node behind

%In the j direction
h1 = (hRS1(i,jj_1)+hRS1(i,j))/2; %Halfway in between node ahead
h2 = (hRS1(i,j)+hRS1(i,jj_2))/2; %Halfway in between node behind

%*****NUMERICAL GRID FOR DELTA*****
%In the j direction
delx(j+1) = dx; %x(j+1)-x(j); %Halfway in between node ahead
delx(j) = dx; %x(j)-x(j-1); %Halfway in between node behind

%In the i direction
delz(i+1) = dz; %z(i+1)-z(i); %Halfway in between node ahead
if i==1
    delz(i) = 0.000101;
else
    delz(i) = dz; %z(i)-z(ii_2); %Halfway in between node behind
end

%*****REYONLDS COEFFICIENTS*****
a0 = (h3-h4)/(delx(j)+delx(jj_1));
a1 = (h4^3)/(delx(j)*(delx(j)+delx(jj_1)));
a2 = (h3^3)/(delx(jj_1)*(delx(j)+delx(jj_1)));
a3 = (h2^3)/(delz(i)*(delz(i)+delz(ii_1)));
a4 = (h1^3)/(delz(ii_1)*(delz(i)+delz(ii_1)));
a5 = a1 + a2 + a3 + a4;

%*****3D PRESSURE EQUATION*****
PRS1(i,j) = dx*(dz^2)*((hRS1(i,jj_1)-hRS1(i,jj_2))/2) -
            ((h4^3)*(PRS1(i,jj_2))*(dz^2)) -
            ((h3^3)*(PRS1(i,jj_1))*(dz^2)) -
            ((h2^3)*(PRS1(ii_2,j))*(dx^2)) -
            ((h1^3)*(PRS1(ii_1,j))*(dx^2));
PRS1(i,j) = PRS1(i,j) / ((dz^2)*(-(h4^3)-(h3^3)) + (dx^2)*(-
            (h2^3)-(h1^3)));

%*****FLOW RATES FOR POISEULLE FLOW*****
q_z_RS(i,j) = (-hRS1(i,j)^3)/(12*mu) * ((PRS1(ii_1,j)-
            PRS1(ii_2,j))/dz);
q_x_RS(i,j) = ((-hRS1(i,j)^3)/(12*mu)) * ((PRS1(i,jj_1)-
            PRS1(i,jj_2))/dx));

%*****FLOW RATES FOR COUETTE FLOW*****
q_x_RS_C = (u/2) * (hRS1/M);

%*****FLOW RATES FOR COUETTE FLOW*****
LargePhiS1(i,j) = ((2/N) * ((hRS1(i,j)^3)/(12*mu)) *
            ((PRS1(i,jj_1)-PRS1(i,jj_2))/dx) ) / (u*Rq1);

```

```

%*****CALCULATE ERROR*****
%Make sure Pressure is not zero and add errors
if(abs(PRS1(i,j))>0)
    error = error + abs((PRS1(i,j)-OldPressure(i,j))/PRS1(i,j));
end

%*****RELAXATION*****
PRS(i,j)=0.9*PRS(i,j)-0.8*OldPressure(i,j);    %Relaxation of 0.8

end    %End j Loop

end        %End i Loop

%Calculate average error in percent
error = error/(N-2)*100/M/N; %Uncomment to see error go down
if(it<10)
    error=10;
end

%*****PLOT THE TENTH ITERATION*****
if (it==10)
    plot(x,PRS1);
    title('Pressure Distribution','FontSize',20)
    grid on
    grid minor
    xlabel('x(m)')
    ylabel('P(pa)')

    hold off
    plot(z,PRS1);
    title('Z-Pressure Distribution','FontSize',20)
    grid on
    grid minor
    xlabel('z(m)')
    ylabel('P(pa)')
    it=0;    %Reset iteration counter
end

end    %End convergence criteria loop

%////////////////////////////////////
%
%                -----
%                |  OUTPUT  |
%                -----
%////////////////////////////////////

%*****PLOT FILM THICKNESS*****

```

```

figure()
plot(x,hRS1)
title('Film Thickness','FontSize',20)
grid on

figure()
surf(hRS1)
title('Film Thickness','FontSize',20)
xlabel('X-direction')
ylabel('Z-direction')
zlabel('Height(\mum)')
grid on

%*****PLOT FLOW RATES*****
figure()
surf(q_x_RS_C)
title('3D Flow Rates - Couette Flow','FontSize',20)
xlabel('X-direction (\mum)')
ylabel('Z-direction (\mum)')
zlabel('Flow Rate (m^3/s)')
set(gca,'XTickLabel',{'0';'200';'400';'600';'800';'1000'})
set(gca,'YTickLabel',{'0';'500';'1000'})
grid on

%*****PLOT 3D PRESSURE CURVES*****
%Plot Surface Mesh
figure()
surf(PRS1)
xlabel('X-direction (\mum)')
ylabel('Z-direction (\mum)')
zlabel('Pressure (Pa)')
set(gca,'XTickLabel',{'0';'200';'400';'600';'800';'1000'})
set(gca,'YTickLabel',{'0';'500';'1000'})
% axis([0 50 0 50 -10e6 10e6])
% colorbar
title('3D Reynolds Plot - Poiseuille Flow','FontSize',20)

%Plot Mesh
figure()
mesh(PRS1)
xlabel('X-direction (\mum)')
ylabel('Z-direction (\mum)')
zlabel('Pressure (Pa)')
set(gca,'XTickLabel',{'0';'200';'400';'600';'800';'1000'})
set(gca,'YTickLabel',{'0';'500';'1000'})
title('3D Reynolds Plot - Couette Flow ','FontSize',20)

% LargePhiS1
LPS1 = sum(sum(LargePhiS1));
end %End function

```

```

%*****
%*****
%***          RING - SMOOTH SURFACE SHEAR FLOW FACTOR          ***
%*                                                    *
%*          MASTERS THESIS 2018                                *
%*                                                    *
%***          ALEX J. LOCKER IV                                ***
%*****
%*****

%*****
% The following function is used to calculate the nodal pressures at one film
% thickness. The film thickness is iterated in the governing program code. This
% is the function that runs the wall against a smooth surface.
%*****

function [LPS2,Rq2] = True_FF_CalculationsRingShear_GP(h)

%film thickness (h) is used in line 110

%////////////////////////////////////
%
%          |  VARIABLES AND CONSTANTS  |
%          |-----|
%////////////////////////////////////

mu      = 0.1;      %Viscosity of the fluid (0.1
u        = 1;       %Velocity of the bearing (1)
M        = 100;    %Number of nodes (Rows)
N        = 100;    %Number of nodes (Columns)
ho       = 2e-5;   %Height at edge of incline (2e-6)
hi       = 1e-5;   %Height at edge of incline (1e-6)
L        = 0.01;   %Length of whole bearing (0.01)
dx       = L/(N-1); %Distance between nodes
dz       = L/(M-1); %Distance between nodes
PRS2     = zeros(M,N); %Initial pressure guess

PRS2(:, :) = 0;
PRS2(:,1) = 0; %Pressure in combustion chamber just after combustion (~30
               bar = 30e6 Pa)
PRS2(:,M) = 0; %Pressure in crankcase (~assuming atmospheric)
PRS2small = 0;
PRS2large = 0;

error    = 10;     %Large initial error to enter loop
crit     = 0.01;   %Convergence criteria of percent error (1%)
sigma    = 1e-6;   %Standard Deviation

```

```

%////////////////////////////////////
%
%          -----
%          |  FORD SURFACE 1  |
%          -----
%////////////////////////////////////

%Call Second Surface (D35 Ring)
FlattenedTopRing_GP
figure()
mesh(LeveledFit)
% axis([0 1000 0 1000 -2 4])
xlabel('X-direction')
ylabel('Z-direction')
zlabel('Height (\mum)')
title('D35 Piston Ring Surface without Curvature','FontSize',20)
grid on

%Calculate Root Mean Square Roughness (Standard Deviation) of Surface 2 (D35
Ring)
Rq2 = 0;
len2 = length(fitwall);
for j = 1:len2
    OldRq2 = Rq2;
    Rq2 = (fitwall(j)-AverageData)^2 + OldRq2;

    if j == len2
        Rq2 = (Rq2/len2)^(1/2);
    end

    j = j + 1;
end
Rq2 = Rq2 * (1e-4);

%////////////////////////////////////
%
%          -----
%          |  CALCULATION  |
%          -----
%////////////////////////////////////

% dx = 2.0408e-6; meters
% dz = 2.0408e-6; meters

for i = 1:M

    for j = 1:N

        z(i) = dz * (i-1);
    end
end

```

```

%*****Basic Equation for h*****
hRS2(i,j) = (-LeveledFit(i,j))*(10^-5) + h; %1.6178 = point in contact

x(j) = dx * (j-1);          %X location at each node

%Initial Pressure Guess (Line)
PRS2(i,j) = PRS2small + (PRS2large-PRS2small)/(N-1)*(j-1);

end
end

figure()
surf(hRS2)
% axis([0 100 0 100 0 5e-5])
xlabel('X-direction')
ylabel('Z-direction')
zlabel('Height/Distance (\mum)')
title('Film Thickness','FontSize',20)
grid on

% FOR DISTANC BEWTEEN TWO SURFACES - UPDATED FILM THICKNESS
% hRS = hRS - (-hRS);

%*****2D PRESSURE PROFILE*****
figure();
grid on;
plot(x,PRS2);      %Plots every tenth iteration to show convergence
grid on
xlabel('x (m)');
ylabel('P (pa)');
hold off;         %Shows all lines (hold off = show most recent)

%*****CALCULATE UNTIL CONVERGENCE CRITERA REACHED*****
it = 0; %Iteration counter
it2=0;
while (error>crit)
    it2=it2+1;      %Uncomment to see iterations calculated
    it = it + 1;    %Increment iteration counter
    OldPressure = PRS2; %Updates new pressure
    error = 0;      %Set error to zero to initialize it

%*****NUMERICAL GRID CALCULATIONS*****
for i = 1:M        %Calculate Pressure at all nodes with periodic BC's {i
                    direction}

    for j = 1:N %Calculate Pressure at all nodes with periodic BC's {j
                    direction}

```

```

%Periodic Boundary Conditions with Ghost Nodes
%*****N Direction (j direction)*****
    jj_1 = j+1;
    jj_2 = j-1;

    if jj_1 > N
        jj_1 = jj_1 - N;
    end

    if jj_2 < 1
        jj_2 = jj_2 + N;
    end

%*****M Direction (i direction)*****
    ii_1 = i+1;
    ii_2 = i-1;

    if ii_1 > M
        ii_1 = ii_1 - M;
    end

    if ii_2 < 1
        ii_2 = ii_2 + M;
    end

%*****NUMERICAL FILM THICKNESS GRID*****
%In the i direction
h3 = (hRS2(ii_1,j)+hRS2(i,j))/2; %Halfway in between node ahead
h4 = (hRS2(i,j)+hRS2(ii_2,j))/2; %Halfway in between node behind

%In the j direction
h1 = (hRS2(i,jj_1)+hRS2(i,j))/2; %Halfway in between node ahead
h2 = (hRS2(i,j)+hRS2(i,jj_2))/2; %Halfway in between node behind

%*****NUMERICAL GRID FOR DELTA*****
%In the j direction
delx(j+1) = dx; %x(j+1)-x(j); %Halfway in between node ahead
delx(j) = dx; %x(j)-x(j-1); %Halfway in between node behind

%In the i direction
delz(i+1) = dz; %z(i+1)-z(i); %Halfway in between node ahead
if i==1
    delz(i) = 0.000101;
else
    delz(i) = dz; %z(i)-z(ii_2); %Halfway in between node behind
end

%*****REYNOLDS COEFFICIENTS*****
a0 = (h3-h4)/(delx(j)+delx(jj_1));
a1 = (h4^3)/(delx(j)*(delx(j)+delx(jj_1)));

```

```

a2 = (h3^3)/(delx(jj_1)*(delx(j)+delx(jj_1)));
a3 = (h2^3)/(delz(i)*(delz(i)+delz(ii_1)));
a4 = (h1^3)/(delz(ii_1)*(delz(i)+delz(ii_1)));
a5 = a1 + a2 + a3 + a4;

%*****3D PRESSURE EQUATION*****
PRS2(i,j) = dx*(dz^2)*((hRS2(i,jj_1)-hRS2(i,jj_2))/2) -
            ((h4^3)*(PRS2(i,jj_2))*(dz^2)) -
            ((h3^3)*(PRS2(i,jj_1))*(dz^2)) -
            ((h2^3)*(PRS2(ii_2,j))*(dx^2)) -
            ((h1^3)*(PRS2(ii_1,j))*(dx^2));
PRS2(i,j) = PRS2(i,j) / ((dz^2)*(-(h4^3)-(h3^3)) + (dx^2)*(-
            (h2^3)-(h1^3)));

%*****FLOW RATES FOR POISEULLE FLOW*****
q_z_RS(i,j) = (-(hRS2(i,j)^3)/(12*mu)) * ((PRS2(ii_1,j)-
            PRS2(ii_2,j))/dz);
q_x_RS(i,j) = (-(hRS2(i,j)^3)/(12*mu)) * ((PRS2(i,jj_1)-
            PRS2(i,jj_2))/dx);

%*****FLOW RATES FOR COUETTE FLOW*****
q_x_RS_C = (u/2) * (hRS2/M);

%*****CALCULATE ERROR*****
%Make sure Pressure is not zero and add errors
if(abs(PRS2(i,j))>0)
    error = error + abs((PRS2(i,j)-OldPressure(i,j))/PRS2(i,j));
end

%*****RELAXATION*****
PRS(i,j)=0.9*PRS(i,j)-0.8*OldPressure(i,j); %Relaxation of 0.8

end %End j Loop

end %End i Loop

%Calculate average error in percent
error = error/(N-2)*100/M/N; %Uncomment to see error go down
if(it<10)
    error=10;
end

%*****PLOT THE TENTH ITERATION*****
if (it==10)
    plot(x,PRS2);
    title('Pressure Distribution','FontSize',20)
    grid on
    grid minor
    xlabel('x(m)')
    ylabel('P(pa)')

```

```

        hold off
        plot(z,PRS2);
        title('Z-Pressure Distribution','FontSize',20)
        grid on
        grid minor
        xlabel('z(m)')
        ylabel('P(pa)')
        it=0;      %Reset iteration counter
    end

end      %End convergence criteria loop

%%%%%%%%%%%%%%%%%%%%%%%%%%%%%%%%%%%%%%%%%%%%%%%%%%%%%%%%%%%%%%%%%%%%%%%%%%%%%%
%
%              -----
%              |  OUTPUT  |
%              -----
%%%%%%%%%%%%%%%%%%%%%%%%%%%%%%%%%%%%%%%%%%%%%%%%%%%%%%%%%%%%%%%%%%%%%%%%%%%%%%

%*****PLOT FILM THICKNESS*****
figure()
plot(x,hRS2)
title('Film Thickness','FontSize',20)
grid on

figure()
surf(hRS2)
title('Film Thickness','FontSize',20)
xlabel('X-direction')
ylabel('Z-direction')
zlabel('Height(\mum)')
grid on

%*****PLOT FLOW RATES*****
figure()
surf(q_x_RS_C)
title('3D Flow Rates - Couette Flow','FontSize',20)
xlabel('X-direction (\mum)')
ylabel('Z-direction (\mum)')
zlabel('Flow Rate (m^3/s)')
set(gca,'XTickLabel',{'0';'200';'400';'600';'800';'1000'})
set(gca,'YTickLabel',{'0';'500';'1000'})
grid on

%*****PLOT 3D PRESSURE CURVES*****
%Plot Surface Mesh
figure()
surf(PRS2)
xlabel('X-direction (\mum)')

```

```

ylabel('Z-direction (\mum)')
xlabel('Pressure (Pa)')
set(gca,'XTickLabel',{'0';'200';'400';'600';'800';'1000'})
set(gca,'YTickLabel',{'0';'500';'1000'})
axis([0 50 0 50 -10e6 10e6])
colorbar
title('3D Reynolds Plot - Poiseuille Flow','FontSize',20)

%Plot Mesh
figure()
mesh(PRS2)
xlabel('X-direction (\mum)')
ylabel('Z-direction (\mum)')
xlabel('Pressure (Pa)')
set(gca,'XTickLabel',{'0';'200';'400';'600';'800';'1000'})
set(gca,'YTickLabel',{'0';'500';'1000'})
title('3D Reynolds Plot - Couette Flow ','FontSize',20)
LPS2 = sum(sum(LargePhiS2)); end %End function

```

```

%*****
%*****
%***          FIT FLOW FACTOR CURVES          ***
%*
%*          MASTERS THESIS 2018              *
%*
%***          ALEX J. LOCKER IV              ***
%*****
%*****

%*****
% The following function takes in the calculated film ratio along with the
% phix, phiz values as well as the shear flow factor for each surface and fits
% these data points to a non-gaussian curve
%*****

function [ax,bx,cx, az,bz, as,bs,cs] =
Fit_FF_Curves(FilmRatio,phis,LPS1,LPS2,phix,phiz)

% LPS1 represents the Phis_s for the Wall
% LPS2 represents the Phis_s for the Ring

%////////////////////////////////////
%
%          |   SHEAR FLOW FACTOR   |
%          |-----|
%
%////////////////////////////////////

%Plot of Raw Data
figure()
plot(FilmRatio,phis, FilmRatio,LPS1, FilmRatio,LPS2)
grid on
legend('Convolute Surfaces (\phi_s)', 'Piston Ring (\Phi_1)', 'Cylinder Wall
(\Phi_2)')
xlabel('h/\sigma', 'FontSize', 15)
ylabel('Shear Flow Factor \phi_s', 'FontSize', 15)
title('Shear Flow Factor', 'FontSize', 20)

%Fit exponential function
phiscurvefit = fit((FilmRatio)', (phis)', 'power2');
phiscoeff    = coeffvalues(phiscurvefit);
as   = phiscoeff(1);
bs   = phiscoeff(2);
cs   = phiscoeff(3);
% ds = phiscoeff(4);

%The General Model is of the form
%   General model:
%   f(x) = a*(x^b)*exp(-c*x + d*(x.^2))
%   Coefficients (with 95% confidence bounds):

```

```

%      a =      0.4042  (0.3686, 0.4398)
%      b =      -1.117  (-1.243, -0.9912)
%      c =      -0.1055 (-0.2034, -0.007549)
%      d =      -0.005322 (-0.0128, 0.00216)

figure()
plot(phiscurvefit,'b',FilmRatio,phis,'m*')
axis([1 7 0 0.8])
xlabel('h/\sigma','FontSize',15)
ylabel('Shear Flow Factor \phi_s','FontSize',15)
title('Shear Flow Factor','FontSize',20)
legend('Data','Fitted Curve')

txt1='a*(x^b)*exp(-c*x + d*(x.^2))';
txt1='\phi_s = 0.4042*(h/\sigma)^-^1.^1^1^7e^{[-0.1055*(h/\sigma) +
0.005*(h/\sigma)^2]} ' ;
text(2.0,0.5,txt1,'HorizontalAlignment','left','VerticalAlignment','top','Bac
kgroundColor',[1 1 1],'FontSize',12);

%*****Patir and Cheng Comparison*****
%*****SAME EQUATION THROUGHOUT*****
%Use a,b,c,d for gamma=2.64
a = 1.621; %A1
b = 0.873; %alpha1
c = 1.09; %alpha2
d = 0.075; %alpha3

phis_PandC = a*(FilmRatio.^b).*exp(-c*FilmRatio + d*(FilmRatio.^2));
%Equation From Paper

figure()
plot(FilmRatio,phis,'b')
hold on
plot(FilmRatio,phis_PandC,'r')
axis([1 7 0 0.8])
grid on
xlabel('h/\sigma','FontSize',15)
ylabel('Shear Flow Factor \phi_s','FontSize',15)
title('Shear Flow Factor','FontSize',20)
legend('FORD D35 measured Rough Surfaces','Patir and Cheng Statistical
Surfaces')

%*****Patir and Cheng Comparison*****
%*****SPLIT UP AT FILM RATIO OF 5*****
%Use a,b,c,d for gamma=2.64
a = 1.621; %A1
b = 0.873; %alpha1
c = 1.09; %alpha2
d = 0.075; %alpha3
e = 0.659; %A2

```





```

phizcurvefit = fit((FilmRatio(1,2:end))',(-phiz+1)', 'exp1');
phizcoeff    = coeffvalues(phizcurvefit); %Determine coefficients a and b
az           = phizcoeff(1);
bz           = phizcoeff(2);

%Correct Logarithmic Equation
FITEQUATION = 1 - az*exp(bz*(FilmRatio(1,2:end)));

figure()
plot(FilmRatio(1,2:end),phiz, 'm*')
hold on
plot(FilmRatio(1,2:end),FITEQUATION, 'b-')
axis([1 7 0 1])
xlabel('h/\sigma', 'FontSize',15)
ylabel('Pressure Flow Factor \phi_z', 'FontSize',15)
title('Z Pressure Flow Factor', 'FontSize',20)
legend('Data', 'Fitted Curve', 'Location', 'southeast')

txt1='1-a*exp^b';
txt1='\phi_z = 1 - 0.6065*e^-^0.^3^3^5^7^*^(^h/^sigma^)';
text(4,0.7,txt1, 'HorizontalAlignment', 'left', 'VerticalAlignment', 'top', 'Backg
roundColor', [1 1 1], 'FontSize',12);

%*****Patir and Cheng Comparison*****
%NOTES: Different method because matlab cannot handle fitting to a decaying
%logarithmic function. A set of linearly spaced points was defined. The set
%of fit methods were used on the equations and then translated to the
%proper region of the graph.

%Linearly spaced points (1 to 7 for h/sigma)
x = linspace(1,7,100);

%Fit from above with coefficients
tNEW = 0.6065*exp(-0.3357*x);

%Using Patir and Cheng coefficients
tfit_PandCNEW = 1.48*exp(-0.42*x);

%Plot the comparision
figure()
plot(x,-tNEW+1, 'b')
hold on
plot(x,-tfit_PandCNEW+1, 'r')
grid on
xlabel('h/\sigma', 'FontSize',15)
ylabel('Pressure Flow Factor \phi_z', 'FontSize',15)
title('Z Pressure Flow Factor', 'FontSize',20)
legend('FORD D35 measured Rough Surfaces', 'Patir and Cheng Statistical
Surfaces', 'Location', 'southeast')
end %End function

```

```

%*****
%*****
%***          2D AXISYMMETRIC REYNOLDS EQUATION WITH FLOW FACTORS          ***
%*
%*
%*          MASTERS THESIS 2018
%*
%*
%***          ALEX J. LOCKER IV
%*****
%*****

%*****
% The following function is the 2D axisymmetric version of the Reynolds
% equation. It utilizes the previously derived flow factors in the governing
% piston ring model to account for surface roughness.
%*****

function [P] =
RE2DwithFF_GP(h,z,dz,u,P_boundary1,P_boundary2,az,bz,as,bs,cs,sigma)

clc;
warning ('off','all');

%////////////////////////////////////
%
%          |  VARIABLES AND CONSTANTS  |
%
%          |-----|
%////////////////////////////////////

mu      = 0.1;          %Viscosity of the fluid (0.1)
M       = length(h);   %Number of nodes (Rows)
P(2:M-1) = 0;         %Initial pressure guess
q_z     = zeros(M);    %Allocate flow rate memory {z direction}
error   = 1;          %Large initial error to enter loop
crit    = 0.1;         %Convergence criteria of percent error (0.1%)
sigma   = 1e-6;       %Standard Deviation
P(1)    = P_boundary1; %Boundary condition crankshaft pressure (atm)
P(M)    = P_boundary2; %Boundary condition combustion chamber pressure (atm)
phi_s   = zeros(M);   %Allocate flow factor memory {shear}

%////////////////////////////////////
%
%          |  CALCULATION  |
%
%          |-----|
%////////////////////////////////////

%*****CALCULATE UNTIL CONVERGENCE CRITERA REACHED*****
it = 0; %Iteration counter

while (error>crit)

```

```

it = it + 1;      %Increment iteration counter
OldPressure = P; %Updates new pressure
error = 0;      %Set error to zero to initialize it

%*****NUMERICAL GRID CALCULATIONS*****
for i = 2:(M-1)  %Calculate Pressure at all nodes except at the edge
                  (Boundary Conditions) {i direction}

    %*****NUMERICAL FILM THICKNESS GRID*****
    %In the i direction
    h1 = (h(i+1)+h(i))/2; %Halfway in between node ahead
    h2 = (h(i)+h(i-1))/2; %Halfway in between node behind

    %*****NUMERICAL SHEAR FLOW FACTOR GRID*****
    %In the i direction
    phi_s_3 = (phi_s(i+1)+phi_s(i))/2; %Halfway in between node ahead
    phi_s_4 = (phi_s(i)+phi_s(i-1))/2; %Halfway in between node behind

    %*****PRESCRIBED FLOW FACTOR EQUATIONS*****
    H_i = h(i)/sigma; %Film thickness for i direction (x)
    phi_z = 1 - az*exp(bz*H_i); %Equation from "A mixed lubrication
                                model considering elastoplastic
                                contact for a piston ring and
                                application to a ring pack"
    phi_s(i) = as*H_i^bs + cs ; %Equation from "A mixed
                                lubrication model considering
                                elastoplastic contact for a piston
                                ring and application to a ring
                                pack"

    %*****REYNOLDS COEFFICIENTS*****
    a0 = 6*mu*u * ((h1-h2)/(z(i)+z(i+1)));
    % a1 = phi_x * ((h4^3)/(x(j)*(x(j)+x(j+1)))); %Unused for
    % axisymmetric case
    a2 = phi_x * ((h3^3)/(x(j+1)*(x(j)+x(j+1)))); %Unused for
    axisymmetric case
    a3 = phi_z * ((h2^3)/(z(i)*(z(i)+z(i+1))));
    a4 = phi_z * ((h1^3)/(z(i+1)*(z(i)+z(i+1))));
    a5 = a3 + a4;
    a6 = sigma * ((phi_s_3-phi_s_4)/(z(i)+z(i+1)));

    %*****3D PRESSURE EQUATION*****
    P(i) = a3*P(i-1) + a4*P(i+1) - a0 - a6;
    P(i) = P(i)/(a5);

    %*****FLOW RATES*****
    q_z = -(h.^3)/(12*mu) * ((P(i+1)-P(i-1))/dz);
    % q_x = ((-h^3)/(12*mu)) * ((P(i,j+1)-P(i,j-1))/dx) + u*h; Not
    % used for axisymmetric case
    New_q_x = q_x(:,1); % Not used for axisymmetric case

```

```

%*****CALCULATE ERROR*****
%Make sure Pressure is not zero and add errors
if(abs(P(i))>0)
    error = error + abs((P(i)-OldPressure(i))/P(i));
end

end        %End i Loop

%Calculate average error in percent
error = error/(M-2)*100

%*****PLOT THE 2D PRESSURE PROFILE TENTH ITERATION*****
if (u ~= 0)
    if (it==10)
        plot(z,P);
        title('Pressure Distribution','FontSize',20)
        grid on
        grid minor
        xlabel('x(m)')
        ylabel('P(pa)')

        it=0;        %Reset iteration counter
    end
end

end        %End convergence criteria loop

%////////////////////////////////////
%
%                |   OUTPUT   |
%                |-----|
%////////////////////////////////////

%*****PLOT FILM THICKNESS*****

if (u == 0)

    sizez = size(z);        %-----|
    if sizez(1) > sizez(2) %   |
        z = z';            %   |-----> Checks the dimension of z
                               |   (Flips if along inner surface)
    end                    %-----|

    figure()
    plot( z(1,(length(z)-length(h)+1):length(z)) , h )
    title('Film Thickness','FontSize',20)
    xlabel('Distance (m)')

```

```

        ylabel('Distance (m)')
        grid on
    else
        figure()
        plot(z,h)
        title('Film Thickness','FontSize',20)
        xlabel('Distance (m)')
        ylabel('Distance (m)')
        grid on
    end
end

% %*****PLOT 3D PRESSURE CURVES*****
%Plot Surface Mesh
figure()
surf(P)
title('3D Reynolds Plot')

%Plot Mesh
figure()
mesh(P)
title('3D Reynolds Plot')

%*****PLOT 2D PRESSURE CURVES*****
if (u == 0)
    figure()
    plot( z(1,(length(z)-length(h)+1):length(z)) ,P)
    title('Pressure','FontSize',20)
    xlabel('Distance (m)')
    ylabel('Pressure (Pa)')
    grid on
else
    figure()
    plot(z,P)
    title('Pressure','FontSize',20)
    xlabel('Distance (m)')
    ylabel('Pressure (Pa)')
    grid on
end

end %End function

```

```

%*****
%*****
%***          ACF AND CCF SURFACE TOPOGRAPHY CHARACTERIZATION          ***
%*
%*                      MASTERS THESIS 2018                      *
%*
%***                      ALEX J. LOCKER IV                      ***
%*****
%*****

```

```

%*****
% The following script calculates the Peklenik number, commonly referred to as
% the surface anisotropy number. This is also referred to as Gamma. By
% calculating the X and Z direction Auto-Correlation Function values the ratio
% is taken to get the ratio. Also the Cross Correlation Function is calculated
% for a more accurate surface characterization parameter.
%*****

```

```

sigma = 0.93884e-6; %Calculated from True_FF_Calculations_ShearV2_GP

```

```

%Read in the data into 5 columns
[A B C D E] = textread('Surfacel_NoWords.txt','%f %c %f %c
%c','headerlines',20); %Need file to end with numbers

```

```

%FOR THE Y VALUES USE THIS CODE
w = 1000; %Number of Samples per row
n = 999; %Number of Repeating Samples
v = repmat(0:n,[w 1]);
v = v(:);

```

```

x1 = A;
y1 = v;
z1 = C;

```

```

%*****LEVEL THE DATA*****

```

```

for j = 1:1000
    sumz = 0;

    if j==1

        for i = 1:1000 %Sum points from 1 to 1000
            sumz = sumz + z1(i);
        end
        a = polyfit(i,j,1);
        avgz(j) = sumz/1000;
        k=0;
        for i = 1 : 1000 %Sum points from X001 to (X+1)000
            k=k+1;
            z2(j,k)=z1(i)-avgz(j)-a(1);
        end
    end
end

```

```

elseif j<=999
    sumz=0;
    for i = (1000*j+1) : (1000*j+1000) %Sum points from X001 to
                                        (X+1)000
        sumz = sumz + z1(i);
    end
    w = polyfit(i,j,1);
    avgz(j) = sumz/1000;
    k=0;
    for i = (1000*j+1) : (1000*j+1000) %Sum points from X001 to
                                        (X+1)000
        k=k+1;
        z2(j,k)=z1(i)-avgz(j)-w(1);
    end

else %For the last point
    for i = 999001:1000000
        sumz = sumz + z1(i);
    end
    e = polyfit(i,j,1);
    avgz(j) = sumz/1000 - e(1);
    k=0;
    for i = 999001:1000000 %Sum points from X001 to (X+1)000
        k=k+1;
        z2(j,k)=z1(i)-avgz(j)-e(1);
    end

end %End j decision loop
end %End j loop

```

```

%Subtract out any average Discrepancies (size of z2 is 1000x1000)
Average = (sum(sum(z2))) / 1e6;
Leveledz2 = z2 - Average;

```

```

figure()
mesh(Leveledz2);
xlabel('X-direction')
ylabel('Z-direction')
zlabel('Height (\mum)')
colorbar
title('D35 Cylinder Wall Surface','FontSize',20)

```

```

%Call Second Surface (D35 Ring)
FlattenedTopRing
figure()
mesh(LeveledFit)
% axis([0 1000 0 1000 -2 4])
xlabel('X-direction')

```

```

ylabel('Z-direction')
zlabel('Height (\mum)')
title('D35 Piston Ring Surface without Curvature','FontSize',20)
grid on

%*****Add both Surfaces*****
figure()
FullSurface = Leveledz2 + LeveledFit; %FOR INDIVIDUAL GAMMAS OR CONVOLUTE
GAMMAS USE THIS LINE TO COMMENT OUT
mesh(FullSurface);
xlabel('X-direction')
ylabel('Z-direction')
zlabel('Height (\mum)')
title('Cylinder Wall and Piston Ring Combined Surface Height','FontSize',20)
grid on

%Columns are Z-Direction
%Rows are X-Direction

%////////////////////////////////////
%
%          |-----|
%          | AUTO CORRELATION FUNCTION |
%          |-----|
%////////////////////////////////////

%*****2D AUTO CORRELATION X DIRETION*****
x = FullSurface(1,:);
N = 1000;
Ls = 1000e-6;
rhox(1:N) = 0;

for bx = 1:N

    betax(bx) = bx/(N-1) * Ls;

    for i = 1:N-bx
        rhox(bx) = rhox(bx) + (x(i)*x(i+bx))/N;
    end

end

%Plot the ACF
figure()
plot(betax,rhox,'b');
xlabel('\beta (m)')
ylabel('ACF (m^2)')
grid on
title('Auto-Correlation Function X-Direction','FontSize',20)

```

```

%Calcualte Half correlation length
HalfACFx = max(rhox)/2;
HalfLambdax = interp1(rhox,betax,HalfACFx);
hold on
plot(HalfLambdax,HalfACFx,'b*')
legend('ACF','Half ACF Length')

%*****2D AUTO CORRELATION Z DIRETION*****
z = FullSurface(:,1);

rhoz(1:N)=0;

it=0;
for bz = 1:N

    betaz(bz) = bz/(N-1) * Ls;

    for i = 1:N-bz
        rhoz(bz) = rhoz(bz) + (z(i)*z(i+bz))/N;
        it=it+1;
    end

end

%Plot the ACF Z-Direction
figure()
plot(betaz,rhoz,'r');
xlabel('\beta (m)')
ylabel('ACF (m^2)')
grid on
title('Auto-Correlation Function Z-Direction','FontSize',20)

%Calcualte Half correlation length
HalfACFz = max(rhoz)/2;
HalfLambdaz = interp1(rhoz,betaz,HalfACFz);
hold on
plot(HalfLambdaz,HalfACFz,'r*')
legend('ACF','Half ACF Length')

%*****
%Plot Both Functions together
figure()
plot(betax,rhox,'b');
hold on
plot(HalfLambdax,HalfACFx,'b*')
hold on
plot(betaz,rhoz,'r');
hold on
plot(HalfLambdaz,HalfACFz,'r*')
xlabel('\beta (m)')

```

```

ylabel('ACF (m^2)')
grid on
% title('Auto-Correlation Functions','FontSize',20)
legend('X-Direction','1/2 X-Correlation Length','Z-Direction','1/2 Z-
Correlation Length')% <----- Two possible legend entries
% legend('X-Direction','\lambda_0_.5_X','Z-Direction','\lambda_0_.5_z')
<-----|

%*****
GAMMA = HalfLambdaz/HalfLambdax % Surface Characterization number
(Peklenik number)
%*****

%////////////////////////////////////
%
%          | CROSS CORRELATION FUNCTION |
%          |
%          |
%          |
%////////////////////////////////////

%Use FullSurface for heights
%TAKES 11.5 HOURS TO RUN BELOW HERE!!!! CAUTION!!!!

rho(N:N)=0;

for e = 1:N

    for d = 1:N

        for b = 1:N

            beta(b) = b/(N-1) * Ls;

            for i = 1:N-b
                rho(b) = rho(b) + (FullSurface(i,d)*FullSurface(i+b,e))/N;
                it=it+1;
            end

        end

    end

end

%Plot the Cross Correlation Function
figure()
plot(beta,rho,'b');

```

```

xlabel('\beta (m)')
ylabel('CCF (m^2)')
grid on
title('Cross-Correlation Function','FontSize',20)

%Calcualte Half correlation length and plot
HalfCCF = max(rho)/(2);
HalfLambda = interp1(rho,beta,HalfCCF)
hold on
plot(HalfLambda,HalfCCF,'b*')
legend('CCF','Half CCF Length')

%NORMALIZE RHO FOR MAXIMUM OF 1
normalizedrho = rho/max(rho);
halfccftest = max(normalizedrho)/2;
halflambdaatest = interp1(normalizedrho,beta,halfccftest)

%Plot normalized rho
figure()
plot(beta,normalizedrho,'b')
xlabel('\beta (m)')
ylabel('CCF (m^2)')
grid on
% title('Cross-Correlation Function Normalized','FontSize',20)
hold on
plot(halflambdaatest,halfccftest,'b*')
legend('Cross-Correlation Length','1/2 Correlation Length')
% axis([0 9e-5 -0.4 1])

```

```

%*****
% The following function was written by Nolan Chu to calculate the contact
% pressure upon given the film thickness, h.
%*****

function PAn=eplasticG_Wcf(h)
tic
import=xlsread('derivscombined_GP.xlsx');
Rv=import(1,:);sigmav=import(3,:);etav=import(2,:);%converting to meters
E=.965*10^11;%Pa
nu=.26;
Eprime=.5/((1-nu^2)/E);%in contact with a rigid surface
Sy=22*10^7;%Pa
for ru=1:length(etav)
%Jackson and Green's prediction of initial loading, von Mises yield
C=1.295*exp(.736*nu);
omegac=Rv(ru)*(pi*C*Sy/(2*Eprime))^2;
Acrit=pi^3*(C*Sy*Rv(ru)/(2*Eprime))^2;
Pcrit=4/3*(Rv(ru)/Eprime)^2*(C/2*pi*Sy)^3;B=.14*exp(23*Sy/Eprime);
for jj=1:length(h)
    limit=linspace(h(jj),300*sigmav(ru),101);
    %    limit=h(jj):sigmav(ru)*.005:sigmav(ru)*10;
    omega=limit-h(jj);a=sqrt(omega*Rv(ru));nodes(jj)=length(limit);
    yv=normpdf(limit,0,sigmav(ru));

omegastar=omega/omegac;a=sqrt(1/pi()*Acrit*omegastar.*(omegastar/(1.9)).^B);
H=Sy*(2.84-.92*(1-cos(pi*a/Rv(ru))));
Force=4/3*Eprime*sqrt(Rv(ru))*omega.^1.5;
Areacontact=pi*Rv(ru)*omega;
for kk=1:length(omega)
if omeagastar(kk)>1.9*omegac;
    Force=Pcrit*(exp(-
.25*omegastar.^(5/12)).*omegastar.^1.5+4*H/(C*Sy).*(1-exp(-
.04*omegastar.^(5/9))).*omegastar);
    B=.14*exp(23*Sy/Eprime);
    Areacontact=Acrit*omegastar.*(omegastar/(1.9)).^B;
end
end
integrand=Areacontact.*yv;
if nodes(jj)==1
    Arat(jj,ru)=0;PAn(jj,ru)=0;
else
Arat(jj,ru)=etav(ru)*Simpsons_1_3_GP(limit,integrand);
integrand2=Force.*yv;
PAn(jj,ru)=etav(ru)*Simpsons_1_3_GP(limit,integrand2);
end
end
end
end

```

```

%*****
% The following function was written by Nolan Chu that utilizes Simpson's
% rule to determine the real area of contact and the normalized pressure.
%*****

function [ out ] = Simpsons_1_3( xv,yv )
%Simpsons_1_3 approximates an integral using parabolas

[a,b]=size(xv);[c,d]=size(yv);sum=0;g=length(xv)/2;
if a~=1 & b~=1 | c~=1 & d~=1
    error('Inputs must not be matrices')
elseif length(xv)~=length(yv)
    error('Input vectors must be of the same length')
elseif g~=floor(g)
    error('Simpson''s rule requires an even number of subintervals')
end
delta=xv(2)-xv(1);
for f=2:length(xv)-1
    if abs(delta-(xv(f+1)-xv(f)))>10^-7
        error('independent vector intervals not equally spaced')
    end
end
for n=2:2:length(xv)-1
    simpson=(xv(n+1)-xv(n-1))/6*(yv(n-1)+4*yv(n)+yv(n+1));
    sum=sum+simpson;
end
out=sum;

```

## **APPENDIX B**

### **FUTURE MODELS**

The following Appendix represent the models that have made progress, however have not yet been implemented into the overall piston ring model program, outlined in Chapter 5.

B.1 Heat Balance .....	209
B.1.1 Heat Transfer Equation Derivation .....	209
B.2 Temperature/Viscosity Model.....	215

## B.1 Heat Balance

In order to solve the steady-state heat conduction problem, the finite difference method was employed similar to the Reynolds equation. At the macroscopic level, the piston ring model utilizes cylindrical coordinates. At the microscopic level, a Cartesian coordinate system is able to be employed in the derivation of the flow factors.

At the smaller scale level there is seen to be no curvature in the piston ring, and thusly the model was solved in Cartesian coordinates. In analyzing the ring dynamics involved, the cylindrical coordinate system is used to account for this curvature. The two-dimensional, steady state, axisymmetric conduction equation was derived from the energy equation.

### B.1.1 Heat Transfer Equation Derivation

The heat transfer equation for this particular system is derived from the energy equation, expressed in tensor notation as

$$\rho \frac{\partial e}{\partial t} + \rho u_k \frac{\partial e}{\partial x_k} = -p \frac{\partial u_k}{\partial x_k} + \frac{\partial}{\partial x_j} \left( k \frac{\partial T}{\partial x_j} \right) + \lambda \left( \frac{\partial u_k}{\partial x_k} \right)^2 + \mu \left( \frac{\partial u_i}{\partial x_j} + \frac{\partial u_j}{\partial x_i} \right) \frac{\partial u_j}{\partial x_i} \quad (94)$$

where the dissipation function is equal to the last two term of Eq. (94)

$$\Phi = \lambda \left( \frac{\partial u_k}{\partial x_k} \right)^2 + \mu \left( \frac{\partial u_i}{\partial x_j} + \frac{\partial u_j}{\partial x_i} \right) \frac{\partial u_j}{\partial x_i} \quad (95)$$

Employing continuity gives

$$\frac{\partial u_k}{\partial x_k} = 0 \quad (96)$$

With simplification the dissipation function (Eq. (95)) becomes

$$\Phi = \frac{1}{2}\mu \left( \frac{\partial u_i}{\partial x_j} + \frac{\partial u_j}{\partial x_i} \right)^2 \quad (97)$$

The material derivative is related to the left hand side of Eq. (94) through

$$\frac{De}{Dt} = \frac{\partial e}{\partial t} + u_k \frac{\partial e}{\partial x_k} \quad (98)$$

where  $e$  represents the internal energy per unit mass. Multiplying Eq. (98) through by density,  $\rho$ , gives

$$\rho \frac{De}{Dt} = \rho \frac{\partial e}{\partial t} + \rho u_k \frac{\partial e}{\partial x_k} \quad (99)$$

The first term on the right hand side of Eq. (99) represents the temporal change, and the second term on the right hand side represents the local convective changes as the fluid flows from one point to another. Assuming these changes are negligible than the material derivative of internal energy per unit mass (Eq. (99)) becomes

$$\rho \frac{De}{Dt} = 0 \quad (100)$$

So the energy equation becomes

$$0 = \frac{\partial}{\partial x_j} \left( k \frac{\partial T}{\partial x_j} \right) + \frac{1}{2}\mu \left( \frac{\partial u_i}{\partial x_j} + \frac{\partial u_j}{\partial x_i} \right)^2 \quad \text{For } i, j = 1, 2 \quad (101)$$

Expanding this tensor notation gives the two dimensional steady state energy equation

$$0 = 2k \left( \frac{\partial^2 T}{\partial x^2} + \frac{\partial^2 T}{\partial y^2} \right) + \mu \left[ 2 \left( \frac{\partial u}{\partial x} \right)^2 + 2 \left( \frac{\partial v}{\partial y} \right)^2 + \left( \frac{\partial u}{\partial x} + \frac{\partial v}{\partial y} \right)^2 \right] \quad (102)$$

Employing a cylindrical coordinate system gives the governing heat transfer equation

$$\frac{\partial^2 T}{\partial r^2} + \frac{1}{r} \frac{\partial T}{\partial r} + \frac{\partial^2 T}{\partial z^2} + \frac{\dot{q}}{2k} = 0 \quad (103)$$

where the heat generation is a function of the viscous and frictional heating

$$\dot{q} = q_{viscous} + q_{friction} \quad (104)$$

And the conduction term is represented by the first three terms of Eq. (103)

$$\frac{\partial^2 T}{\partial r^2} + \frac{1}{r} \frac{\partial T}{\partial r} + \frac{\partial^2 T}{\partial z^2} = 0 \quad (105)$$

The conduction equation (Eq. (105)) is able to be solved for by using a similar nodal network for the Reynolds equation discretization (shown in Figure 3.20). The nodal discretization for temperature is shown in Figure B.1.

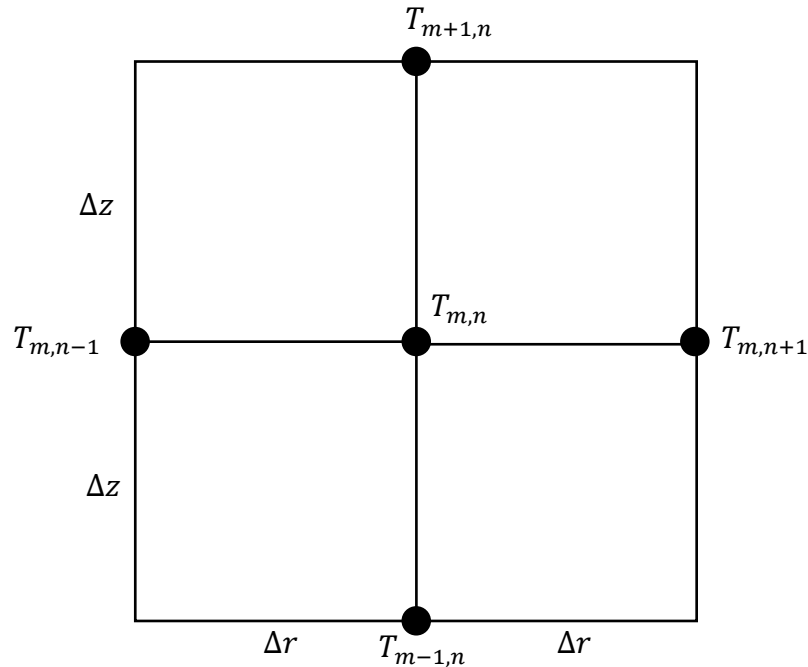


Figure B.1: Discretization of Temperature ( $T$ )

Employing the center difference for the first term on the left hand side of the conduction equation (Eq. (105))

$$\frac{\partial^2 T}{\partial r^2} = \frac{\left(\frac{\partial T}{\partial r}\right)_{m,n+1/2} - \left(\frac{\partial T}{\partial r}\right)_{m,n-1/2}}{r_{m,n+1/2} - r_{m,n-1/2}} = \frac{\frac{T_{m,n+1} - T_{m,n}}{\Delta r} - \frac{T_{m,n} - T_{m,n-1}}{\Delta r}}{\Delta r} \quad (106)$$

which simplifies too

$$\frac{\partial^2 T}{\partial r^2} = \frac{T_{m,n+1} - 2T_{m,n} + T_{m,n-1}}{(\Delta r)^2} \quad (107)$$

Applying the same methodology in the  $z$  direction for the third term on the left hand side of Eq. (105) gives

$$\frac{\partial^2 T}{\partial z^2} = \frac{T_{m+1,n} - 2T_{m,n} + T_{m-1,n}}{(\Delta z)^2} \quad (108)$$

The second term on the left hand side of the conduction equation (Eq. (105)) is discretized as

$$\frac{1}{r} \frac{\partial T}{\partial r} = \frac{1}{r} \frac{T_{m,n+1} - T_{m,n-1}}{r_{m,n+1} - r_{m,n-1}} = \frac{T_{m,n+1} - T_{m,n-1}}{2(\Delta r)^2} \quad (109)$$

By combining Eqs. (107-109) and solving for  $T_{m,n}$  the total nodal temperature results in the expression

$$T_{m,n} = \frac{(\Delta z)^2 (3T_{m,n+1} + T_{m,n-1}) + 2(\Delta r)^2 (T_{m+1,n} + T_{m-1,n})}{-4[(\Delta z)^2 + (\Delta r)^2]} \quad (110)$$

Before incorporating this nodal temperature into the piston ring model, this heat transfer model was to be first run through a verification simulation. The simulation was run on a hypothetical plate acting as the piston ring. To test the convergence, three arbitrary points are chosen at various distances from each surface edge, with two temperatures applied at the upper

and lower piston ring face. It is assumed the combustion stroke has just initiated and the temperature in the combustion chamber is 2500K, thus the upper piston ring surface is modeled as being 2500K. The lower piston ring surface is modeled at the crankcase temperature of 273K. The steady-state solution is shown in Figure B.2. The convergence temperature at each point location is shown in Figure B.3. Similar to the method discussed in Section 3.3.4 the convergence criteria was chosen to be 1%. The final converged temperature values for each point is shown in Figure B.4.

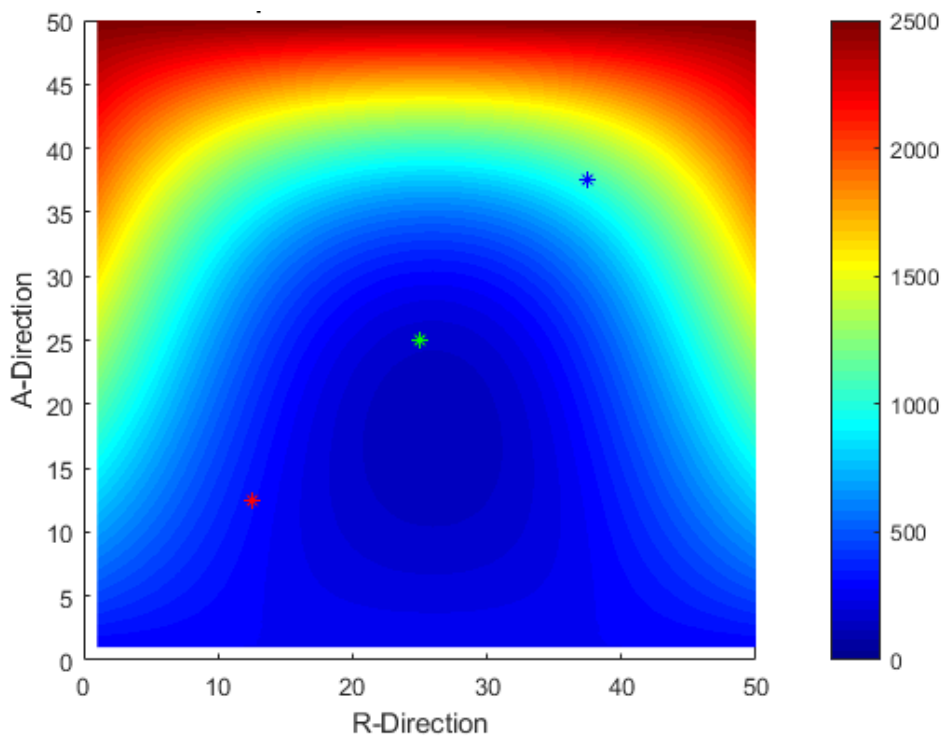


Figure B.2: Converged temperatures across four surfaces

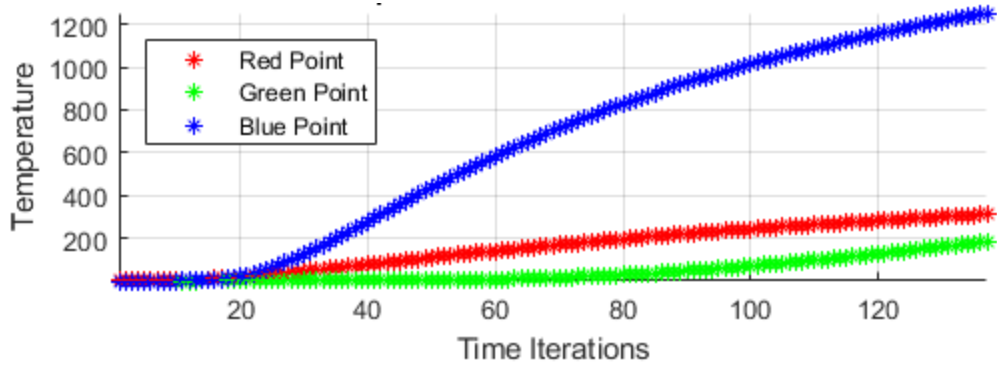


Figure B.3: Temperatures at each point converging

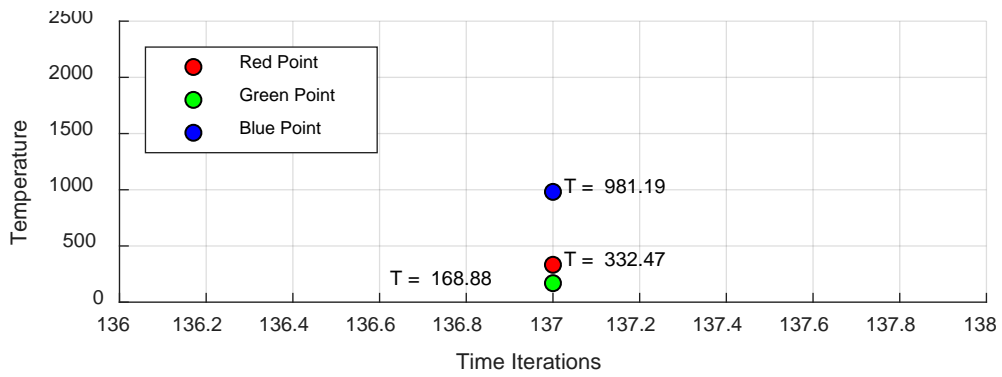


Figure B.4: Converged temperature value and time

The two dimensional, axisymmetric, steady state conduction equation has been solved and will be incorporated into the model in the future.

## *B.2 Temperature/Viscosity Model*

As the piston moves linearly throughout the combustion cycle, its frictional work generates heat. This heat causes the temperature of the lubricant to rise. Temperature has a large effect on viscosity; as the temperature rises, the lubricant becomes less viscous, and vice versa, as the temperature of a lubricant decrease, its viscosity increases. The lubricants viscosity is able to be modeled after the Roeland's equation [78], which models the effect of temperature on viscosity independently from pressure as

$$\log(\log\mu + 1.2) = -S_0 \log\left(1 + \frac{T_m}{135}\right) + \log(G_0) \quad (111)$$

Solving for viscosity gives

$$\mu = 10^{G_0(1+T_m/135)^{-S_0}} \quad (112)$$

where  $S_0$  and  $G_0$  are Roeland's constants. This temperature dependent viscosity model will be incorporated into the piston ring model in the future to more accurately describe the changing viscosity throughout the combustion cycle.

## REFERENCES

- [1] N. Patir and H. Cheng, "An average flow model for determining effects of three-dimensional roughness on partial hydrodynamic lubrication," *Journal of Lubrication Technology*, vol. 100, pp. 12-17, 1978.
- [2] J. Peklenik, "Paper 24: New developments in surface characterization and measurements by means of random process analysis," in *Proceedings of the Institution of Mechanical Engineers, Conference Proceedings*, 1967, pp. 108-126.
- [3] S. Tzeng and E. Saibel, "Surface roughness effect on slider bearing lubrication," *Asle Transactions*, vol. 10, pp. 334-348, 1967.
- [4] M. Leighton, Rahmani, R., Rahnejat, H., "Surface-specific flow factors for prediction of friction of cross-hatched surfaces," *Surface Topography: Metrology and Properties*, vol. 4, 2016.
- [5] S. Mezghani, I. Demirci, M. Yousfi, and M. El Mansori, "Running-in wear modeling of honed surface for combustion engine cylinderliners," *Wear*, vol. 302, pp. 1360-1369, 2013.
- [6] R. L. Jackson and I. Green, "On the modeling of elastic contact between rough surfaces," *Tribology Transactions*, vol. 54, pp. 300-314, 2011.
- [7] R. L. Jackson, "An analytical solution to an Archard-type fractal rough surface contact model," *Tribology Transactions*, vol. 53, pp. 543-553, 2010.

- [8] R. L. Jackson, "The effect of scale-dependent hardness on elasto-plastic asperity contact between rough surfaces," *Tribology Transactions*, vol. 49, pp. 135-150, 2006.
- [9] R. L. Jackson and I. Green, "A statistical model of elasto-plastic asperity contact between rough surfaces," *Tribology International*, vol. 39, pp. 906-914, 2006.
- [10] L. Kogut and R. L. Jackson, "A comparison of contact modeling utilizing statistical and fractal approaches," *Journal of tribology*, vol. 128, pp. 213-217, 2006.
- [11] R. L. Jackson, H. Liu, and D. Leray, "A Comparison of the Predictions of a Finite Element Model and Multiscale Model for a Rough MEMS Electrical Contact," in *Holm Conference on Electrical Contacts (HOLM), 2013 IEEE 59th*, 2013, pp. 1-9.
- [12] R. L. Jackson and I. Green, "The thermoelastic behavior of thrust washer bearings considering mixed lubrication, asperity contact, and thermoviscous effects," *Tribology Transactions*, vol. 51, pp. 19-32, 2008.
- [13] R. L. Jackson and I. Green, "The behavior of thrust washer bearings considering mixed lubrication and asperity contact," *Tribology Transactions*, vol. 49, pp. 233-247, 2006.
- [14] S. V. Angadi, R. L. Jackson, S.-y. Choe, G. T. Flowers, B.-Y. Lee, and L. Zhong, "A multiphysics finite element model of a 35A automotive connector including multiscale rough surface contact," *Journal of Electronic Packaging*, vol. 134, p. 011001, 2012.
- [15] M. Mahajan, R. Jackson, and G. Flowers, "Experimental and analytical investigation of a dynamic gas squeeze film bearing including asperity contact effects," *Tribology Transactions*, vol. 51, pp. 57-67, 2008.

- [16] J. Jang and M. Khonsari, "Thermoelastic instability with consideration of surface roughness and hydrodynamic lubrication," *Journal of tribology*, vol. 122, pp. 725-732, 2000.
- [17] J. Jang and M. Khonsari, "Thermoelastic instability including surface roughness effects," *Journal of tribology*, vol. 121, pp. 648-654, 1999.
- [18] J. Jang and M. Khonsari, "Thermoelastic instability of two-conductor friction system including surface roughness," *Journal of applied mechanics*, vol. 71, pp. 57-68, 2004.
- [19] J. Jang and M. Khonsari, "A generalized thermoelastic instability analysis," in *Proceedings of the Royal Society of London A: Mathematical, Physical and Engineering Sciences*, 2003, pp. 309-329.
- [20] C. L. Davis, C. M. Krousgrill, and F. Sadeghi, "Effect of temperature on thermoelastic instability in thin disks," *Journal of tribology*, vol. 124, pp. 429-437, 2002.
- [21] M. E. Construction, "What is the function of the piston?," in <https://constructionmechanical-engineering.blogspot.com/2010/01/what-is-function-of-piston.html>, ed, 2010.
- [22] R. Stone, "Introduction to internal combustion engines," *Society of Automotive Engineers*, vol. 3, 1999.
- [23] B. Secondmain, "BMW Revised Motor," in <https://secondemain.fr/auto-pieces-accessoires/pièces/bmw/revision-moteur-bmw-325i-318i-221173556.html>, ed, 2017.
- [24] u. Ipd, "Spark plug set," in <https://ipdusa.com/products/4876/113440-spark-plug-set>, ed, 2017.

- [25] J. B. Heywood, "Internal combustion engine fundamentals," 1988.
- [26] L. Ting and J. Mayer, "Piston ring lubrication and cylinder bore wear analysis, part I— theory," *Journal of Lubrication Technology*, vol. 96, pp. 305-313, 1974.
- [27] D. Dowson, "A generalized Reynolds equation for fluid-film lubrication," *International Journal of Mechanical Sciences*, vol. 4, pp. 159-170, 1962.
- [28] W. W. F. Chong, M. Teodorescu, and N. D. Vaughan, "Cavitation induced starvation for piston-ring/liner tribological conjunction," *Tribology International*, vol. 44, pp. 483-497, 2011.
- [29] S. Furuhashi, "A dynamic theory of piston-ring lubrication: 1st report, calculation," *Bulletin of JSME*, vol. 2, pp. 423-428, 1959.
- [30] O. Akalin and G. M. Newaz, "Piston ring-cylinder bore friction modeling in mixed lubrication regime: part I—analytical results," *Journal of Tribology*, vol. 123, pp. 211-218, 2001.
- [31] H. Chen, V. Patel, and S. Ju, "Solutions of Reynolds-averaged Navier-Stokes equations for three-dimensional incompressible flows," *Journal of Computational Physics*, vol. 88, pp. 305-336, 1990.
- [32] C. Singh and P. Sinha, "The three-dimensional Reynolds equation for micro-polar-fluid-lubricated bearings," *Wear*, vol. 76, pp. 199-209, 1982.
- [33] Y. Peiran and W. Shizhu, "A generalized Reynolds equation for non-Newtonian thermal elastohydrodynamic lubrication," *Journal of Tribology*, vol. 112, pp. 631-636, 1990.

- [34] I. Dien and H. Elrod, "A generalized steady-state Reynolds equation for non-Newtonian fluids, with application to journal bearings," *Journal of Lubrication Technology*, vol. 105, pp. 385-390, 1983.
- [35] A. Metzner and J. Reed, "Flow of non-newtonian fluids—correlation of the laminar, transition, and turbulent-flow regions," *AICHE Journal*, vol. 1, pp. 434-440, 1955.
- [36] Y. Mitsuya, T. Ohkubo, and H. Ota, "Averaged Reynolds equation extended to gas lubrication possessing surface roughness in the slip flow regime: approximate method and confirmation experiments," *Journal of Tribology*, vol. 111, pp. 495-503, 1989.
- [37] L. Wu and D. Bogy, "New first and second order slip models for the compressible Reynolds equation," *Journal of Tribology*, vol. 125, pp. 558-561, 2003.
- [38] R. L. Jackson, "The wear and thermo-elastohydrodynamic behavior of thrust washer bearings under non-axisymmetric loads," Doctor of Philosophy in Mechanical Engineering, Woodruff School of Mechanical Engineering, Georgia Institute of Technology, 2004.
- [39] S. a. Technologies, "Tribological properties and applications of alumina," in [https://substech.com/dokuwiki/doku.php?id=tribological\\_properties\\_and\\_applications\\_of\\_alumina](https://substech.com/dokuwiki/doku.php?id=tribological_properties_and_applications_of_alumina), ed, 2016.
- [40] N. Patir and H. Cheng, "Application of average flow model to lubrication between rough sliding surfaces," *Journal of Lubrication Technology*, vol. 101, pp. 220-229, 1979.
- [41] A. K. Singhal, M. M. Athavale, H. Li, and Y. Jiang, "Mathematical basis and validation of the full cavitation model," *Journal of fluids engineering*, vol. 124, pp. 617-624, 2002.

- [42] K.-O. Olsson, "Cavitation in dynamically loaded bearing," *Trans. Chalmers Univ. of Tech, Sweden*, vol. 308, 1957.
- [43] S. F. Hoerner, *Fluid-dynamic drag: practical information on aerodynamic drag and hydrodynamic resistance*: Hoerner Fluid Dynamics, 1965.
- [44] L. Floberg, "On hydrodynamic lubrication with special reference to sub-cavity pressures and number of streamers in cavitation regions(Hydrodynamic bearing lubrication of rotating cylinder with reference to sub-cavity pressure and cavitation regions)," *1965. 37 P*, 1965.
- [45] W. Stieber, "Hydrodynamische Theorie des Gleitlagers das Schwimmlager," *VDI, Berlin*, 1933.
- [46] H. W. Swift, "THE STABILITY OF LUBRICATING FILMS IN JOURNAL BEARINGS.(INCLUDES APPENDIX)," in *Minutes of the Proceedings of the Institution of Civil Engineers*, 1932, pp. 267-288.
- [47] Q. Yang and T. G. Keith Jr, "An elastohydrodynamic cavitation algorithm for piston ring lubrication," *Tribology Transactions*, vol. 38, pp. 97-107, 1995.
- [48] M. Kozubková, J. Rautová, and M. Bojko, "Mathematical model of cavitation and modelling of fluid flow in cone," *Procedia Engineering*, vol. 39, pp. 9-18, 2012.
- [49] B. Jakobsson, "The finite journal bearing considering vaporization," *Trans. Chalmers Univ. of Tech, Sweden*, vol. 190, 1965.
- [50] H. G. Elrod, "A cavitation algorithm," *ASME J. Lubr. Technol.*, vol. 103, p. 350, 1981.

- [51] A. Paydas and E. Smith, "A flow-continuity approach to the analysis of hydrodynamic journal bearings," *Proceedings of the Institution of Mechanical Engineers, Part C: Mechanical Engineering Science*, vol. 206, pp. 57-69, 1992.
- [52] L. Liu, "Modeling the performance of the piston ring-pack with consideration of non-axisymmetric characteristics of the power cylinder system in internal combustion engines," Massachusetts Institute of Technology, 2005.
- [53] M. Ma, I. Sherrington, and E. Smith, "Implementation of an algorithm to model the starved lubrication of a piston ring in distorted bores: prediction of oil flow and onset of gas blow-by," *Proceedings of the Institution of Mechanical Engineers, Part J: Journal of Engineering Tribology*, vol. 210, pp. 29-44, 1996.
- [54] S. R. Harp and R. F. Salant, "An average flow model of rough surface lubrication with inter-asperity cavitation," *Journal of tribology*, vol. 123, pp. 134-143, 2001.
- [55] A. Sommerfeld, "Zur Theorie der Schmiermittelreibung," *Archiv für Elektrotechnik*, vol. 3, pp. 1-5, 1914.
- [56] M. Priest, D. Dowson, and C. Taylor, "Theoretical modelling of cavitation in piston ring lubrication," *Proceedings of the Institution of Mechanical Engineers, Part C: Journal of Mechanical Engineering Science*, vol. 214, pp. 435-447, 2000.
- [57] E. Gumbel, Reibung, and Schmierung, "Vergleich der Ergebnisse der rechnerischen Behandlung des Lagerschmierangproblem mit neueren Versuchsergebnissen," *Monatsbl. Berliner Bez. Ver. Dtsch. Ing.*, pp. 125-128, 1921.

- [58] P. J. Zwart, A. G. Gerber, and T. Belamri, "A two-phase flow model for predicting cavitation dynamics," in *Fifth international conference on multiphase flow, Yokohama, Japan*, 2004.
- [59] G. H. Schnerr and J. Sauer, "Physical and numerical modeling of unsteady cavitation dynamics," in *Fourth international conference on multiphase flow, New Orleans, USA*, 2001.
- [60] B. N. Surfaces, "Performing 3D Optical Profiling Surface Measurements that Correlate to Traceable Standards," *AZO Materials*, 2016.
- [61] N. Patir, "A numerical procedure for random generation of rough surfaces," *Wear*, vol. 47, pp. 263-277, 1978.
- [62] C. Dodds and J. Robson, "The description of road surface roughness," *Journal of sound and vibration*, vol. 31, pp. 175-183, 1973.
- [63] W.-L. Li and W.-T. Chien, "Parameters for roughness pattern and directionality," *Tribology Letters*, vol. 17, pp. 547-551, 2004.
- [64] I. Green, "Numerical Solution of the Reynolds Equation," Georgia Institute of Technology, 2002.
- [65] B. E. R. Khonsari Michael M., *Applied Tribology, Bearing Design and Lubrication* vol. 2: Jon Wiley & Sons Ltd, 2008.
- [66] N. Chu, "The Effect of Asperity Geometry on Elastic-Plastic Statistical and Multi-scale Rough Surface Contact Models," Master of Science, Mechanical Engineering, Auburn University, 2018.

- [67] J. Greenwood and J. P. Williamson, "Contact of nominally flat surfaces," in *Proc. R. Soc. Lond. A*, 1966, pp. 300-319.
- [68] R. L. Jackson and J. L. Streater, "A multi-scale model for contact between rough surfaces," *Wear*, vol. 261, pp. 1337-1347, 2006.
- [69] A. Rostami and R. L. Jackson, "Predictions of the average surface separation and stiffness between contacting elastic and elastic-plastic sinusoidal surfaces," *Proceedings of the Institution of Mechanical Engineers, Part J: Journal of Engineering Tribology*, vol. 227, pp. 1376-1385, 2013.
- [70] R. Goltsberg and I. Etsion, "A universal model for the load-displacement relation in an elastic coated spherical contact," *Wear*, vol. 322, pp. 126-132, 2015.
- [71] R. Goltsberg, I. Etsion, and G. Davidi, "The onset of plastic yielding in a coated sphere compressed by a rigid flat," *Wear*, vol. 271, pp. 2968-2977, 2011.
- [72] W. Song, L. Li, I. Etsion, A. Ovcharenko, and F. E. Talke, "Yield inception of a soft coating on a flat substrate indented by a rigid sphere," *Surface and Coatings Technology*, vol. 240, pp. 444-449, 2014.
- [73] W. Song, L. Li, A. Ovcharenko, D. Jia, I. Etsion, and F. E. Talke, "Plastic yield inception of an indented coated flat and comparison with a flattened coated sphere," *Tribology International*, vol. 53, pp. 61-67, 2012.
- [74] L. V. Almeida, R. Ramadoss, R. L. Jackson, K. Ishikawa, and Q. Yu, "Laterally actuated multicontact MEMS relay fabricated using MetalMUMPS process: experimental

- characterization and multiscale contact modeling," *Journal of Micro/Nanolithography, MEMS, and MOEMS*, vol. 6, p. 023009, 2007.
- [75] J. R. Polchow, S. Angadi, R. L. Jackson, S.-y. Choe, G. T. Flowers, B.-Y. Lee, and L. Zhong, "A Multi-Physics Finite Element Analysis of Round Pin High Power Connectors," in *2010 Proceedings of the 56th IEEE Holm Conference on Electrical Contacts*, 2010.
- [76] R. L. Jackson, S. H. Bhavnani, and T. P. Ferguson, "A multiscale model of thermal contact resistance between rough surfaces," *Journal of Heat Transfer*, vol. 130, p. 081301, 2008.
- [77] R. L. Jackson, H. Ghaednia, Y. A. Elkady, S. H. Bhavnani, and R. W. Knight, "A closed-form multiscale thermal contact resistance model," *IEEE Transactions on Components, Packaging and Manufacturing Technology*, vol. 2, pp. 1158-1171, 2012.
- [78] C. Roelands, J. Vlugter, and H. Waterman, "The viscosity-temperature-pressure relationship of lubricating oils and its correlation with chemical constitution," *Journal of Basic Engineering*, vol. 85, pp. 601-607, 1963.